Fall 2022

Magnetic Field Directed Self-Assembly of Colloidal Nanoparticles via Extreme Field Gradients of Magnetic Recording Media

Abdul Rahman Mohtasebzadeh

Magnetic Field Directed Self-Assembly of Colloidal Nanoparticles via Extreme Field Gradients of Magnetic Recording Media

by

Abdul Rahman Mohtasebzadeh

Bachelor of Science
Herat University 2008

Master of Science
University of South Carolina 2014

Submitted in Partial Fulfillment of the Requirements

for the Degree of Doctor of Philosophy in

Physics

College of Arts and Sciences

University of South Carolina

2022

Accepted by:

Thomas M. Crawford, Major Professor

Richard Creswick, Committee Member

Yanwen Wu, Committee Member

Morgan Stefik, Committee Member

Cheryl L. Addy, Interim Vice Provost and Dean of the Graduate School

Acknowledgments

Words cannot express my gratitude to my advisor Dr. Thomas Crawford for his invaluable patience, motivation, support, and feedback. I also could not have undertaken this journey without my defense committee, Dr. Richard Creswick, Dr. Morgan Stefik, and Dr. Yanwen Wu, who generously provided knowledge and expertise. Additionally, this endeavor would not have been possible without the generous support from the Department of Physics and Astronomy at the University of South Carolina and the respected professors and staff, specifically Sam Beals and Beth Powell.

I want to extend my sincere gratitude to our collaborators: Dr. Karen Livesey from the University of New Castle in Australia and Jonathon Davidson from the University of Colorado, for their help with simulations for our experimental observations, and Dr. Andrew Greytak, Dr. Mathew Kelley, and Jennii Burrell, from the University of South Carolina for their help with quantum dot self-assembly experiments. Special thanks to Dr. Mark Freeman for his suggestion to look into the hexatic phase self-assembly. Thank you, Dr. Thompson Mefford, from Clemson University, Dr. Erica Vreeland, and Mee Wa Wong from Imagion Biosystems for providing magnetic nanoparticles. I am also grateful to my office mates, Dr. Bryan L. Chaves, Dr. Sara Fitzgerald, Dr. Cory Dolbashian, Dr. Longfei Ye, Adam Fisher, and Heath Smith, for their support throughout this journey.

Lastly, I would be remiss in not mentioning my family, especially my beloved spouse Nilab, children Liana and Elena, parents, siblings, nephews, and nieces. Their belief in me has kept my spirits and motivation high during this process.

Abstract

Magnetic nanoparticles have been extensively studied over the last half century and continue to sustain interest due to their potential use in different fields. This research explores Magnetic Field Directed Self-Assembly of magnetic nanoparticles using a magnetic disk drive. The magnetic fields generated by the bits in a magnetic disk drive have rapidly changing field gradients that can self-assemble magnetic nanoparticles into various shapes. We demonstrate the ability to record and read field gradients on a commercial disk drive medium and to use monodisperse iron oxide nanoparticles to achieve self-assembly. We use image analysis techniques to quantify parameters related to self-assembly, and real-time optical measurements to monitor changes in optical diffraction signal as nanoparticles self-assemble into two-dimensional parallel arrays. In addition, we compare our experimental results to Langevin dynamics simulations and show that small changes to the magnetic or colloidal force change the self-assembly from ordered hexatic phase assemblies to disordered features. Our results demonstrate the ability to precisely control and tune the self-assembly of magnetic nanoparticles to achieve features with sub-200 nm resolution for various applications.

Table of Contents

List of Tables

List of Figures

Chapter 1

Motivation and Introduction

I was inspired to pursue a degree in experimental condensed matter physics when I listened to Richard Feynman's lecture "There's Plenty of Room at the Bottom." His quote became a roadmap for what we know today as nanoscience. Nanoscience is the study of structures and materials with unique and exciting properties on ultra-small scales.[17] In the last couple of years of my research, I have realized that there is plenty of room as we explore the world's smallest scales, and the deeper we dive to the bottom, new physics phenomena with unique properties appear. Physics at the nanoscale differs from bulk materials because nanomaterials have a significantly higher surface-to-volume ratio. For example, a cube with 1 nm size on each side has a surface area of 6 nm^2 and a volume of 1 nm^3, which makes it surface-to-volume ratio 6:1. In contrast, a cubic particle of 2 nm sides with 6×4 nm^2 surface area and 8 nm^3 volume has a surface to volume ratio of 3:1. Therefore, the smaller materials get, the surface area increases. As a result, the surface effects get more dominated and quantum effects influence materials' properties.

Today Nanoscale Physics is considered a branch of Condensed Matter Physics which is a collaborative venture between multiple disciplines such as Chemistry, Biology, Material Engineering, Electrical Engineering, etc. This field of physics plays a crucial role in achieving nanoscale functional materials.[87]

Top-down and bottom-up approaches often achieve material fabrication at such a nanoscale. In top-down methods, crystals from materials are removed layer by layer to achieve well-ordered nanostructures. This is usually done by Electron Beam

Lithography (EBL), which yields atomic-scale precision, but this method is expensive for large-scale patterning, and achieving periodicity and high reproducibility is challenging [63]. In the bottom-up approach, nanostructures are fabricated using single atoms or molecules as pieces forming a larger assembly ranging from single to a few micrometers. [55]. Today, electronic components reach below 10 nm in length scale with top-down methods. Bottom-up self-assembly is also limited at scales beyond 100 nm because the larger structures get, the more defects in the structures become more dominant. An optimal limit is required where both top-down and bottom-up approaches are used for nanomanufacturing. As a well-known bottom-up approach, the self-assembly of nanoparticles allows large-scale nanofabrication with high control and nanoscale precision. [58]

This research explores the self-assembly of magnetic nanoparticles and how they interact when placed in an extreme magnetic field gradient found on a disk drive media. In this approach, colloidal particles above the patterned disk drive medium are pulled down to its surface by sizeable magnetic field gradients that occur when the medium magnetic moment switches direction, also known as a transition or "bit".

Initial investigation of Magnetic Field Directed Self-Assembly (MFDSA) involved using a Longitudinal Magnetic Recording media (LMR); a media that was used in old disk drives, where the magnetic moments are oriented in-plane to the disk. The goal was to develop a low-cost nanomanufacturing alternative to fabricate nanoparticle-based diffraction gratings and monitor the self-assembly of aqueous nanoparticles via changes in the diffraction signal in real-time. [21], [42], [41] [86]

Modern disk drives store approximately 105 Gbits in a single square centimeter, a density enabled by a technology known as Perpendicular Magnetic Recording (PMR). [45] Because of the higher aerial density and sharper transitions in Perpendicular Magnetic Recording media (PMR), the MFDSA studies transitioned from using LMR as a template to PMR. Also, MFDSA of aqueous magnetic and non-aqueous nanoparticles

onto pre-recorded templates on PMR media with fixed spacing (750 nm) was studied, and the magnetic properties and the growth of nanoparticles as a function of time were explored in detail.[66] The PMR media was also used to record user-defined magnetic templates for self-assembly into various shapes.[94] For all these experiments, self-assembly happens due to single and fixed magnetic transitions. The next chapter will cover basics of self-assembly and these magnetic recording techniques.

Magnetic transition of the disk drive media is one of the critical elements of this type of field-directed self-assembly, and in this research, we explore and cover its importance in detail. One way to tune and control self-assembly is to add and adjust the spacing between transitions. Unlike previous experiments where a single transition was obtained by raster scanning the write head to obtain a region with all up magnetization and an adjacent region with all down magnetization, here we completely erase the disk drive medium with a very high external magnetic field; thus, achieving media with all the magnetic moments aligned in one direction. Then, we record a single stripe by dragging the write head once to achieve a region of opposite magnetization and two transitions with the width corresponding to the write head.

Based on our initial hypothesis, with two transitions, we expected to see self-assembly of two distinct features, i.e., two arrays of nanoparticles equally spaced apart. However, our experimental results show a single array covering the region between two transition. Our collaborators Dr. Karen Livesey and Jonathon Davidson, confirmed this hypothesis with simulations. The existence of a wide self-assembled stripe spanning both transitions that was observed experimentally puzzled us for many months. Turning our attention to the chemistry of nanoparticles solution and properties of the magnetic recording medium, we have learned that slight changes to the diameter of nanoparticles and a soft magnetic layer of the disk drive medium can drive self-assembly from a single feature to two distinct features. These results that are recently been accepted for publication in Advanced Materials Interfaces journal,

are explained in detail in Chapter 3.[20]

In chapter four, we discuss additional tunable parameters and quantify width growth, edge defects, and non-specifically self-assembly as a function of periodicity and spacing between recorded stripes, applied voltage to the write head, and lubrication of the disk drive medium. We explore the reason behind the bridging of nanoparticles when recorded stripes are close together and the formation of double layers when they are far apart.

We quantitatively calculate parameters related to nanoparticle order and the possibility of achieving hexatic self-assembly in chapter five. The hexatic order happens in specific spacing where the edge roughness of the nanoparticles arrays and the number of non-specifically assembled particles are minimal. Our experimental results with 25 nm diameter iron oxide nanoparticles show that these defects and order in self-assembly can also be tuned.

To further investigate the cause of these defects, we employ a read head to map out the fields due to the underlying magnetic templates. These measurements are covered in chapter six. And finally to better understand the overall dynamics of the process, in chapter seven, we cover results from real-time self-assembly monitoring of nanoparticles optical diffraction.

Chapter 2

Basic Concepts

2.1 Self-Assembly of nanoparticles

Self-assembly of nanoparticles is a process in which nanoparticles organize into complex structures. The particles are guided to specific locations by a balance of attractive and repulsive forces that result from their electric, magnetic and surface properties. Self-assembly or bottom-up method of fabrication utilize physical forces and interactions to arrange superstructures that span many hierarchical levels and help scale up from the nano to the macroscale. [74], [84], [4], [73] Nanoparticles act as building blocks for the fabrication of more advanced materials when mixed with other materials, such as super-conducting wires, semiconducting quantum emitters, and nanocrystal superlattices with tunable optical properties. [39],[16]

In general, nanoparticle self-assembly can happen in two ways: It can happen due to their intermolecular interactions, such as covalent and noncovalent bonding with their capping ligands, and Van der Waals forces where the system tends to achieve its lowest energy state. [34],[11] Self-assembly can also happen due to external fields where nanoparticle assembly is driven by an external electric, shear, and magnetic forces. [23], [46]

Magnetic Field Directed Self-assembly (MFDSA), which is the main purpuse of this research, is a technique where magnetic nanoparticles (MNPs) are guided to self-assemble into ordered 1D chains, 2D layers, and 3D stacked materials with the help of external magnetic field.[73],[31],[26],[88] These assembled structures represent a

new class of advanced materials whose properties are determined by a combination of intrinsic nanoparticle properties, mutual interactions, and nanoparticle interactions with external fields. [74],[8]

2.1.1 Magnetic Nanoparticles

Colloidal magnetic nanoparticles under the influence of external fields are mostly used in bottom-up self-assembly. When placed on external magnetic fields, MNPs arrange into nano- to mico-meter size assemblies. [62], [76], [70] MNPs with controlled diameter and surface properties have been synthesized for specific applications including information storage, photonic crystals, cancer therapy, targeted drug delivery and bio-engineering.[40],[83],[67],[61],[28] Materials with higher saturation magnetization are preferred in bio-sensing due to their higher sensitivity and efficiency [52]. Materials with larger coercivity are preferred in magnetic storage devices to avoid the random flips caused by demagnetizing or stray field of the material. Furthermore, one wants to have a large enough remnant magnetization for data storage so that moments are not flipped upon removal of the external field.

The crystal structure of magnetic nanoparticles gives detailed information on their magnetic properties. The most commonly used magnetic nanoparticles are Iron Oxide nanoparticles such as magnetite Fe_3O_4, maghemite γFe_3O4, or hematite αFe_2O3. Iron oxide nanoparticles present a non toxic alternative to other magnetic nanoparticles and thus are widely used in medicine for drug delivery, cell targeting and cancer therapy. [80]. Further details on crystal structure, magnetic properties of nanoparticles, and steric interaction can be found in Appendix A.

A number studies showed that the synthesis and controlling of iron oxide nanoparticles through their preparation had been known to be a factor in the final magnetic properties of nanoparticles. The most evident changes as nanoparticle size decreases are the surface effects. The spins of a magnetic nanoparticle can be viewed as a

core-shell structure, where the surface spins are canted or disordered because of the incomplete coordination, and broken symmetry. [6], [69],[33] ,[95],[35] Several theoretical and experimental efforts have explored magnetic field-driven self-assembly of these particles.[92],[79] Examples include self-assembly via field gradients from an electromagnet, a nickel micro-grid array, a ferrite garnet film, and helical magnetic fields .[24],[85],[90], [2],[81] However, achieving highly ordered structures with single-nanoparticle precision is still elusive experimentally and requires improved understanding to precisely control the balance between external magnetic field gradients and inter-particle colloidal forces.[65], [6], [82]

Magnetic nanoparticles that we use in this research are highly monodisperse 25 nm oleic acid capped magnetite nanoparticles. These particles are well known for their high colloidal stability in non-polar solvents such as hexane. The carboxylic acid group of oleic acid binds to the magnetite while the aliphatic chain extends out into the non-polar solvent, thus providing steric force between the particles. [38]

2.2 Interactions During Self-assembly

Nanoparticles are often considered as scale models of atoms but there are notable differences between them. Firstly, the forces between colloidal nanoparticles are differ greatly from those between atoms. Secondly, unlike atoms that exhibit ballistic motion in vacuum, colloidal particles undergo Brownian motion without a well-defined velocity. [59] Predicting the self-assembly of colloidal nanoparticles computationally is very challenging because such tiny particles are influenced not only by a complicated superposition of deterministic forces, but also by random Brownian forces and torques. External magnetic or electric fields can be applied to provide additional controllability of self-assembly of nanoparticles. [60]

Some of the interactions during self-assembly are: magnetic force due to external field source $\vec{F}_m$, force due to gravity $\vec{F}_g$, viscous drag force $\vec{F}_d$, inter-particle effects such as dipole-dipole interaction $\vec{F}_{dd}$, electric double layer force $\vec{F}_e$, steric force $\vec{F}_a$, Van der Waals forces $\vec{F}_{vdw}$, etc. Langevin's model is the most common approach to predict particle's motion in a magnetophoretic system [92].

$$m_i \frac{d^2 x_i}{dt^2} = \vec{F}_{b,i} + \vec{F}_{m,i} + \vec{F}_{d,i} + \vec{F}_{g,i}(t) + \sum_{j=1}^{N} (\vec{F}_{dd,ij} + \vec{F}_{vdw,ij} + \vec{F}_{a,ij} + \vec{F}_{e,ij}) \qquad (2.1)$$

Further details about these interactions can be found on Appendix A.2.

2.3 Magnetic Recording Technology

Using magnetic recording media as a template for self-assembly is powerful and cost-effective technique. Here we go briefly on the process and some properties of magnetic recording media. The critical measure of magnetic recording is areal density. Data on magnetic recording media is stored through recording certain spatial variations of magnetization [50].

There are two types of recording systems:

Longitudinal Magnetic Recording (LMR): In this kind of magnetic recording, the preferred direction of the magnetization i.e., easy axis, lies in the plane of the recording layer. Using an inductive 'ring-type' writer, the magnetization of the grains is aligned along the track in either a positive or negative direction. Change in magnetization is represented by "0" and "1".

Perpendicular Magnetic Recording (PMR): In this kind of magnetic recording, the easy axis lies perpendicular to the recording layer and is typically written with a Single Pole Head (SPH). Schematic representation of both LMR and PMR is shown in Figure 2.1.

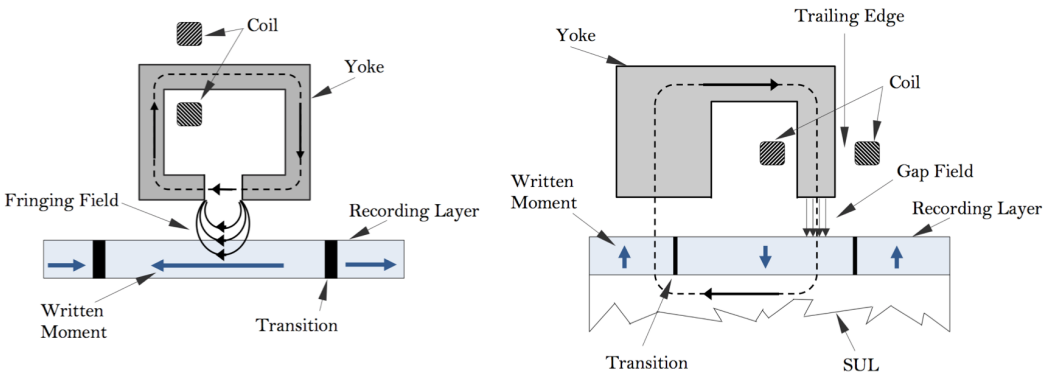

Figure 2.1 Schematic representation of longitudinal (left) and perpendicular (right) recording (reproduced with permission from [50])

The geometry of the 'ring'-type recording head in LMR defines the upper limit of the writing field of $2\pi M_s$, where M_s is the saturation magnetization of the write pole material. However, in PMR media, the upper limit of the write filed is doubled or $4\pi M_s$ because it is generated between the trailing pole of a single-pole head and a Soft Under-Layer (SUL).

Several aspects make perpendicular recording superior to the longitudinal recording, such as higher areal density, sharper write field gradients, absence of demagnetizing fields, etc. According to the law of scaling, higher areal density require smaller grain sizes. However, reducing grain size can cause a superparamagnetic effect, especially in longitudinal media where the demagnetizing field achieves its maximum. A typical magnetic medium consists of magnetic granular structures made of polycrystalline material, which are randomly packed.

For a media to be thermally stable, energy barrier or KV should be substantially greater than or equal to 40 times than the energy of a single quantum of thermal fluctuation k_BT [15]. For example, for a Co-based thin film medium with anisotropy constant $K = 2 \times 10^6 erg/cm^3$ and $T = 300K$ and $k_BT = 1.14 \times 10^{-}14erg$ the minimum volume V for a grain should be greater than 800 nm^3.

Most of perpendicular magnetic recording media are divided in two types: 1) Alloy

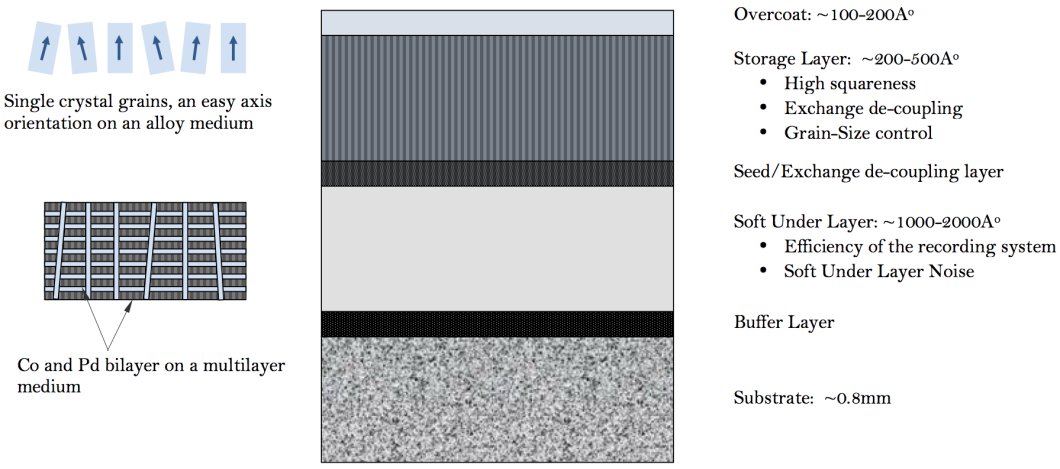

Figure 2.2 Perpendicular Magnetic Recording (PMR) media layers [89]

based media such as CoC-alloys and 2) media based on magnetic multilayers (Figure 2.2), such as Co/Pt, Co/Pd or other materials. In general following properties are required for high density magnetic recording media:

- *High Coercivity*, to accommodate very sharp transitions.
- *High Remanent Magnetization,* M_r, to provide large enough readback signals.
- *Nearly Squared hysteresis loop*, to achieve sharp transition and satisfactory overwrite ratio.
- *Smooth Surface and reliable mechanical stability*, to attaining small magnetic spacing with acceptable tribological performance.

In this research we use perpendicular magnetic recording media as a basis for magnetic field directed self-assembly. Magnetic fields of magnetic recording media is analytically evaluated by principle of linear superposition and Laplace's equation. The details on calculation of the gradient forces due to a single and double transitions are mentioned in Appendix A.3.

Chapter 3

Tunability in Two-dimensional arrays of Magnetic Nanoparticles Assembled via Extreme Field Gradients

In the previous chapter, we mentioned the possibility of self-assembling nanoparticles from colloid onto perpendicular hard disk drive media at locations where the magnetization switches from up to down. This is due to the extreme magnetic field gradients above these so-called transitions. Previously, magnetic nanoparticles were always seen to assemble directly above transitions in theoretical and experimental studies. Here, we instead show experimentally that when there are two transitions close together – say at the two edges of a long reversed stripe region of the recording media – then the self-assembly may fill the stripe region, rather than forming two distinct lines above the two transitions. We compare our experimental results with Langevin dynamics simulations performed by our collaborators Dr. Karen Livesey and Jonathon Davidson, and find that the magnetic underlayer of the hard disk drive media results in this broad quasi-2D ordering of the specific 25 nm diameter monodisperse particles. By changing the polarity of the solvent, the deposited nanoparticles form two disordered lines above the two transitions. In this way, the self-assembled structures can be tuned by changing the magnetic recording media and/or the colloid characteristics by small amounts. [20]

3.1 Preparing Magnetic Templates

To prepare the media we uniformly magnetize, i.e. erase, a commercial disk drive medium (Figure 3.1 a). Then we record the medium with a single pass of the recording head, yielding a reversed magnetization region along a line whose ~ 100 nm width is determined by the write head's physical width (Figure 3.1 b).

This process creates a 'stripe', that consists of two 3-4 nm wide transitions between "up" and "down" magnetization, spaced approximately 100 nm apart. This process is then repeated many times across the disk drive surface yielding multiple stripes or two-transition features. Medium is recorded with varying stripe spacing $d = 200$–$1600\ nm$ in order to test how the deposited features change with d. To deposit nanoparticles, the recorded medium is rotated and translated via automated rotating stage in a beaker containing nanoparticle solution of 25 nm diameter Fe_3O_4 nanoparticles stablized with oleic acid and suspended in hexane (Figure 3.1 c). More details on preparation of the medium and nanoparticles solution is mentioned in Appendix B.

With two transitions close together we expect to observe two separate lines of nanoparticles upon exposing the recorded pattern to a colloidal dispersion. The expected pattern is shown schematically in Figure 3.2 a (side-view) and as simulated using Langevin dynamics in Figure 3.2 b (top view), both for two stripes. Contradicting our hypothesis, experiments yield only single lines of self-assembled nanoparticles spanning the 100 nm stripe between the two transitions, independent of recorded feature spacing d. One such example is shown in Figure 3.3 (inset), a Scanning Electron Microscopy (SEM) image of the self-assembled particles for $d = 500$ nm. Two stripes are shown, each displaying a single assembly of particles rather than two as expected for two transitions. When exposed to white light at a fixed angle, rectangular regions with different spacing display colors due to diffraction. The differently colored bars in Figure 3.3 each correspond to many stripes all with the same spacing.

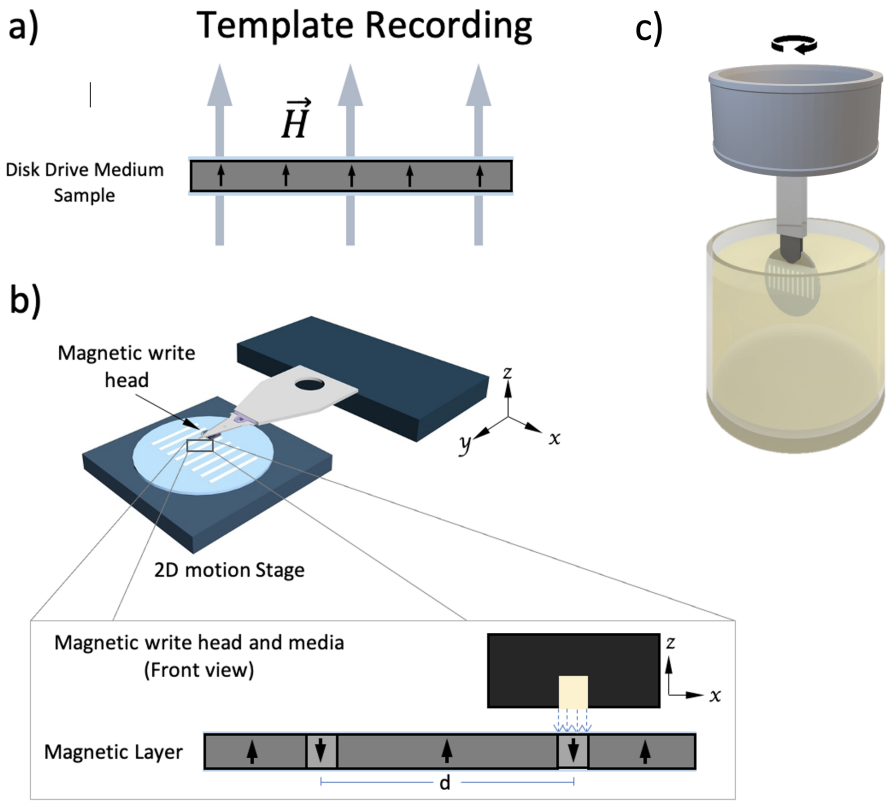

Figure 3.1 Template recording procedure: a) Disk drive medium is placed perpendicular to a large magnetic field to erase or align the magnetization in one direction. b) 3D sketch of the recording process using a write head and an erased disk drive medium on a 2D motion stage. A single stripe with opposite magnetization is produced by dragging the head slider the disk drive medium while applying current to the write head. (inset: Front cross-sectional view of magnetic head slider producing magnetic field to magnetize stripes with line spacing d.) c) the recorded medium is dipped inside a beaker containing nanoparticle solution and translated and rotated for 20 minutes via automated rotating stage. (3D graphics courtesy of Ghazal Mohtasebzada)

3.2 The Importance of Soft Under Layer

This hypothesis and the simulations supporting it, both shown in Figure 3.2, assume the only magnetic materials impacting nanoparticle assembly are the recorded grains that comprise the perpendicular medium. However, as mentioned in previous

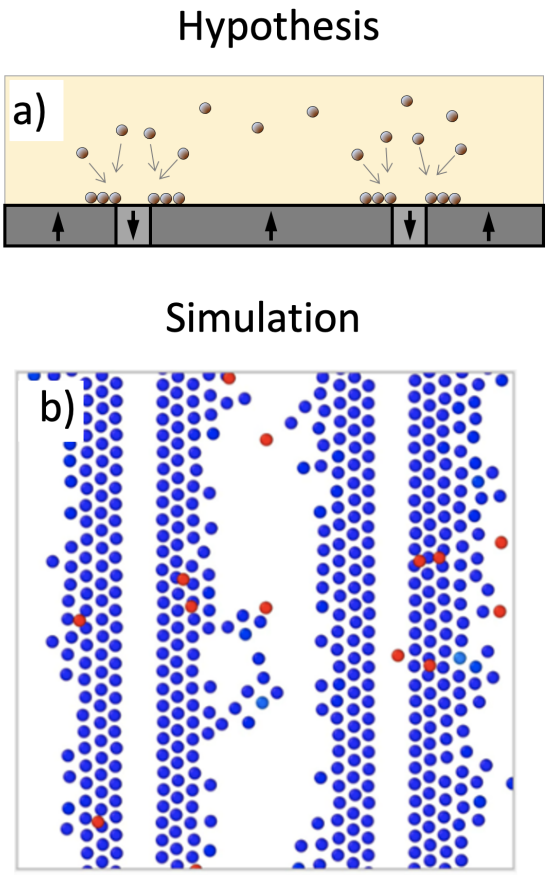

Figure 3.2 a) Schematic of self-assembled nanoparticles from colloidal dispersion on two side of a stripe based on hypothesis. b) Langevin dynamics-based simulations (top view) appear to confirm this hypothesis. Here the blue spheres are particles on the hard drive and red spheres are particles still suspended above in the colloid

chapter there is another, thicker magnetic layer beneath the recording layer in the perpendicular recording system .[89],[71] This soft underlayer (SUL), combines with the recording head during the write process, producing a magnetic 'image' of the write head below the medium to boost the size of the write field. Yet once recorded, the SUL also produces an image of the medium magnetization as well, which mod-

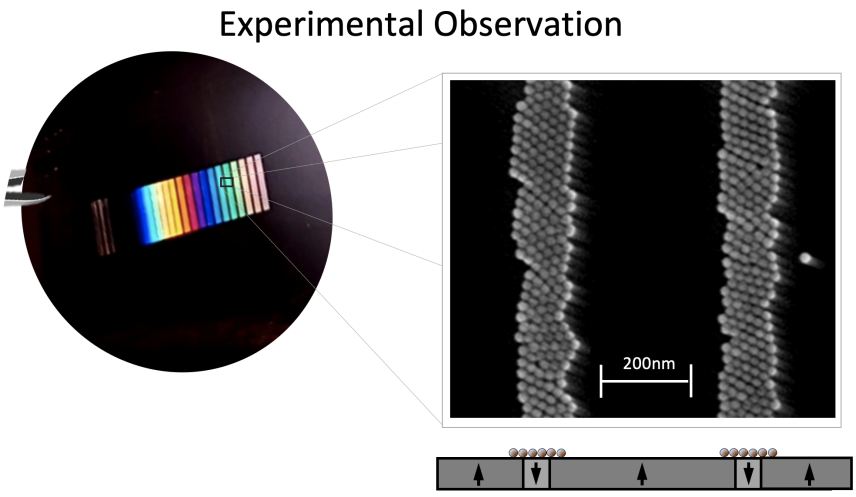

Figure 3.3 Photograph of the resulting media displaying diffracted light from the nanoparticles arrays (left), and Scanning Electron Microscopy (SEM) image of nanoparticle arrays filling two entire stripes that are separated by $d = 500$ nm.

ifies the field above the medium. Therefore it must be included in simulations to model the true effect of the medium stray field on self-assembly. In fact, we found that including the SUL was necessary to obtain agreement between simulations and experiment. To illustrate the SUL's importance, Figure 3.4 shows spatial maps of the magnetic field magnitude for an isolated stripe without (panel a) and with (panel b) the SUL. The color contours show the field magnitude. The black arrows depict the magnetic force on a nanoparticle in space above the medium and suggest stronger forces localized to the two transitions in panel a, but a wider and overwhelmingly downward force centered between the transitions in panel b. Note, to calculate the analytic magnetic force on the particles one can assume the nanoparticle moment is pointing in the same direction as the medium field due to its high magnitude when the particles are close to the surface [29]. One can see how particles are pulled away from the center and toward the two transitions when the SUL is absent (Figure 3.4 a), but uniformly downwards across the ~ 100 nm wide stripe region when the SUL's

effect on the magnetic field gradient is included (Figure 3.4 b).

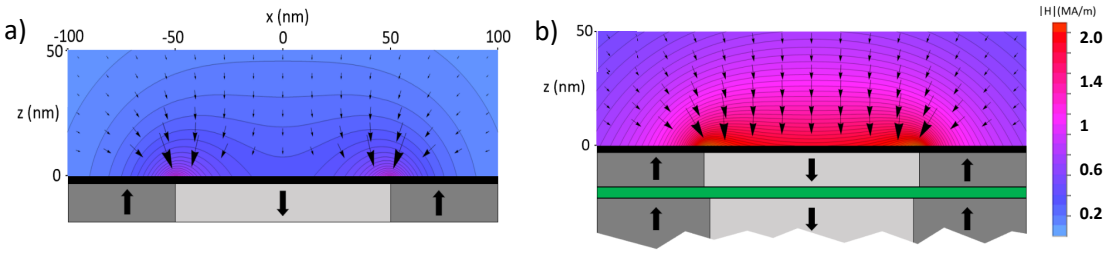

Figure 3.4 The magnitude of the field of the given substrate with a) the field due to the hard layer and b) the field of the hard and soft layer. The black arrows over the plot are the direction and magnitude of the force on the MNPs. The geometry of the hard and soft layer are shown underneath the plots to show the location of the magnetic regions with the black region being a nonmagnetic coating over the substrate and the green being an exchange breaking layer between the hard and soft layers. The separation of magnetized region in both these plots are d = 1000nm. (Courtesy of K. Livesey and J. Davidson)

As shown in Figure 3.3, 25 nm diameter particles tend to assemble into single lines of particles. The upper two panels in Figure 3.5 show Scanning Electron Microscope (SEM) images of self-assembled nanoparticles while the lower panels show simulations of self-assembly that include the SUL. Panels a and b show stripes with $d = 500\ nm$ and $1000\ nm$, respectively. Increasing stripe spacing to $1000\ nm$ increases the number of particles assembled per stripe (pattern width) and causes a second layer of nanoparticles to self-assemble on top of the first layer. Panels c and d show similar assemblies in the simulations, with second layer formation occurring at $d = 500\ nm$ spacing and nearly a complete second layer at $d = 1000\ nm$. For the current experimental conditions, the second layer forms when line spacing is increased beyond 700 nm, i.e. where the forces are increasing.

3.3 Sensitivity of self-assembly to the diameter of particles

To demonstrate the sensitivity of the assembly process, we reduce the hydrodynamic radius of the nanoparticles. In a non-polar solvent like hexane the hydrophobic alkyl

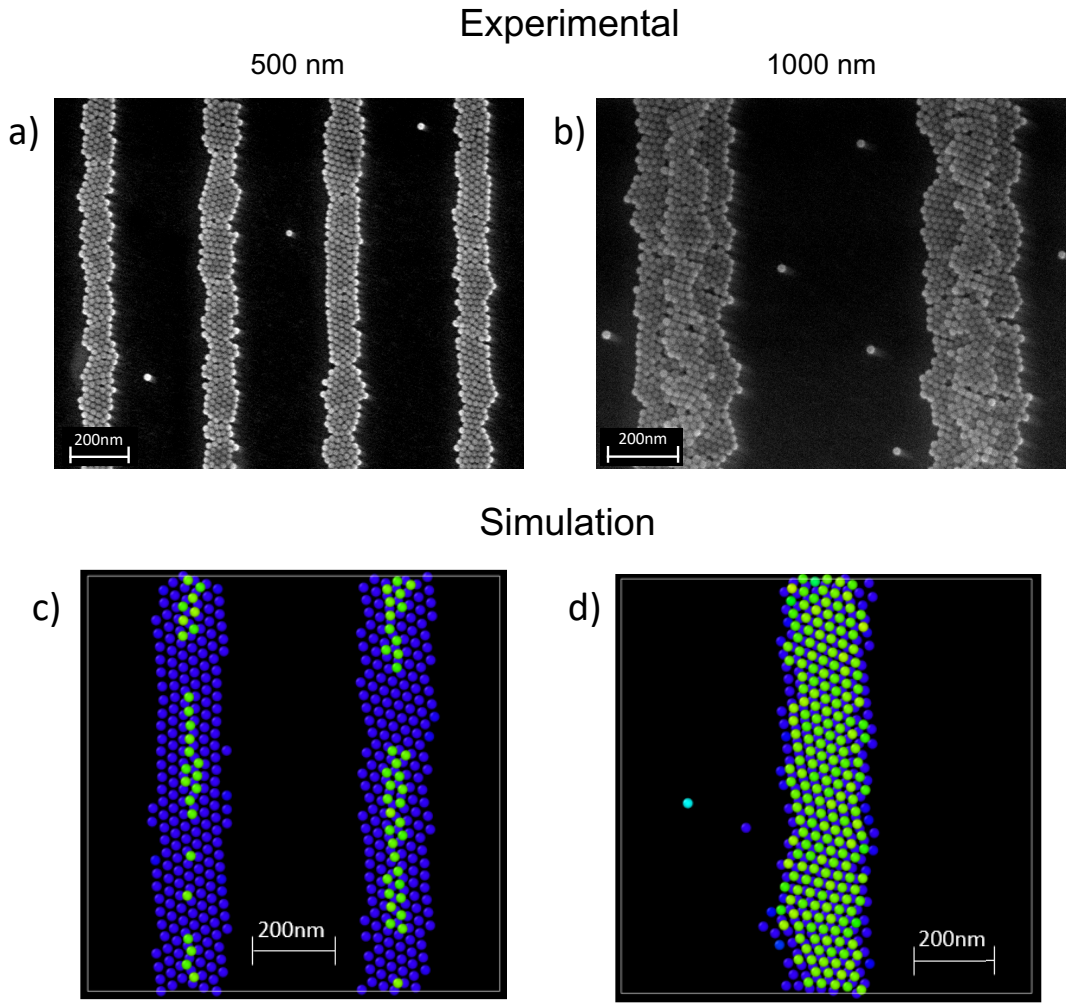

Figure 3.5 SEM images of self-assembled iron oxide nanoparticles in hexane solution compared to simulations for 500 nm spacing (a and c) and for 1000 nm spacing (b and d)

chains of the oleic acid dictate the nanoparticle-solvent interface, making solvent-ligand interactions energetically favorable. It has been shown via molecular dynamics simulations that interactions between polar solvents and oleic acid ligands decrease the tail extension length by half, reducing hydrodynamic size and affecting nanoparticle self-assembly. [30],[56] While these studies looked at hexane and ethanol sep-

arately, they indicate what will occur when ethanol is added to hexane. Therefore, we add ethanol (2% by volume) to our hexane solution and measure how the modified colloid affects the resulting nanoparticle patterns. The features in Figure 3.6 a demonstrate that the nanoparticles are no longer hexagonally close-packed. More importantly, they no longer form a single stripe, but rather a gap opens at the center of the stripe. We hypothesize that the reduction of the effective nanoparticle diameter caused by adding the ethanol transforms the assembly pattern from a single line into two mostly-distinct assemblies with loss of quasi-crystallinity.

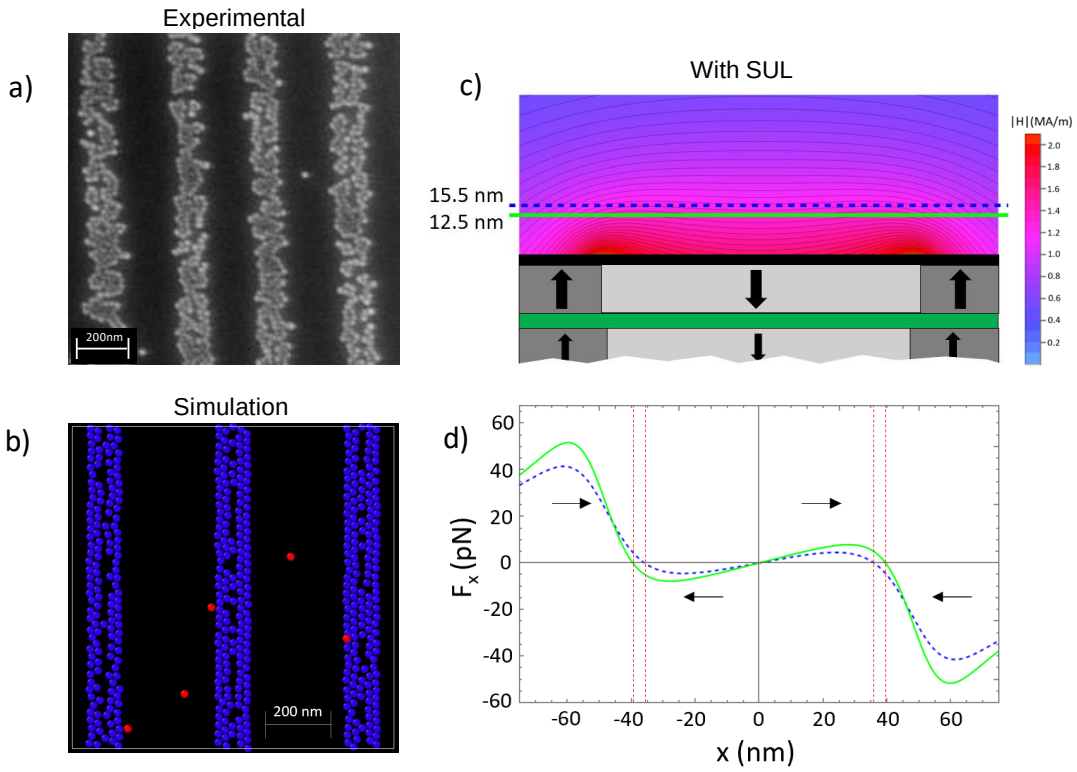

Figure 3.6 SEM images compared to simulations for self-assembly of iron oxide nanoparticle in hexane with added ethanol for d=400 nm (a and b). c) Field magnitude with both hard and soft layer for d = 400 nm (the lines are referenced in panel d). d) Horizontal force on the MNPs at heights 15.5 nm (blue dashed line) and 12.5 nm (green solid line) above the disk surface. The red dashed lines show the stable equilibrium positions.

These two changes in the assembly are also observed in simulations (Figure 3.6 b) where the only alteration to the computer program was to reduce the particle hydrodynamic radius from 15.5 nm to 12.5 nm, to mimic the reduction of ligand length caused by adding the ethanol. The ligand length appears explicitly in the equation for the steric repulsion, (Equation (A.15) of Appindex A.1) and thus this length changes the overall effective Lennard-Jones interaction between particles, making it more attractive and making the equilibrium separation of particles smaller. The features formed are less disordered in simulation compared to in experiment, again likely because in simulation all particles are perfect spheres of the same size. Note that deposited particles are blue in Figure 3.6 b and a few particles still in colloidal solution are red. The changes to the self-assembled features caused by reducing the particles' hydrodynamic size can be explained as follows. Figure 3.6 c shows a contour plot of the magnetic field magnitude including both the hard layer and SUL, for stripes with $d = 400$ nm. Only one stripe is shown, with magnetization down. Two horizontal lines are drawn at heights of 15.5 nm (blue dashed line) and 12.5 nm (solid green line) above the medium surface to indicate where the center of a particle is located when deposited: in hexane (15.5 nm) and with the addition of ethanol (12.5 nm). Figure 4d then shows the in-plane component F_x of the magnetic force at these two heights (horizontal lines in panel c). The force outside the stripe (that is $|x| > 50$ nm) drives particles inwards toward the stripe, as indicated schematically by the black arrows. The force inside the stripe region ($|x| < 40$ nm) instead weakly pushes particles outwards towards the transitions. At a height of 15.5 nm (hexane), the maximum horizontal force inside the stripe is 7 pN, while for a height of 12.5 nm (with the addition of ethanol) it has a maximum of 10 pN. In other words, there is a larger force driving particles outward from x=0 and towards the transitions. Furthermore, the particles are able to pack more tightly together when their hydrodynamic diameter is reduced, meaning that geometrically there is room for a single-particle

width gap in the assembly above the center of the strip at $x = 0$. There is no room for such a gap when the particles are larger. Computer simulations confirm this explanation for the different self-assembly behaviors. For example, our collaborators ran simulations for artificial scenarios where the magnetic particles have increased Lennard-Jones attraction, as also occurs with a reduced ligand length, and with various hydrodynamic sizes. Changes in the Lennard-Jones strength could not reproduce the different assembly structures, while the reduced hydrodynamic size could.

Apart from filling the entire stripe, another important observation of nanoparticles from SEM images, particularly in Figure 3.5 a and b, is the formation of second layers, non-specific assembly between line, and rougher edges as the spacing increases. There are several ways to control the formation of the second layer, including by controlling nanoparticle deposition time, employing particles with different diameters, or changing the medium thickness. Furthermore, both simulation and experiment show the particles form a two-dimensional "hexatic" array within a single layer and a hexagonal-close-packed array if there are multiple layers. The hexatic arrangement is more perfect in simulation because the particles all have the same size, which is not true in experiment. The match between experiment and theory will be made quantitative in the coming chapters.

Chapter 4

Space Dependence and Structural Charectarization of Self-assembly of Iron Oxide Nanoparticles

Having demonstrated the extreme sensitivity of self-assembly templated by disk drive media to field and nanoparticle geometry, both theoretically and experimentally, we next demonstrate the sensitivity to feature spacing with d varying from 200 nm–1600 nm for both cases: with and without added ethanol. We also include the smaller stripe spacing for 50 nm and 100 nm, and larger spacing 1900 nm and beyond in the same disk drive medium and same nanoparticles solution.

4.1 Space dependence in pure hexane solution

Dark field optical microscopy was used to confirm the dimension of each rectangular region and Zeiss Gemini500 Field Emission Scanning Electron Microscope (FE-SEM) was employed to check the self-assembly for each pattern within the sample. No distinguished lines are noticed for the first two rectangles, i.e., the regions with 50 and 100 nm spacing, because the write head dimensions are between 50 to 100 nm and the fringing fields due to the head overwriting the magnetized regions. Only at 300 nm spacing is where nanoparticle arrays start to distinguish; however, at this spacing still, nanoparticles are bridging the adjacent lines near the edges.

This is best seen when comparing the corner of the rectangular regions. Figure 4.1 shows the corner for the rectangles with 50 nm spacing (Figure 4.1 a), 100 nm

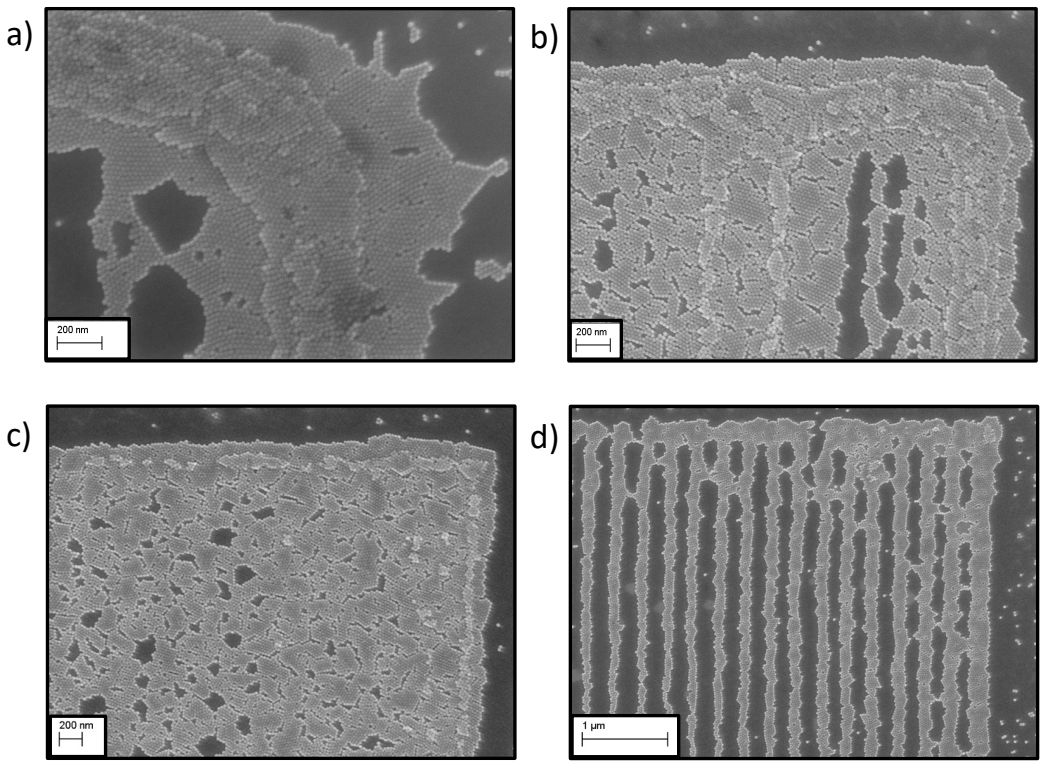

Figure 4.1 SEM images of nanoparticles self-assembled at the corner of the rectangular regions with spacings: (a) 50 nm, (b) 100 nm, (c) 200 nm, and (d) 300 nm spacings

spacing (Figure 4.1 b), 200 nm spacing (Figure 4.1 c), and 300 nm spacing (Figure 4.1 d). As seen in this figure, at 50 nm spacing, nanoparticles in the edge of the rectangle self-assemble in multilayers, where the first layer covers a large area. Although the edge assembly is not defect-free, however; crystalline assembly with high order is very noticeable. The multilayer assembly is still noticeable at 100 nm spacing but gets less noticeable at 200 nm spacing and disappears at 300 nm. At 200 nm spacing, self-assembly in the corner of the rectangle is almost entirely covered by 'super-crystal-like' assemblies of nanoparticles with different orientational orders. Figure 4.1 suggests that by changing the spacing between the magnetic stripes, one can

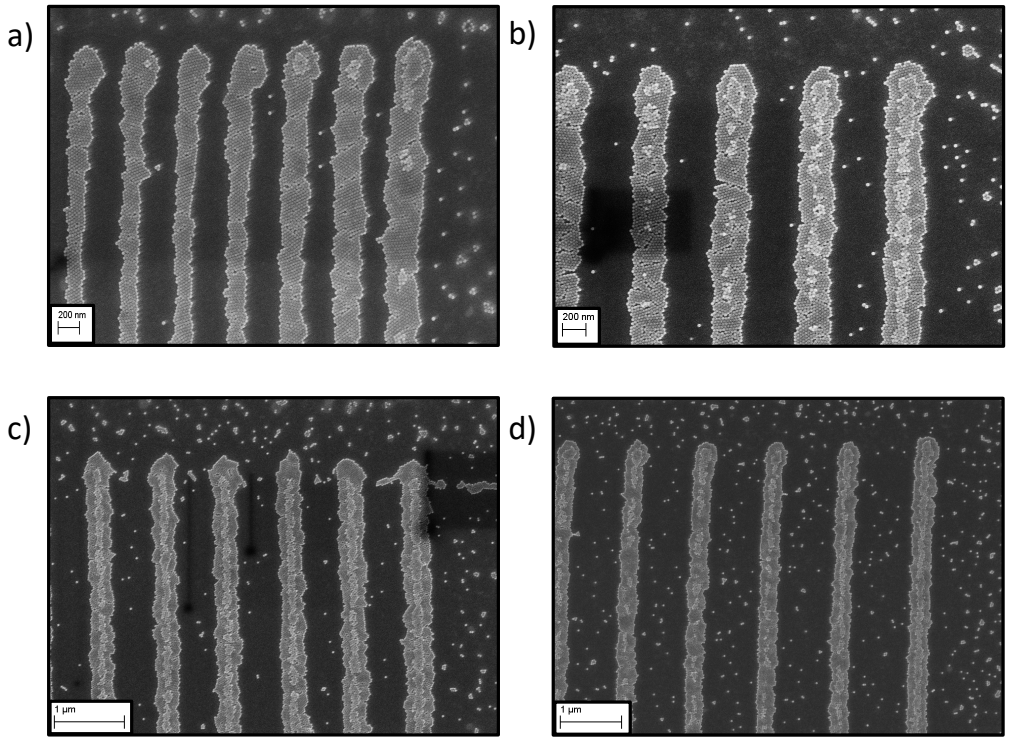

Figure 4.2 SEM images of nanoparticles self-assembled at the corner of the rectangular regions with spacings: (a) 500 nm, (b) 700 nm, (c) 1000 nm, and (d) 1500 nm spacings

control self-assembly to achieve a rectangular region with sharp edges filled with a monolayer of particles. When the spacing increases to 500 nm, lines are separated and do not bride. The first few lines in the rectangle are wider and bridged because of the large opposite magnetization region near the edges. Therefore, to quantify structural properties such us width growth and edge roughness of arrays, one must consider the most central region within each rectangle. Figure 4.3 shows electron microscope images of the lines in the central area for the rectangles with 200 nm - 500 nm spacing. At 200 nm (Figure 4.3 a), magnetic nanoparticles assemble near transition and form long continuous arrays with an average of 2-3 nanoparticles width. Self-assembly at this spacing provides the first evidence of hexagonal nucleation of nanoparticles onto

parallel lines.

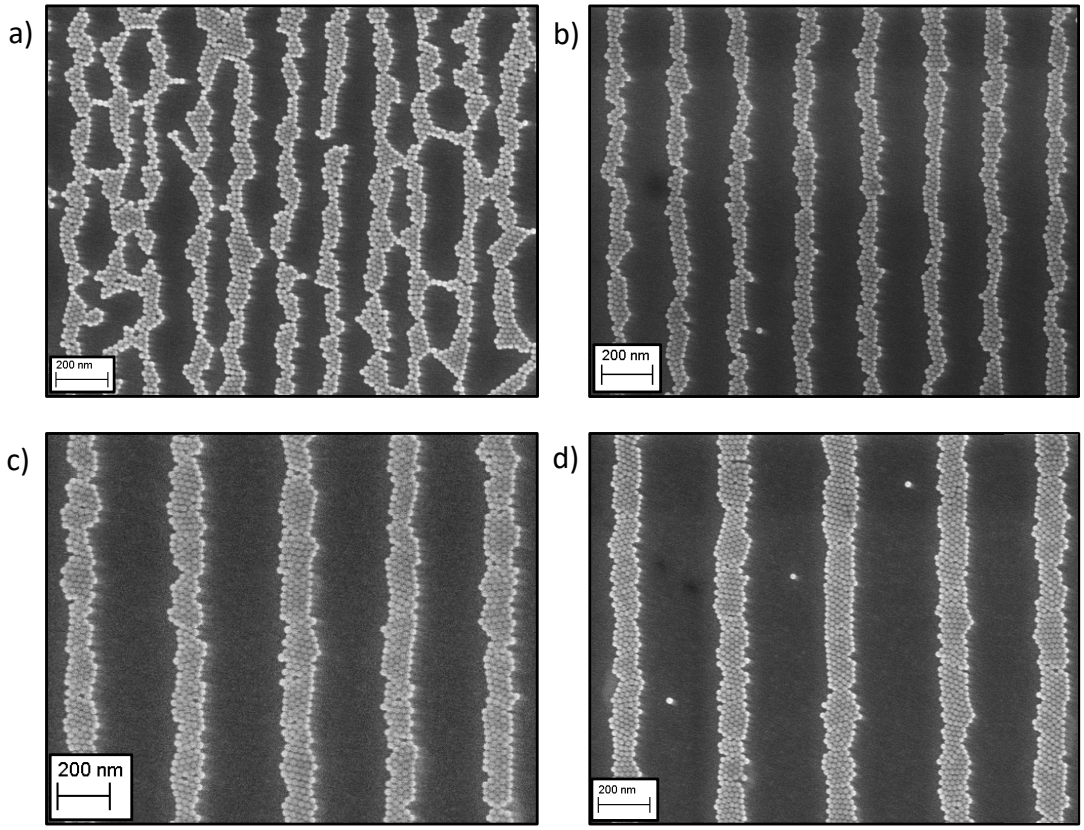

Figure 4.3 SEM images of nanoparticles self-assembly at: (a) 200 nm, (b) 300 nm, (c) 400 nm, and (d) 500 nm spacings

At 300 nm, spacing lines are distinct and have no particles or joined edges in between. In some regions, particles form a perfect line edge. In contrast, in other areas, they include triangular-tip edges and the possibility to self-assemble sub-100 nm feature sizes over a limited distance. As the spacing between arrays increased to 400 nm and 500 nm (Figure 4.3 b), the quasi-crystalline nature of self-assembly with hexagonal order is more pronounced. At this spacing, particles have minimal edge roughness and defects with no nonspecifically assembled particles between lines.

Bridging between adjacent strips for the smallest spacing $d = 200\ nm$ can occur because the interparticle attractive force is comparable in magnitude to the horizontal

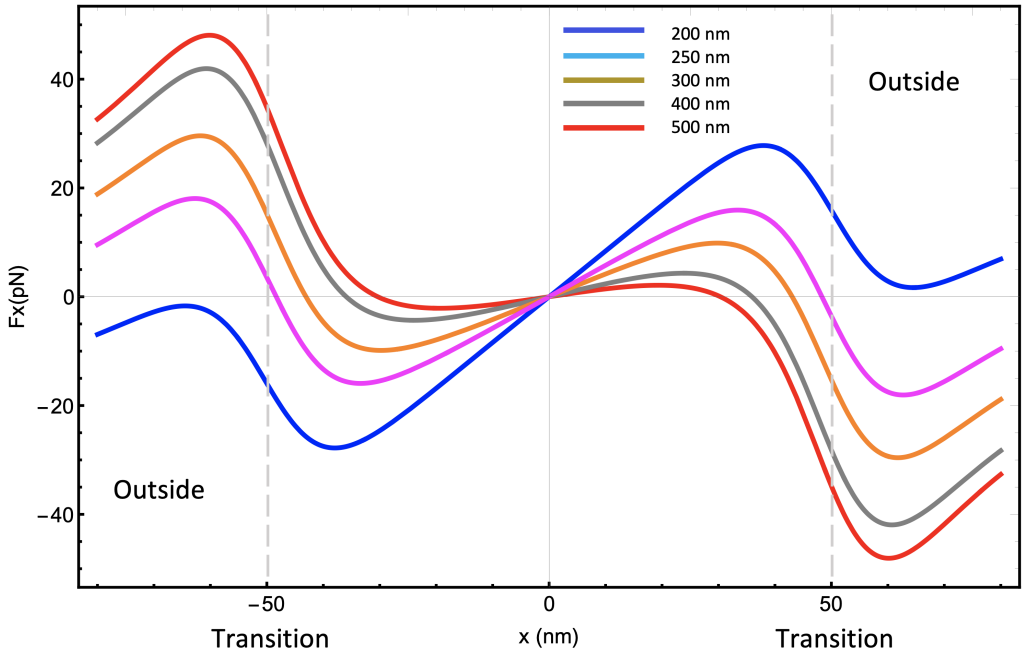

Figure 4.4 Horizontal force due to the magnetic field gradient for different spacing

component of the magnetic gradient force from the recording medium. The horizontal (in-plane) component of the magnetic gradient force is more significant for larger line spacings, meaning that particles are more likely to be pulled toward the strips rather than joining together to form bridges between the strips. Figure 4.4 shows the calculated horizontal component of the magnetic force for different line spacings. In the regions outside the transitions, the force pulling the particles towards the strip is lower in magnitude for $d = 200\ nm$ than $d = 400\ nm$. While the bridges between the adjacent stripes may make it hard to visualize the spacing, using averaged line profiles from the SEM images, the center-to-center spacing is 192 nm +/- 26 nm or approximately one nanoparticle. (Details on this measurement can be found in Appendix C.1)

At 600 nm - 700 nm (Figure 4.5 a - b), lines start to have discontinuity and form distinct nanoparticle "super-crystal-like" structures, each with distinct degree of

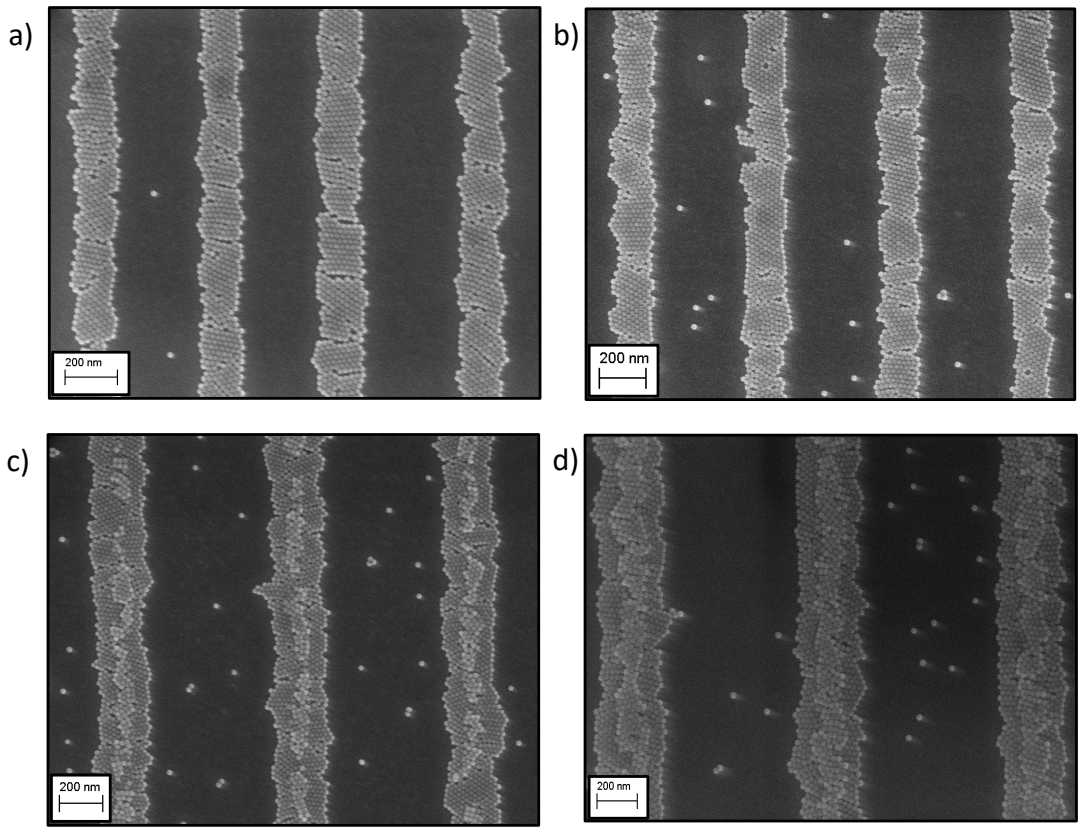

Figure 4.5 SEM images of nanoparticles self-assembly with: (a) 600 nm, (b) 700 nm, (c) 1000 nm, and (d) 1200 nm spacings

nucleation that grow as wide as $7-8$ nanoparticles on average. As spacing is increased to 1000 nm and 1200 nm (Figure 4.5 c and d, respectively) lines grow thicker, and nanoparticles start to self-assemble on second layers. At 1000 nm spacing and beyond, the width of the lines saturates with 9 - 10 nanoparticles.

When spacing is increased to 1200 nm and beyond, an intermediate assembly happens between the lines, where the horizontal magnetic force is minimal. This intermediate assembly happens when nanoparticles form a discontinuous line as they land halfway between two parallel lines. This is obvious in Figure 4.6, when the spacing is 1900 nm. Another significant observation from SEM images is that for spacings 300 nm to 600 nm, there are very few or almost no particles between the

lines. The number of non-specific assembled particles between the lines increases exponentially as the spacing is increased. The arrangement and different geometries that these nanoparticles assemble are shown in Figure 4.7. While there are few single nanoparticles at 300 nm to 600 nm spacing, the number of single nanoparticles, as well as doublets and triplets of nanoparticles, is exponentially increasing.

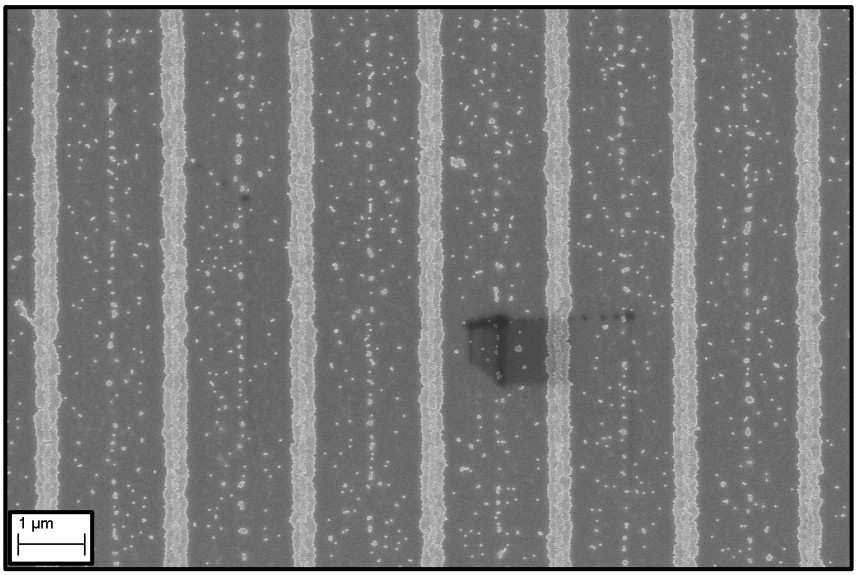

Figure 4.6 SEM images of nanoparticles secondary self-assembly between the lines at 1900 nm spacing

4.1.1 Effects of applied voltage on self-assembly

While the change in spacing between magnetized regions shows different self-assembly, the applied voltage to the write head is kept at 0.7 V for all spacings. Here we demonstrate how the change in applied voltage to the head affects the width growth of magnetic nanoparticles. We use the same disk drive medium, nanoparticle concentration, and coating time but change the applied voltage to the write head. Figure 4.8 shows nanoparticles self-assembled on a disk drive medium with 500 nm spacing,

Spacing [nm] / Type	300	400	500	600	700	800	900	1000	1100	1200
●	6	3	6	6	60	85	109	144	138	190
●●	0	0	0	0	10	17	28	34	27	51
●●	0	0	0	0	1	5	7	4	5	9
●●	0	0	0	0	1	3	6	3	4	8
●●●	0	0	0	0	2	4	4	1	1	11
●●●	0	0	0	0	0	1	2	3	3	4

Spacing [nm] / Type	1300	1400	1500	1600	1700	1800	1900	2000
●	195	205	146	147	163	0	208	0
●●	49	45	32	46	44	0	66	36
●●	21	16	13	16	28	0	15	36
●●	12	11	7	10	12	0	8	12
●●●	6	5	6	7	9	0	11	36
●●●	2	0	3	3	3	0	7	36

Figure 4.7 Different configurations and number of non-specifically assembled nanoparticles for different spacing

and patterns are written with different applied voltages to the write head. When 0.2 V is applied to the head (Figure 4.8 a), the media seem to be magnetized and produces a weak field gradient. As a result, nanoparticles' self-assembly is discontinuous, and many particles land non-specifically. As the voltage increases to 0.5 V (Figure 4.8 b) more particles fill the lines, and very few land non-specifically; however, self-assembled lines still show a discontinuity. At 0.7 V and 1 V (Figure 4.8 c and d), nanoparticles fill the lines with four nanoparticles and five nanoparticles on average, respectively, and no particles between the lines.

Applied voltage plays a critical role in the way nanoparticles grow. This growth is also dependent on how far apart magnetized strips are located. While with 0.2 V applied voltage nanoparticles seem to self-assemble non-specifically at 500 nm spacing, at 50 nm spacing, they grow vertically and form long chains of particles. Figure 4.9 shows this behavior for the same disk drive medium, nanoparticle concentration, and coating times. As seen in these images, chaining is associated with how much voltage

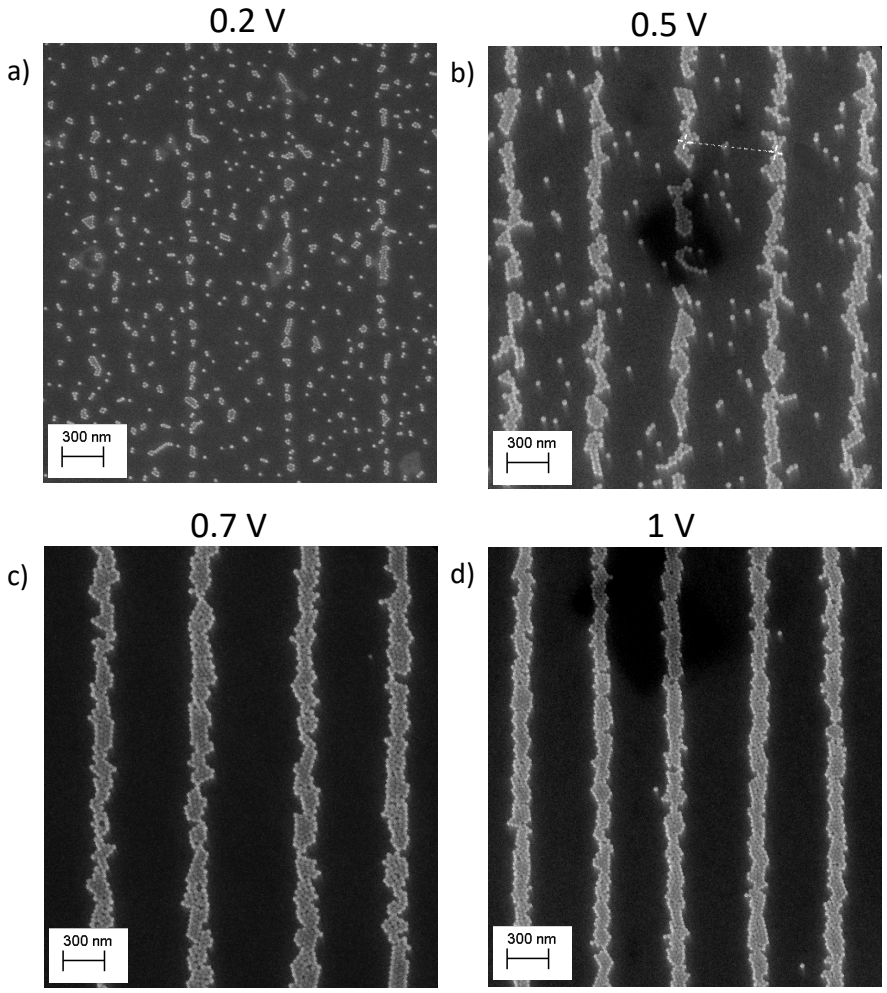

Figure 4.8 SEM images of nanoparticles self-assembled for 500 nm spacing with a) 0.2 V, b) 0.5 V, c) 0.7 V, and d) 1V applied

is applied to the write head. At 0.2 V applied voltage (Figure 4.9 a - and inset b), the chain length of nanoparticle assemblies is shorter than when 1 V is applied (Figure 4.9 c - and inset d).

We employ image analysis using the image processing program ImageJ to calculate the width and length growth of nanoparticles as a function of voltage for both cases with 500 and 50 nm spacing. Figure 4.10 shows nanoparticle width growth at 500 nm spacing for four different voltage values (top) and length growth on nanoparticles at 50 nm spacing for 0.2 V and 1 V (bottom). Width growth seems to be linearly

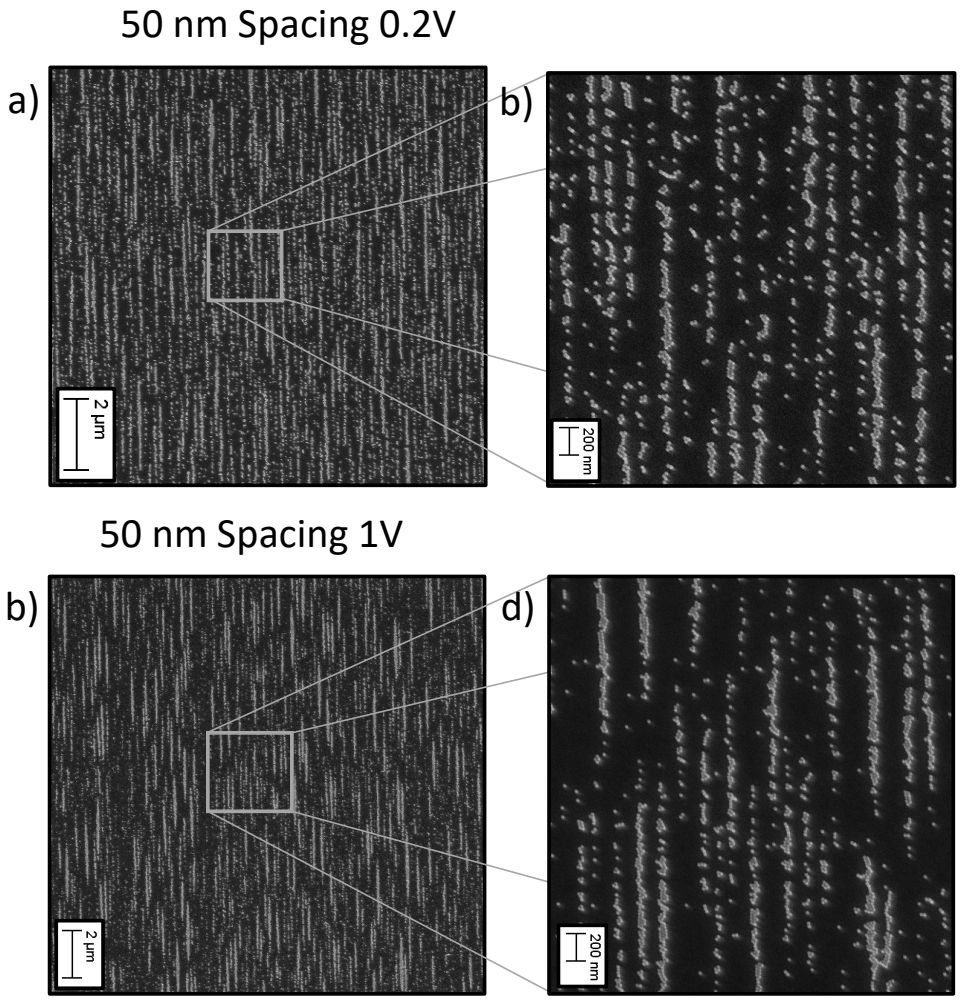

Figure 4.9 SEM images of nanoparticles self-assembled at 50 nm spacing for: a) 0.2 V and c) 1 V. Insets b and d show the zoomed in image for both cases

increasing as applied voltage to the write head is increased. Higher applied voltage leads to a more intense fringing field produced by the write head, and more area is magnetized. An extended magnetized region has stronger field gradients, and consequently, the region fills more magnetic nanoparticles.

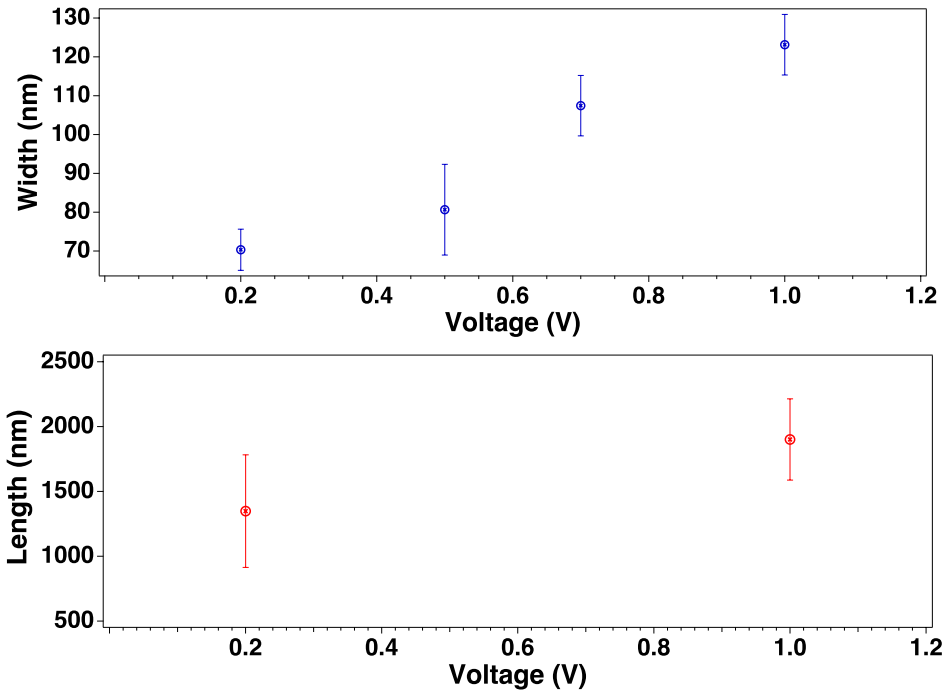

Figure 4.10 Calculated a) width and b) length, of nanoparticles as a function of voltage

4.1.2 Effects of media lubrication on self-assembly

Lubricants have been widely used for numerous special tribological applications because of their superb oxidative and thermal stability properties in magnetic recording disks, mostly for topical lubrication to reduce the wear of rigid disks. Commonly used lubricants include Fomblin Z and Demnum, as well as their polar derivatives containing various reactive end groups, e.g., hydroxyl (Fomblin Z-DOL, Demnum SA), and piperonyl. [47] [9]

When we initially record patterns on the disk drive medium, we apply 0.01 % Zdol-Vertrel solution—increasing the percentage of Zdol from 0.01% to 0.1% increases the lubrication layer that significantly changes the assembly of nanoparticles.

As seen in Figure 4.11, for a 1000 nm line spacing, nanoparticles form distinct two-

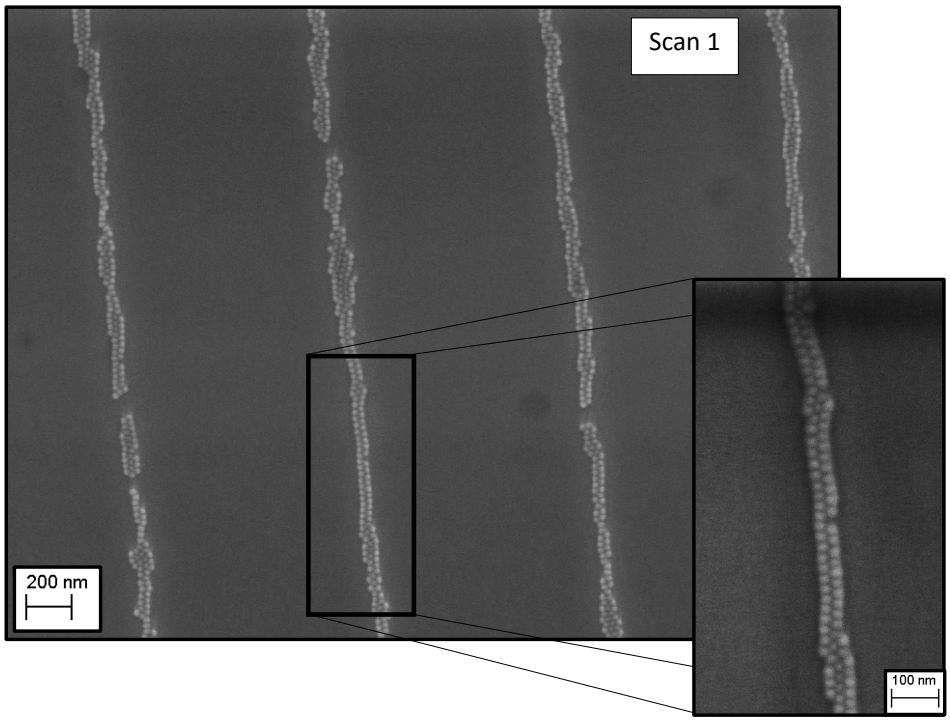

Figure 4.11 SEM images of nanoparticles self-assembly at the surface of the media with 1000 nm spacing but with higher concentration of Zdol lubricant

particle assemblies with some discontinuity. The increased percentage of lubricant creates a layer that repels nanoparticles, and only in the region with maximum force field does nanoparticle self-assembly happens. The lubricant layer burns out when the coated medium is exposed to the SEM beam. Upon coating media for the second time, the lubricant-free region (that was burnt on the first SEM scan) self-assembles nanoparticles into broader features and double-layers which is demonstrated in Figure 4.12.

4.2 Space dependence in pure hexane and ethanol solution

Figure 4.13 shows the SEM images of self-assembly with added ethanol for a) 300 nm, b) 500 nm, c) 1000 nm, and d) 1500 nm spacings. The features in this figure show

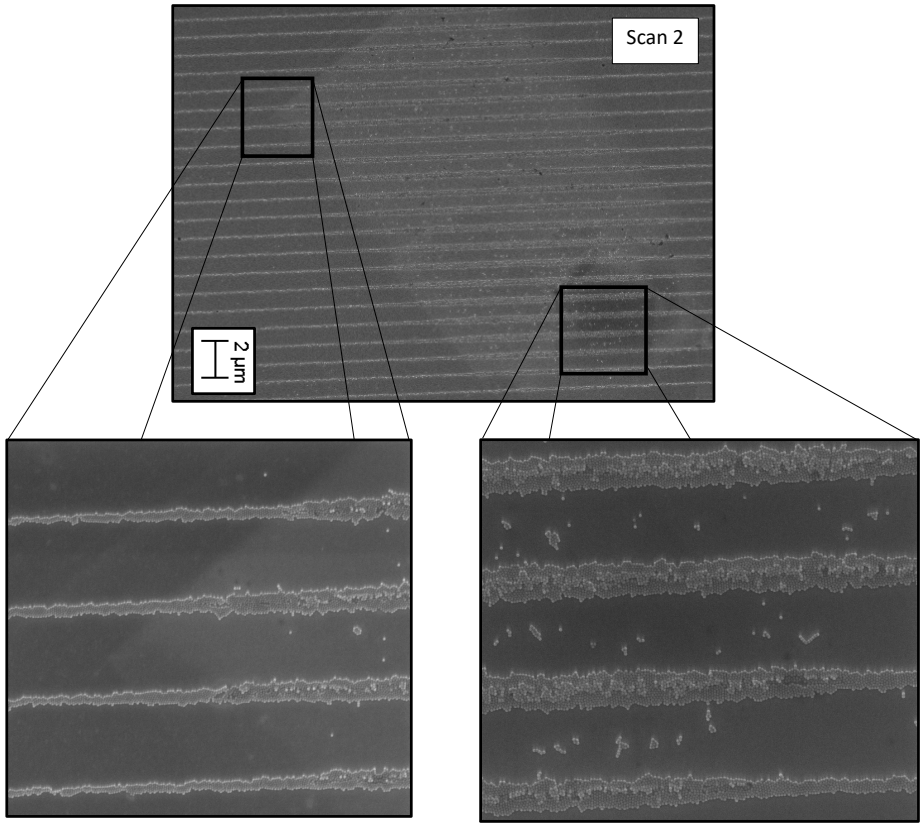

Figure 4.12 Second scan images of nanoparticles self-assembly with higher concentration of Zdol lubricant after initial exposure to the SEM beam, lower images show the regions that were exposed to the beam have increased nanoparticles assembly

that the nanoparticles are no longer hexagonally close-packed. More importantly, they no longer form a single stripe, but rather a gap opens at the center of the stripe, with the increased number of non-specifically assembled particles between the lines.

To compare self-assembly when ethanol is added to the solution, we quantify parameters such as features width, edge roughness, and a number of non-specific assembled particles between lines with ImageJ software. Details of these calculation can be found in Appendix C.1.

Figure 4.14 a, b, and c show line width, edge roughness, and the number of non-specifically particles as a function of line spacing for the solution with (blue curves)

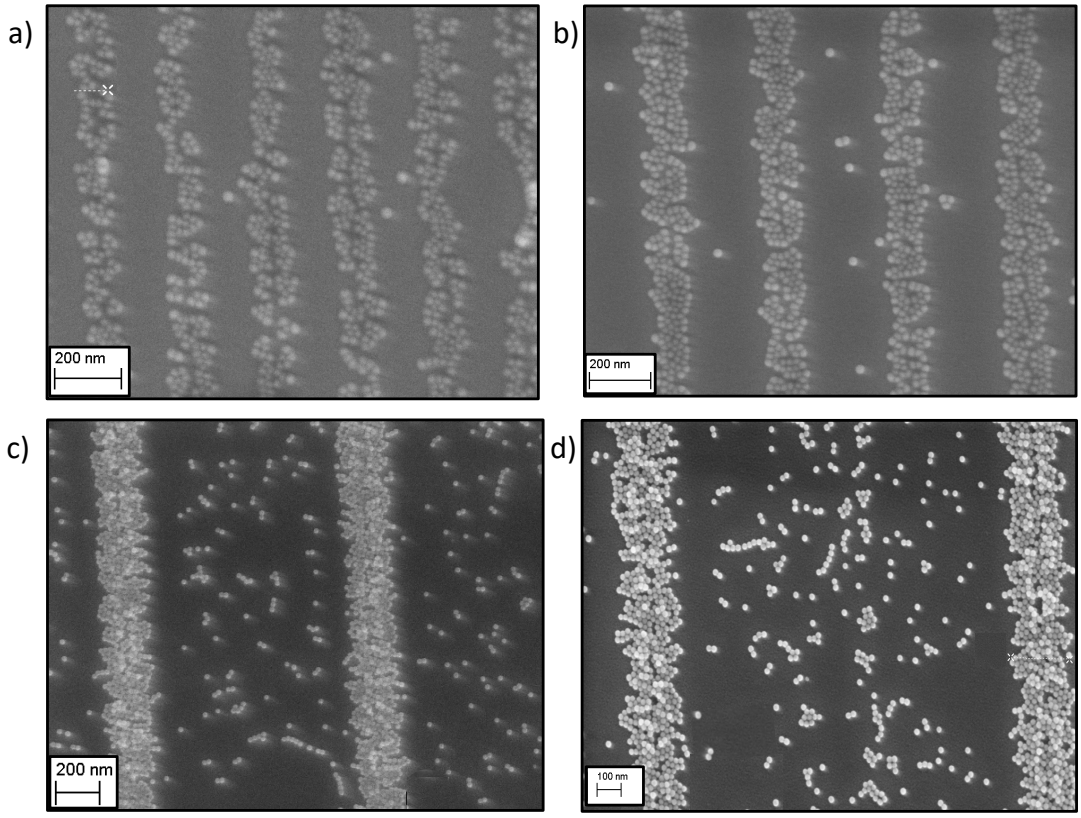

Figure 4.13 SEM images of nanoparticles self-assembly in hexane with added ethanol at: (a) 300 nm, (b) 400 nm, (c) 1200 nm, and (d) 1600 nm spacings

and without (red curves) ethanol. For the case with no ethanol, 200-300 nm spacing yields features 1-3 particles wide, while spacing 500 nm or larger yields features greater than five nanoparticles wide. Edge roughness is minimum for line spacing 200 nm to 600 nm with values of 25 to 50 nm and is at maximum for spacing 800 nm and beyond with values of nearly 125 nm. For the case when ethanol is added to colloid, at 200 nm spacing, features are 3-4 nanoparticles wide and at 500 nm spacing, features yield six nanoparticles. Edge roughness increases for all spacings when ethanol is added, varying from 60 to 90 at 200 nm spacing to nearly 175nm for spacing 800nm and beyond. The number of non-specifically-assembled particles between lines for the hexane solution on average is $1 - 6$ nanoparticles for $200 - 500$nm

spacings and slowly increases to 15 nanoparticles at 1000nm. For the hexane solution with ethanol, the number is similar at 200 – 500 nm spacing. However, it increases to 65 nanoparticles at 1000 nm spacing. One possible reason for this increased number could be the aggregation of the particles due to the modified surfaces of the particles and absence of strong fields between the stripes.

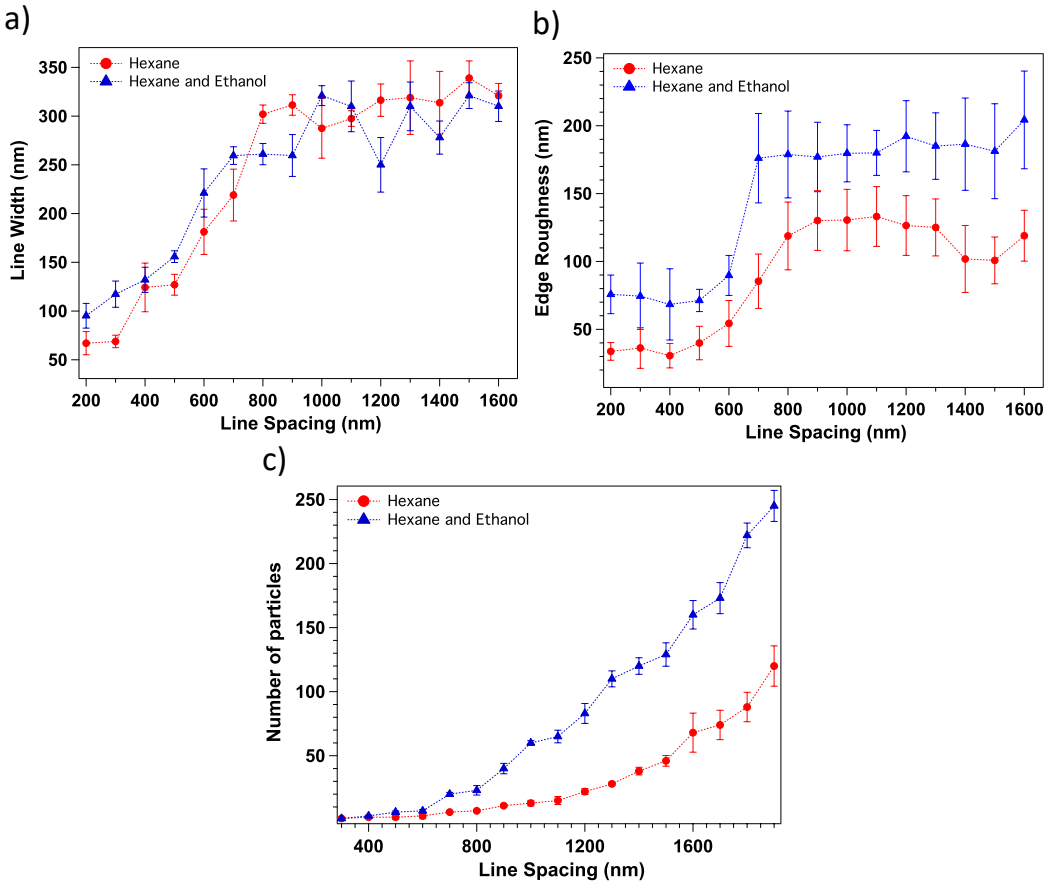

Figure 4.14 a) Line width, b) Line edge roughness, and c) number of non-specifically assemble particles for nanoparticles in hexane (red curves) and hexane plus ethanol (blue curves) as a function of line spacing

Chapter 5

Order in Magnetic Nanoparticles Arrays

One of the characteristics of monodisperse nanoparticles is the ability to form an ordered, close-packed structure. Polydispersity and defects such as dislocations or vacancies between particles within lines preclude the long-range order in 2D systems, thus leading to a hexatic-like phase of self-assembly. In the previous chapter, we demonstrated that magnetic patterns of the disk drive medium drive self-assembly into ordered nanoparticle arrays, specifically at 400 - 700 nm spacings. This chapter discusses and quantitatively measures order in these quasi-crystalline nanoparticle self-assemblies.

5.1 Introduction

In colloidal systems, the system's dimensionality is essential in describing the physical properties of self-assembled structures. A notable example is when a system undergoes melting or crystallization. Such phase transition occurs in different situations ranging from ice formation in clouds and the preparation of rapidly quenched metallic alloys to the production of window glass. [64]

During the last centuries, vast technical experience in quite different areas has been earned where freezing and melting phenomena are used to facilitate everyday life. Despite this rapidly increasing experimental and phenomenological knowledge, molecular aspects were addressed only in the last decades, aiming at a microscopic understanding of the solid-liquid phase transformation.

5.2 Statistical Mechanics of Two dimensional systems of particles

It has been known that when solid melts through heating, microscopical lattice waves are generated, which are known as phonons. When the amplitude of vibration exceeds a certain fraction of lattice constant (i.e., Lindemann Criterion), solid is no longer stable, and the state of matter changes to liquid. When the temperature is increased, lattice excitation is not the only thing that can happen; the other thing that might happen are topological defects.

Examples of topological defects happen a lot in nature, such as vortices of superfluid, dislocations in a solid, skyrmions, etc. If such topological defects can be generated thermally, can they give order to disordered transition? This problem has been addressed by John M. Kosterlitz and David J. Thouless. [54] They have shown that such transition can happen in the two-dimensional (X, Y) spins model through the neighboring interactions. The topological defects in such a system are vortices, where the sum of the twist in the angle around the edges is $\pm 2\pi$, and no vortex or 0 when there is no twist. The energy required to create such vortices is

$$E_v = (\frac{J_s}{2}\pi \ln N) \tag{5.1}$$

with N total number of spins in the system and J_s interaction strength. Such vortices can be nucleated anywhere in the N sites, and the entropy of the system goes as $S = k_B \ln N$ with the free energy of:

$$F = E - TS \approx (2J - k_B T) \ln N \tag{5.2}$$

At low temperatures, the prefactor $(2J - k_B T)$ is positive, and creating a vortex is energetically unfavorable, leading to a ferromagnetic state. When the temperature crosses $\frac{2J}{k_B}$, the prefactor $(2J - k_B T)$ becomes negative; the free energy reduces and creates an energetically favorable vortex. As a result, it leads to dislocations' sudden

proliferation and magnetization drop to zero. Although it appears from such variation that it is a first-order transition, the free energy appears smooth and doesn't have a discontinuity. Such transitions are knows as Berezinsky, Kosterlitz, Thouless transition.

Halperin, Nelson, and Young predicted that melting could proceed through an alternate route [68] via two continuous phase transitions mediated via topological defects. The first transition involves the proliferation of thermally excited free dislocation in the lattice and creating an intermediate state between a crystalline and liquid. Then the second transition dislocations separate into isolated disinclination, thus producing an isotropic fluid. The intermediate state is called 'hexatic'. Such a state has zero shear modulus and short-range positional order, like that of a liquid, and quasi-long-range orientational order like a crystal. Much effort has been put into testing the BKTHNY theory in two-dimensional systems. Such as electrons over a liquid helium surface, Wigner solids, vortices in superconducting thin films, magnetic skyrmion lattices, and colloidal nanoparticle systems.

According to Nelson, the defects in such systems are usually dislocations and disclinations. These are characterized by a Burgers vector $a_0\vec{b}$, defined as the amount by which a contour integral of the displacement field around the dislocation fails to close. Therefore,

$$\oint d\vec{u} = a_0\vec{b}(r) \tag{5.3}$$

where a_0 is the lattice spacing, a dislocation occurs; for example, when a row of particles from a perfect lattice is removed. Topological defects and Burger's vector loop around them are shown in Figure 5.1. Figure 5.1 a shows self-assembled magnetic nanoparticles on a line where adjacent lines are 1000 nm apart. The defects due to disclination are marked with circles. Disclinantions can have a profound influence on breaking orientational order. Figure 5.1 b shows self-assembly of the same particles

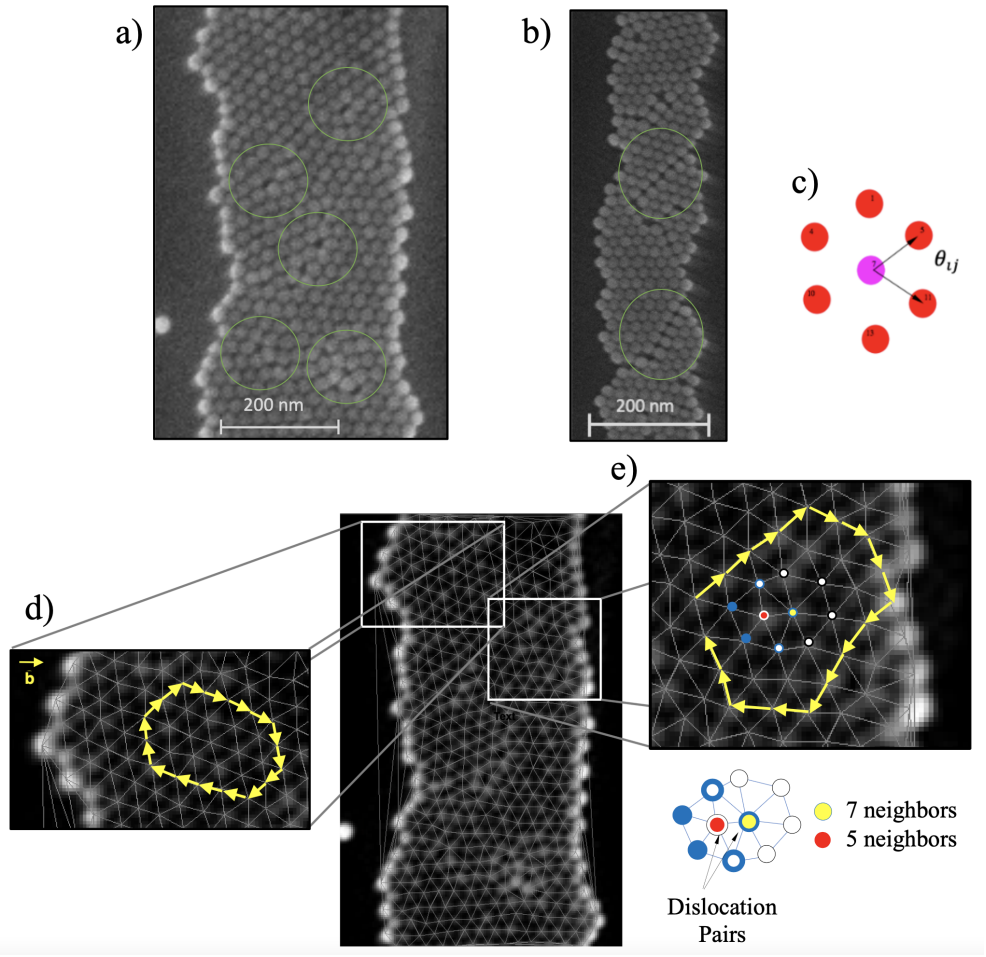

Figure 5.1 Topological defects of triangular lattice in nanoparticles arrays in a) 1000 nm spacing, b) 400 nm. Burger's vector in a region: d) with no defects forming a closed loop, and e) with defects where the particles can have 5 and 7 neighbors.

with narrower width at 400 nm spacing; note the dislocations can split nanoparticles (marked with circles) and can be pretty effective at breaking up translational order. Disclinations in Figure 5.1 a can be tested with Burger's vector method (Figure 5.1 d and e). The original image has an adjusted contrast and window level to find the center points better and generate a Delauney triangulation mesh. In the region where there are no defects, vector $\vec{a}$ forms a closed loop; however, in the areas where two isolated points of 5- and 7-fold symmetry are embedded, the loop around the

dislocation fails to close.

All three thermodynamic phases (solid, liquid, and hexatic) and their corresponding symmetries can be visualized using the structure factor:

$$S(\vec{q}) = \frac{1}{N} < \sum_{ij} e^{i\vec{q}(\vec{r}_i - \vec{r}_j)} > \tag{5.4}$$

The isotropic phase is characterized by concentric rings at $q = \frac{2\pi}{a}$, with $a = \frac{1}{2\pi}$, the average particle distance calculated by the two dimensional particle density ρ. The structure factor of Figure 5.2 is calculated from the positions of a colloidal monolayer (crosses at high intensity are artifacts from the Fourier transformation due to the finite field of view of the ensemble). [49] [53]

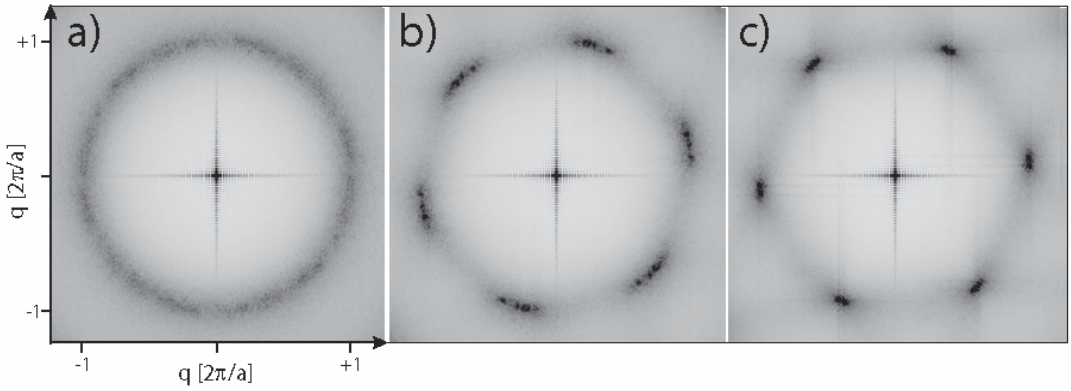

Figure 5.2 Structure factor of a) an isotropic fluid, b) the hexatic phase, c) a crystal in two dimensions. (With permission from [49])

5.2.1 Order in nanoparticles

Different correlation functions provide the quantitative measure of order in nanoparticle assemblies. Translational and rotational symmetries characterize crystalline solids. These two are not entirely independent: Rotating one patch of the perfect crystal relative to another disrupts translational order. However, translating one patch of

the crystal relative to another keeps the orientational order intact. The translational order parameter is given by:

$$\rho_G(r) = e^{i\vec{G}\cdot\vec{r}} \tag{5.5}$$

where $\vec{G}$ is a reciprocal lattice vector and $\vec{r}$ is the position of a particle. To examine translational order, the Radial Distribution Function (RDF) G(r) is often calculated. The radial distribution function is the probability distribution to find the center of a particle in a given position at a radius r from the center of a reference sphere. [37] This measurement is widely used to characterize packing structures and contains information about long-range interparticle correlations and their organization. [78]

Bond-orientational correlation function in two dimensions $G_6(D)$ can be defined as

$$G_6(D) = \langle {\psi^*}_6(0)\psi_6(D)\rangle \tag{5.6}$$

with ψ_6 a complex local orientation order parameter at site i:

$$\psi_6(D) = \frac{1}{N}\sum_j e^{6i\theta_{ij}}, \tag{5.7}$$

where the sum over j is the sum over all the nearest neighbor particles to site i and θ_{ij} is the angle made by the line joining the center of i to the center of j, relative to a reference axis (Figure 5.1 c). Once ψ_6 is calculated for all particles i, one can then calculate the orientational correlation ${\psi^*}_6(0)\psi_6(D)$ between a particle pair which is located at a distance D apart. All particle pairs are thus calculated, allowing sufficient statistics to determine the mean value of the correlation $G_6(D) = \langle {\psi^*}_6(0)\psi_6(D)\rangle$.

In a perfect crystal $G_6(D)$ is equal to 1 and independent of the distance D. [12] For imperfect crystals, the decay of $G_6(D)$ as a function of distance provides information about the degree of orientational order. For example, a hexatic phase is an intermediate between the liquid and solid phase, typically found in liquid crystals

and colloidal systems.[13],[25] In the hexatic phase $G_6(D) \sim D^{-\eta}$ where $0 < \eta < 1/4$.[36],[27]

5.3 Translational and Bond orientational correlation calculation

We use image analysis to quantify order in nanoparticle assembly. The center points for each particle are needed in both translational and orientational analysis described in the previous section. These points are taken from SEM images using the Image Science library's Fiji (ImageJ) software. For each stripe, a rapid change in intensity of the features was detected using the FeatureJ function followed by Gaussian blur. Home-built Mathematica code (see Appendix C.2) was then used to calculate the bond orientation correlation parameter $G_6(D)$ for multiple stripes for a given spacing from experimental data for the case with hexane solution and the case where ethanol is mixed with the solution.

To test the radial distribution function and Fourier transform of the patterns, we use a similar approach to [51] with ImageJ (Figure 5.3). The resulting fast Fourier transform pattern that is shown in Figure 5.3 b shows sharp peaks, indicating the nature of high order and crystalline assembly. Similarly, defects due to dislocations and disinclination in our sample for 400 nm spacing are shown in Figure 5.4. Here, the lack of translational order, quasi-long-range orientational order, and the Fast Fourier Transform (FTT) diagram seem to show the hexatic phase assembly. The FFT pattern does not have sharp peaks like in the crystal case and does not have a spreading ring like in liquid. (Figure 5.4 b) . The radial distribution function for this sample shows a high correlation over 250 nm distance (90 pixels).

Furthermore, for the bond orientational correlation function, we computed $G_6(D)$ as a function of spacing for multiple images. Figure 5.5 shows the calculated correlation function for different spacing. Each plot represents an averaged $G_6(D)$ for multiples lines, and fit plot ($G_6(D) = \frac{1}{D^{\eta}}$). Calculated fit parameters η with corre-

sponding fits are shown in the inset for each plot. From these plots, the sample with 400 nm has the lowest η parameter, while the 1000 nm spacing has the highest η parameter. The corresponding η parameter for all spacings for both cases, with and without added ethanol, are shown in Figure 5.7.

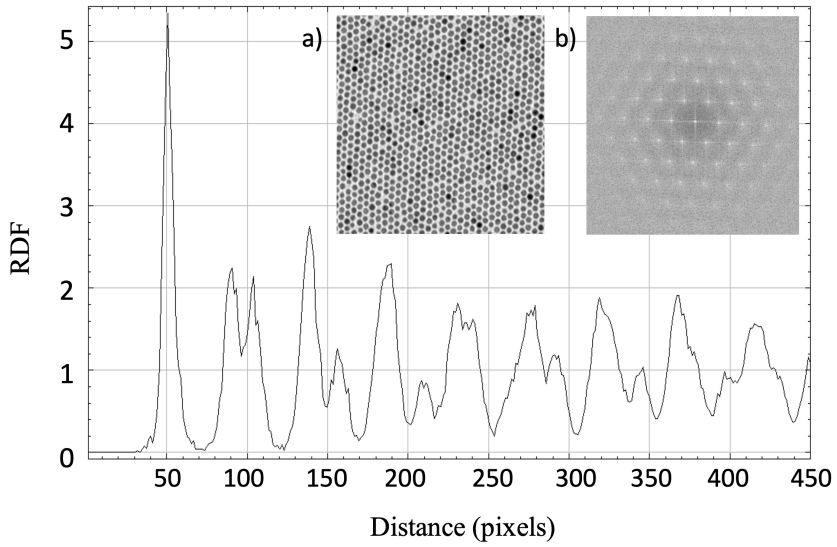

Figure 5.3 Example of calculated RDF from a nearly perfect crystalline assembly a) by Kimyujin et al, and b) its corresponding fast Fourier transform pattern. (With permission from [51])

Figure 5e shows calculated $G_6(D)$ as a function of distance within a nanoparticle feature for simulation (triangles) and experiment with hexane (circles) and with hexane and ethanol (squares). Spacing between stripes are $d = 400$ (red) and 1000 nm (black). We find that $\eta = 0.21$ for stripe spacing between 400-600 nm, suggesting these nanoparticles are in a hexatic phase. However, for 1000 nm spacings, η increases to 0.33, outside the typical hexatic phase range. For the simulation at 400 nm spacing, $G_6(D)$ maintains a large, nearly constant value compared to 1000 nm spacing, with minimal η values that are well within the hexatic limit. The reasons for the large discrepancy between the simulated and experimental $G_6(D)$ values are twofold is because: Firstly, the simulated dynamics lack poly-dispersion in the size of nanopar-

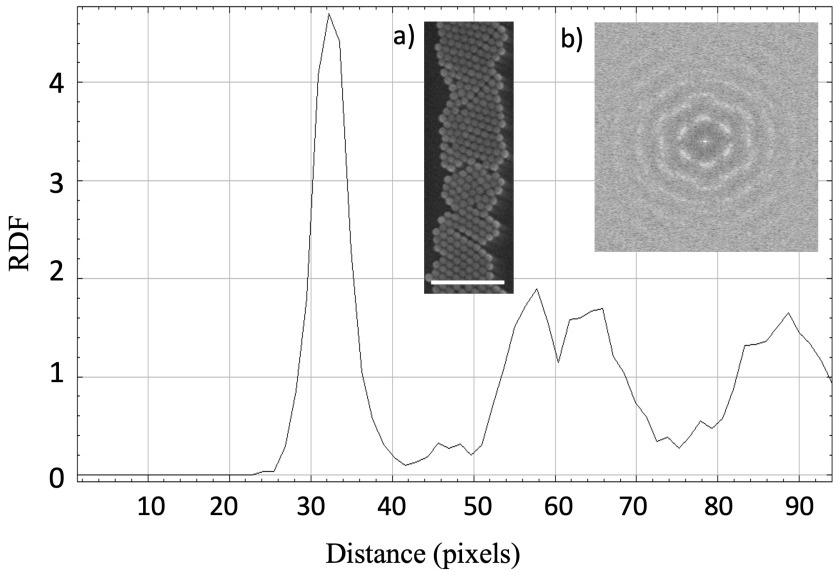

Figure 5.4 Calculated RDF plot from a) SEM image of nanoparticles self-assembly at a stripe with 400 nm spacing (scale bar 200 nm), b) corresponding fast Fourier transform pattern

ticles, allowing particles to pack together in a more ordered fashion, increasing the $G_6(D)$ value calculated. Secondly, the transitions in magnetization are modeled as perfectly parallel. In contrast, in reality, the medium grains have abnormal sizes and shapes, creating a meander in the lines of magnetic transitions. Even excluding these details from the simulation, the decay does follow the same trend found in the experimental $G_6(D)$ for stripe spacing; for the case of a 2 % ethanol solution, $\eta \sim 0.63$, much larger than hexatic phase limit. This quantitative result matches our earlier observation from the SEM image (Figure 3.6) that the addition of ethanol largely destroys hexatic order. The $G_6(D)$ analysis demonstrates that although the nanoparticle features are limited in their width, the quasi-crystalline assembly can be achieved within the stripes.

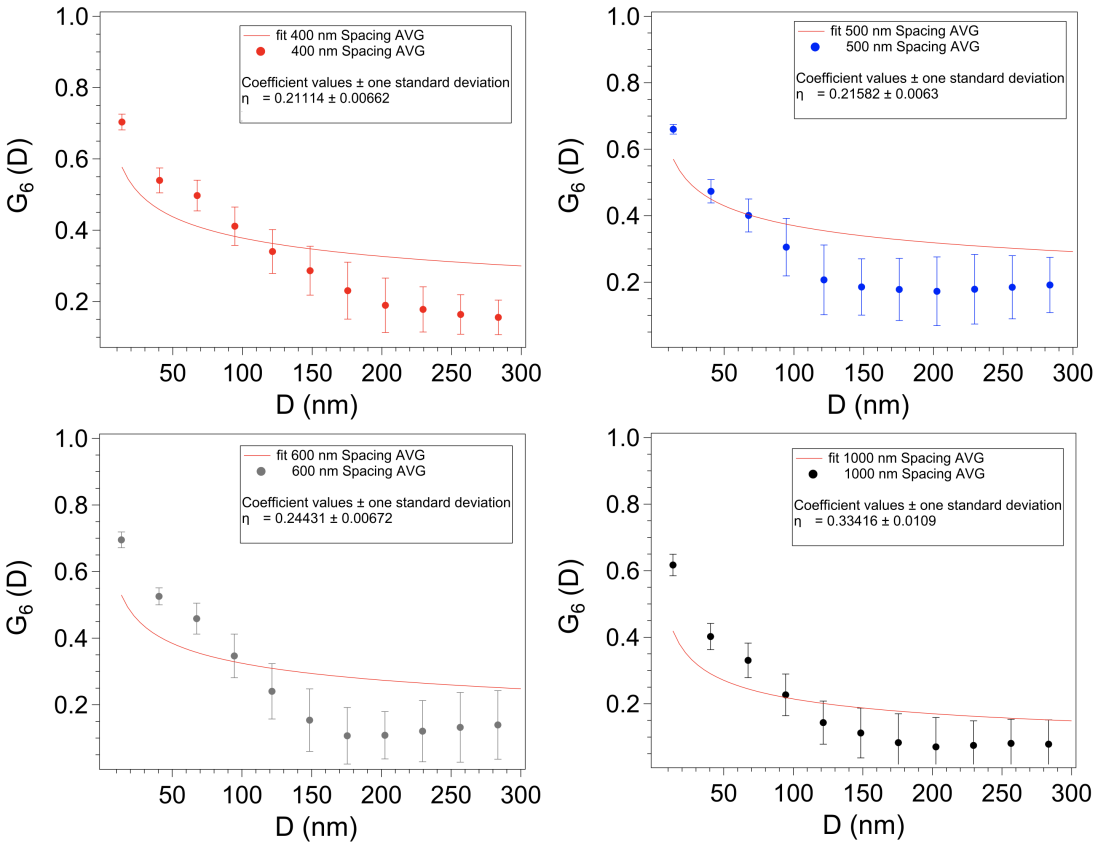

Figure 5.5 Calculated $G_6(D)$ for hexane case and corresponding fit plots for four spacings

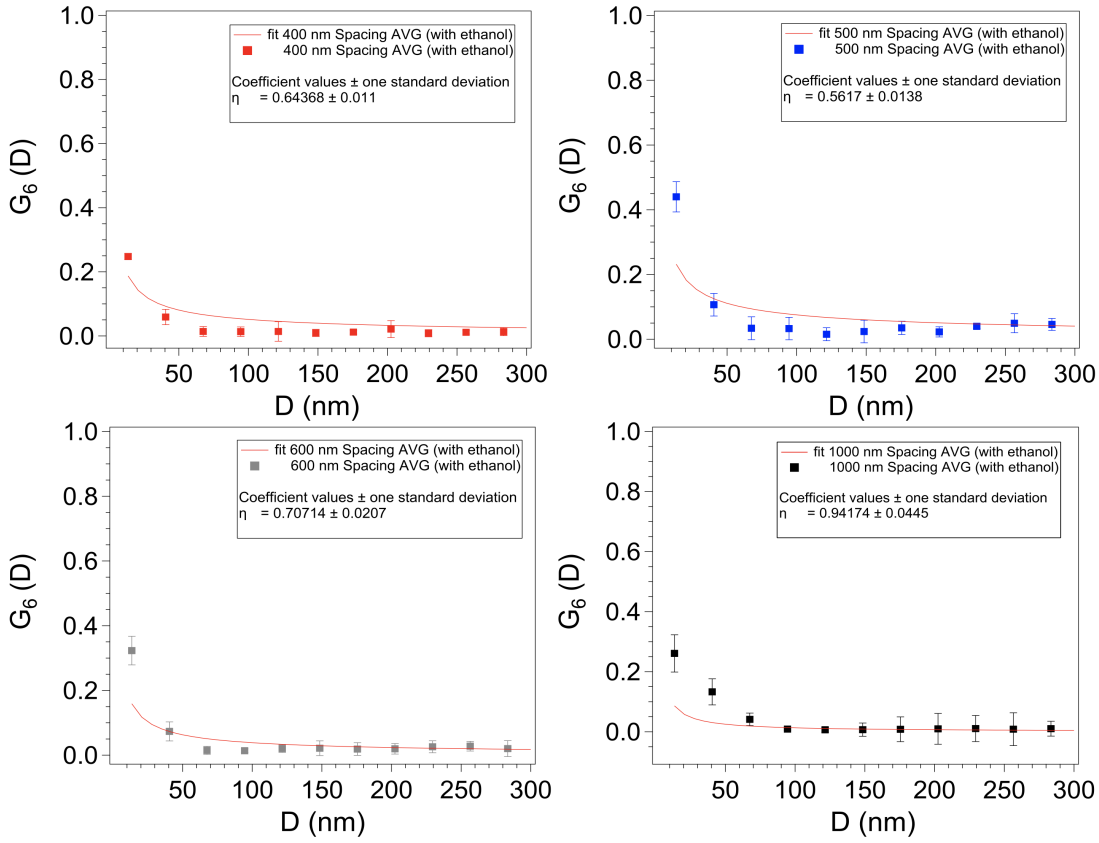

Figure 5.6 Calculated $G_6(D)$ for the case of added ethanol and corresponding fit plots for four spacings

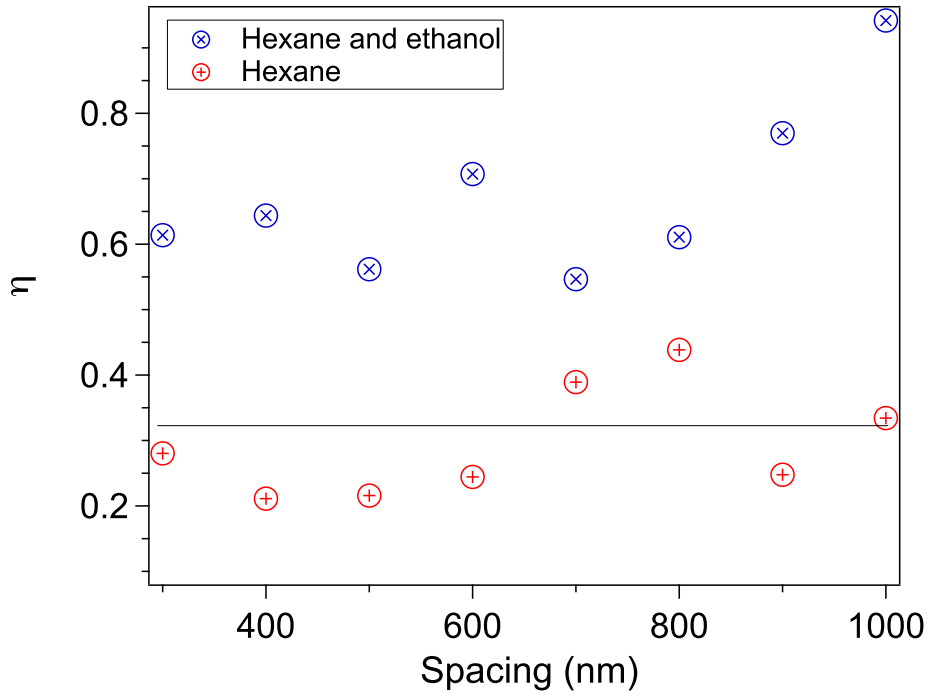

Figure 5.7 Calculated η parameter for different spacing for both cases with ethanol (blue marks) and no ethanol (red marks)

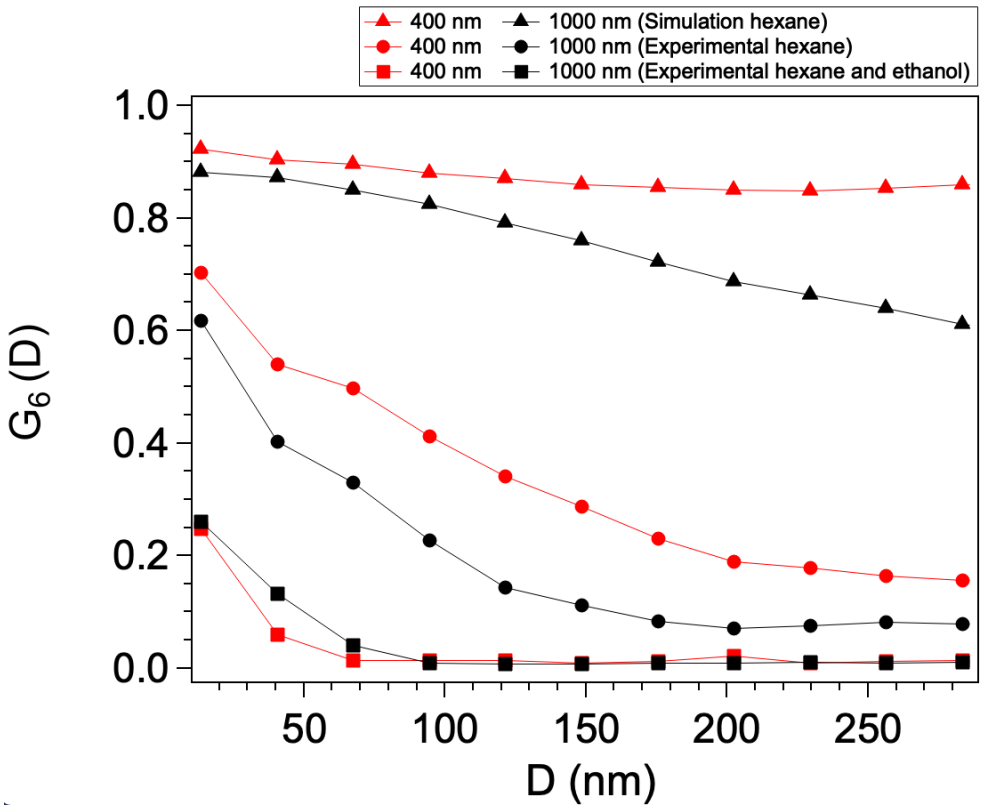

Figure 5.8 Comparison of calculation of G6(D) for simulation in hexane (triangles), experiment in hexane (circles) and experiment in hexane and ethanol (squares). For each of these three cases, line spacing d = 400 nm (red symbols) and 1000 nm (black symbols) are considered

Chapter 6

Magnetic read back process of the recorded templates

In this chapter, we focus on the underlying recorded templates to investigate the cause of the defects in self-assembled structures. In a hard disk drive, the head assembly contains both write and read head elements; here, we demonstrate the possibility of simultaneously writing and reading the recorded region. This way, one can test and confirm the recorded area without depositing nanoparticles. Furthermore, the read-back signal shows sensitivity and quality of recorded patterns.

6.1 Introduction

In the recording method that was mentioned in chapter two, the transitions are obtained by applying DC voltage (± 0.7 volts) to the write head coil while scanning the head across the disk drive medium. This method is mainly used to produce large regions of parallel magnetized lines, such as templates for a diffraction grating. Another method to record templates is called Bitmap Recording, which was developed by Adam Fischer (*et al.*) at MagAssemble (LLC). In this method, a bitmap image can be loaded to LabView software and converted to an array of on and off signals that dictate both Arbitrary Waveform Generator (AWG) to the output voltage to the write head and the (X, Y) stage to move accordingly. The software compares the bitmap image dimension to the stage motion via pixel coupling; each pixel in the bitmap image (either black or white) becomes a particular current and is converted

to the nanometer distance that allows the write head to move accordingly. Some examples of the medium recorded using bitmap images can be found in Appendix B.8.

6.2 Giant Magneto-Resistance and read back of single sharp transition

Bound currents create the field inside a magnetized medium [89]. The magnetic medium extends horizontally in the (x, y) plane, and for a single-step transition below, the following relation for M as a function of position holds

$$M(x) = \begin{cases} -M_r \quad for \quad x < 0 \\ \\ M_r \quad for \quad x > 0 \end{cases} \tag{6.1}$$

Typically, the information is read by a process called "*Giant Magneto Resistance*". GMR head is typically consists multiple layers with different magnetic materials and a nonmagnetic layer known as *Spacer*. These layers have two configurations to sense the magnetic field produced by the transitions (0's and 1's), and control the resistance of the entire read head is controlled by "*Spin-valve*" which consists of four laminated metal layers: an anti-ferromagnet pinning layer, a pinned layer whose magnetization is fixed by an exchange-coupling field from the anti-ferromagnet layer, a Cu interlayer, and a free layer whose magnetization rotates according to the signal field from the disk media [48]. Heads in modern high aerial density disk drives read the information with Tunneling Magnetoresistance (TMR). TMR head is similar to GMR but with higher magnetoresistance and has an additional separating layer that acts as an obstacle for electrons to pass. The conduction happens when electrons tunnel through this insulating layer. [1]

6.2.1 Read-back process

We have significantly improved the head assembly extracting the process from a disk drive to protect the reader from Electrostatic Discharge (ESD). The removal process, ESD protection circuit, and grounding tools are mentioned in Appendix B.

Once the disk drive medium is magnetized and desired templates are achieved, the read head can be employed to map the magnetized pattern. This step is essential as it tells how well the transitions are recorded. The read head element is a rectangular shape that is narrow in one direction, and scanning resolution is more sensitive in the down track (i.e., scanning in the y-direction in Figure 3.1 b). If a template is recorded with lines, such as diffraction grating where lines are parallel in the y-direction, then to read-back a recorded line, one must re-orient the disk drive medium to be perpendicular to the read head scanning. However, locating the pattern with the reader is challenging, especially for smaller patterns. To overcome this, either the recording template must have multiple reference points for easier detection or to record the template with the arbitrary bitmap method (with an image where the lines are parallel to the x-direction). Thus, there is no need to re-orient the medium perpendicular to the read element. Recording large line templates in cross-track, i.e., moving the head in the x-direction, is not often recommended and may require further suspension stiffening and lubrication.

First, for the parallel line or diffraction grating pattern recording, we test the read head by writing a large $2 \times 2mm^2$ with 830 nm spacing. Upon completion of writing, the coupon is rotated 90 degrees. The read head outputs the change in the resistance as the head scans the media and passes transitions of oppositely magnetized regions. Figure 6.1a shows four line scans of a segment of a $2 \times 2mm^2$ region. Here the number of steps in the down-track scan is 4 nm, while the resolution in Cross track is 15 nm.

Figure 6.2 b shows corresponding resistance profiles for each scan, where resistance averages to 6.3 ohms for each peak. Such profiles can give information on the write

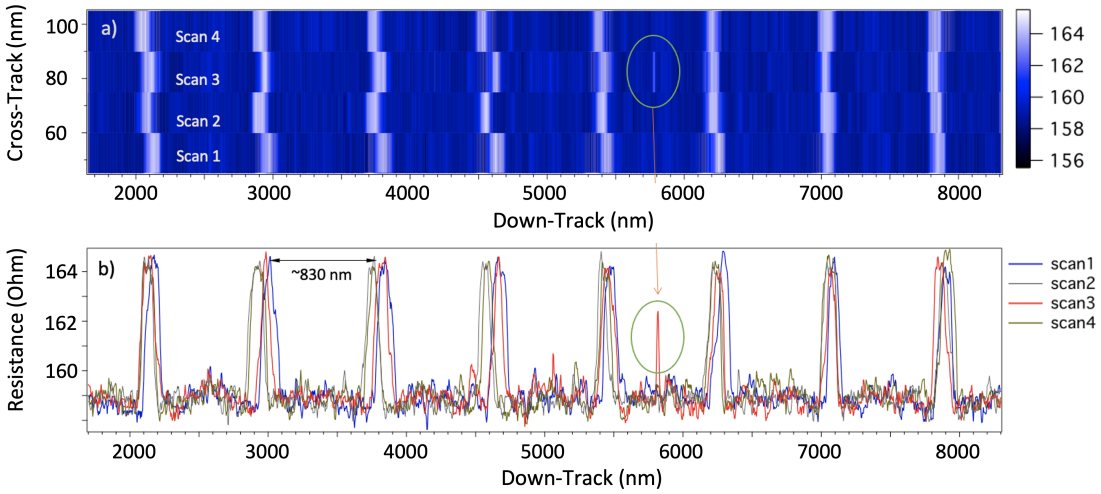

Figure 6.1 a) Readback 2D image of four line scans, and b) corresponding resistance profiles, for parallel recorded lines with 830 nm spacing

width and separation between two transitions. For this, we use IgorPro software signal analysis function to get the Gaussian fit profile for each line scan and get (Figure 6.3). Then we calculate the full-width half-max (FWHM) for each peak for multiple line scans (Figure 6.4). The FWHM data is averaged for 35 peaks for a single scan, which averages to 102.5 nm $\pm$ 12.10 nm.

The low voltage output could be due to the lift-off of the head after recording. That is why testing the reader is preferred when the template is recorded using an arbitrary bitmap image. The reader is not lifted after the recording, and the distance between the head and the medium is fixed. Figure 6.4 demonstrates a recorded arbitrary bitmap image (in this case, the logo of the University of South Carolina), its corresponding read-back image that is recorded with 15 nm pixel coupling, and the read-back signal of the individual line scans within the recorded regions. Figure 6.5 shows the resulting assembled nanoparticles with a 15 nm diameter on the same recorded areas with four different pixel couplings (15, 20, 30, 60 nm). The recording with 60 nm pixel coupling shows clear self-assembly, while the recording with 15 nm does not clearly show the logo. While this bitmap image was used to demonstrate

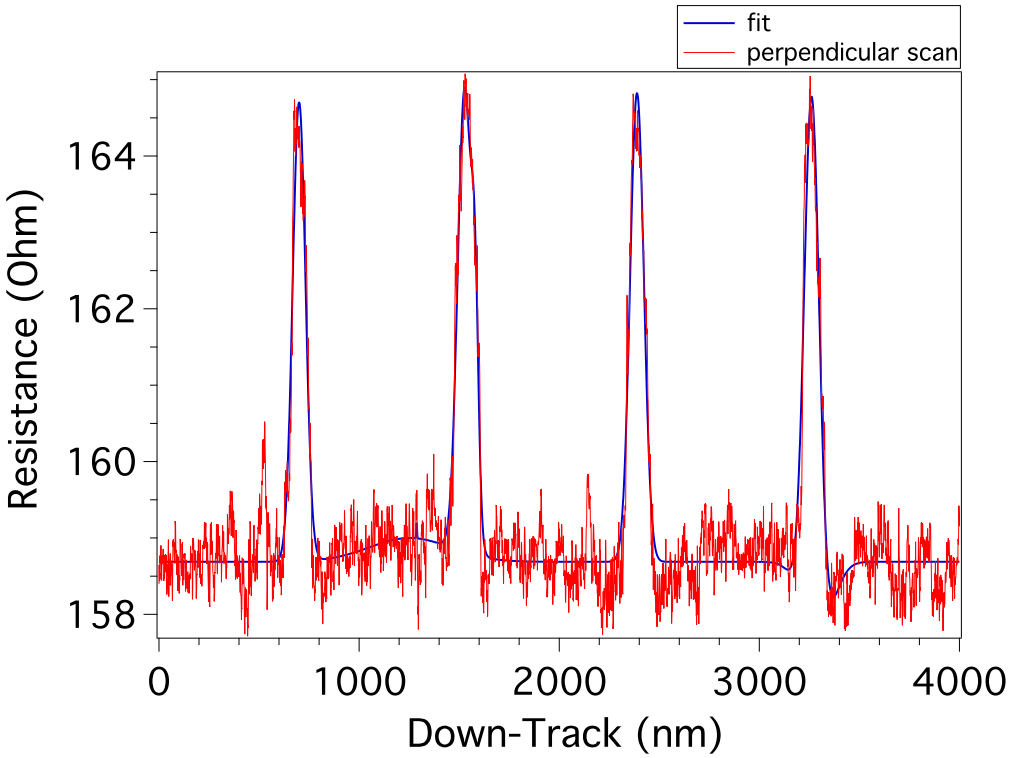

Figure 6.2 Applied fit to the resistance profile for a single line scan

the ability to record and read a well-known pattern with detailed features, it is not ideal to quantitatively measure the sharpness and quality of the recording.

To better test the sharpness of transition with the read-back, we prepare a more detailed bitmap image to record (Figure 6.6). The image is $1500 \times 1500 pixels^2$ with squares and lines. At the top left corner of the image, the square with a line across its diagonal is a reference to locate the pattern quickly. There is also 3 set of lines, each with different pixel spacing. We record three different pixel coupling values for this image: 15, 45, and 60 nm. The same head that the patterns were written is used for read-back.

Figure 6.7 shows the 2D image plot for the top left region of the original bitmap. As seen in the figure, head scans in both down-track and cross-track. Profiles are plotted to confirm and compare the output resistance for each scan in the down-track

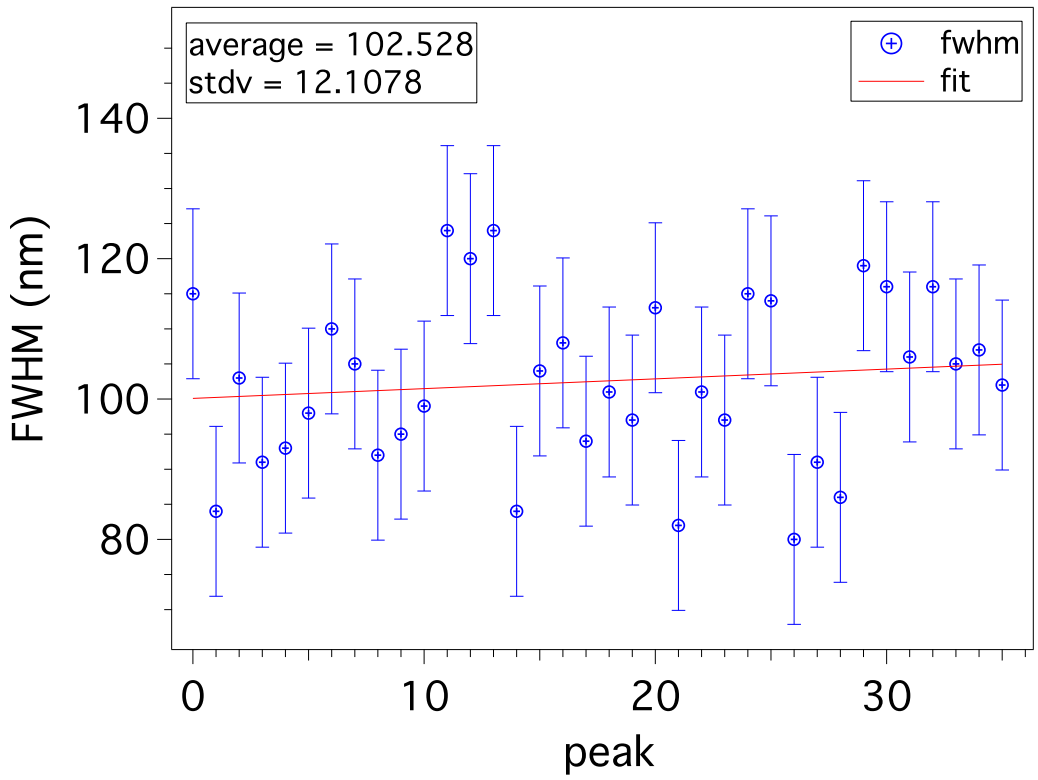

Figure 6.3 Averaged full width half max for 35 peaks of resistance profiles

line. Three line sets in the bitmap image show the resistance output by the read head. The lines with 5 pixels spacing seem to have higher resistance output according to the heat map scale, the 1- and 2- pixels spacing has less resistance. Note that the line profiles for the square that contains 2-pixel line spacing are similar to the case of line recording (Figure 6.1). This is because lines are located between two squares (to the left, a square with a line in diagonal, and to the right, a thick square). The sudden sharp jumps in resistance (nearly 50 ohms) represent the space between the lines and the squares (i.e., the spacing is a sharp transition itself).

Figure 6.8 shows averaged line profiles for each set. For a line set with 5 pixels spacing, the average resistance is 16.3 ohms; for 2 pixels spacing, resistance averages 8 ohms; for lines with 1-pixel spacing, it averages 10.2 ohms. Although the lines

are distorted in two-dimensional images, the averaged line scans show the sensitivity of the read head for each spacing. The recorded bitmap pattern with 60 nm pixel coupling is coated with magnetic nanoparticles and observed with SEM to confirm the self-assembly. We use iron oxide nanoparticles of 15 nm diameter and coat the recording media for 20 minutes. The nanoparticle preparation and media coating follow the same recipe used in previous chapters.

Figure 6.9 shows the Scanning Electron Microscope (SEM) image of the disk drive medium coated with 15 nm diameter iron oxide nanoparticles in hexane for 20 minutes. As seen in this image, the patterns' edges are sharp, confirming that the distortion in the read-back map is not due to the recording. We confirm the pixel coupling by calculating the spacing between the lines in the rectangle with 5 pixels spacing (corresponding to 300 nm in SEM images). Figure 6.9 b shows zoomed-in images of the line set with 5 pixels spacing, and Figure 6.9 c shows averaged line profiles of image inset b. The full-width half-max of the spacing shows the average spacing of 295 nm with ± 11 nm standard deviation, which is close to $5px \times \frac{60nm}{1px} = 300nm$. From Figure 6.9 c, one can see the double peaks on the line profiles that are also visible in the SEM image on each line. This is due to the size of the nanoparticles. With smaller nanoparticles, the lateral x-directed magnetic force pushes the nanoparticles on the two sides of the transition. As a result, nanoparticles do not fill the regions between transitions. This confirms the sensitivity of MFDSA to the change in diameter of particles that was mentioned in Chapter 3. Figure 6.10 shows all three regions with three different line spacing, 5- pixels and 1- pixel (top), and 2- pixels (bottom).

From the read-back map, the defects in the two-dimensional image may not necessarily be due to the writing. Further experiments can be done to improve the quality of the read-back by adjusting the time constant of the signal in the lock-in or controlling the read-back speed.

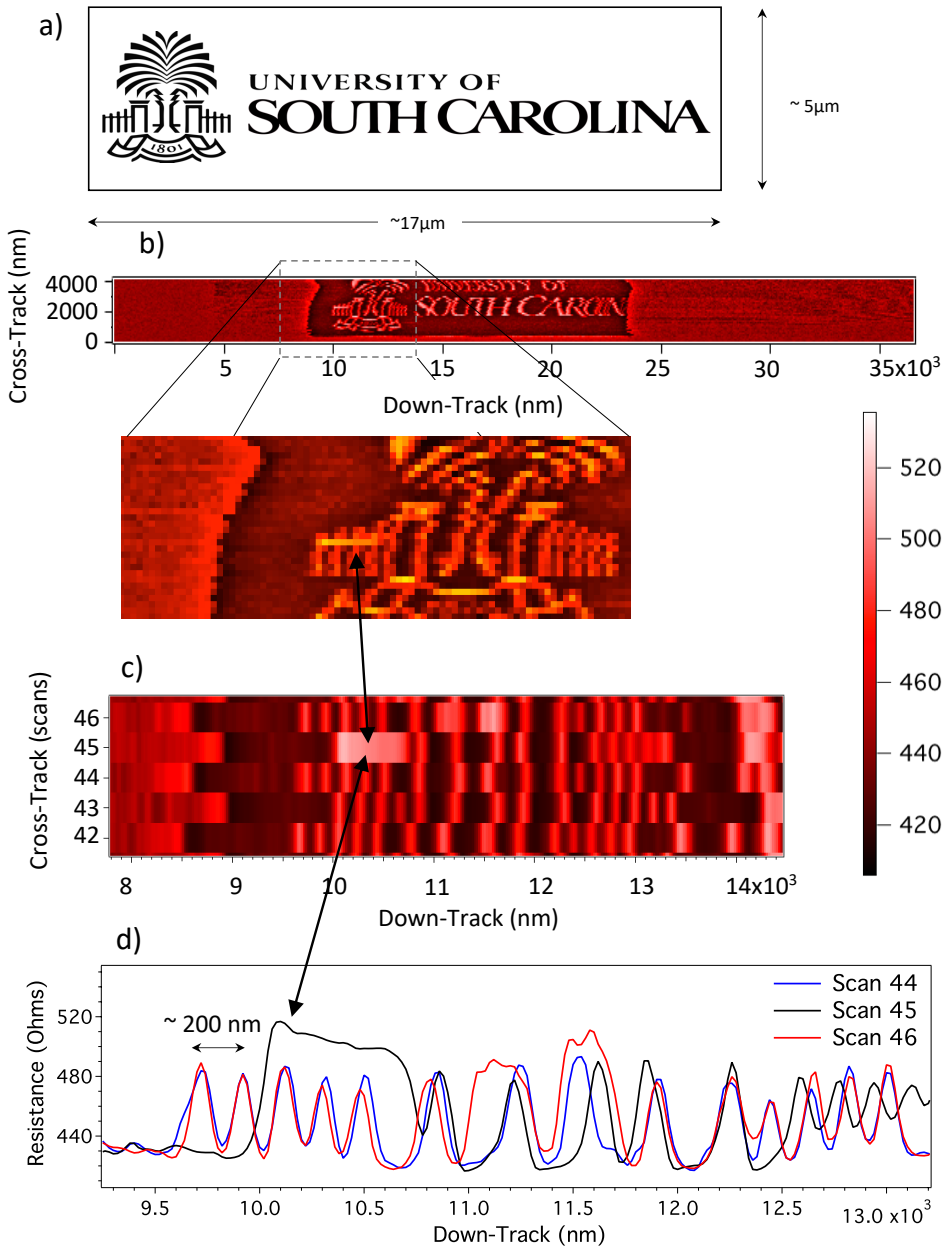

Figure 6.4 a) A bitmap image of the University of South Carolina, b) corresponding read-back image full scale and inset is a zoomed in portion with heatmap range from 420 to 520 Ohms, c) a portion of the read-back image with changed aspect ratio to emphasize resistance profiles that are shown in d). d) resistance profiles for three scans.

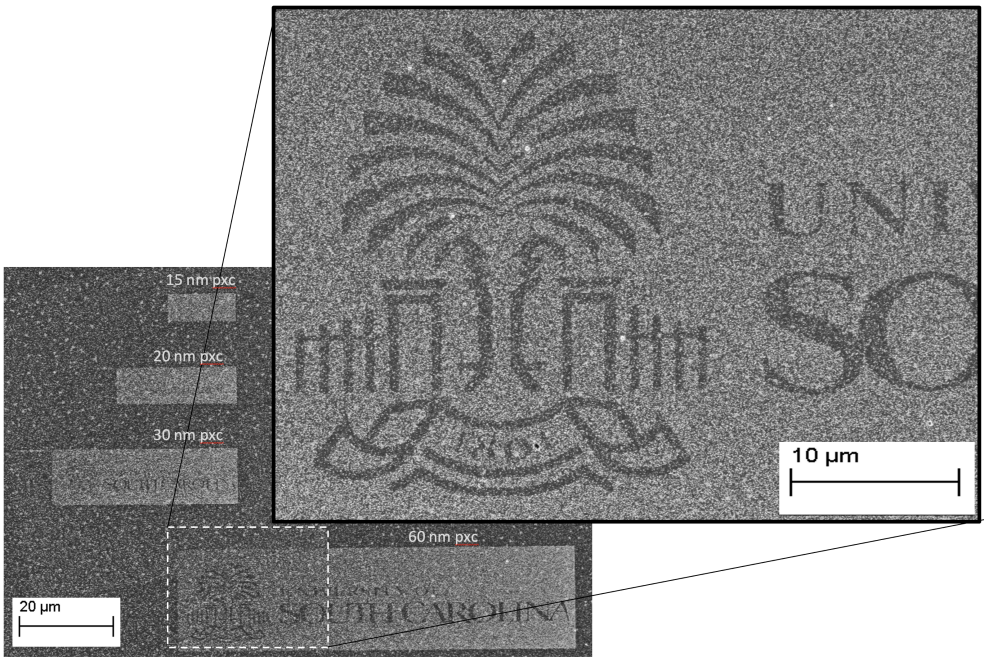

Figure 6.5 a) SEM image of three the assembled magnetic nanoparticles on the recorded UofSC logos from a bitmap image with 4 different pixel coupling values.

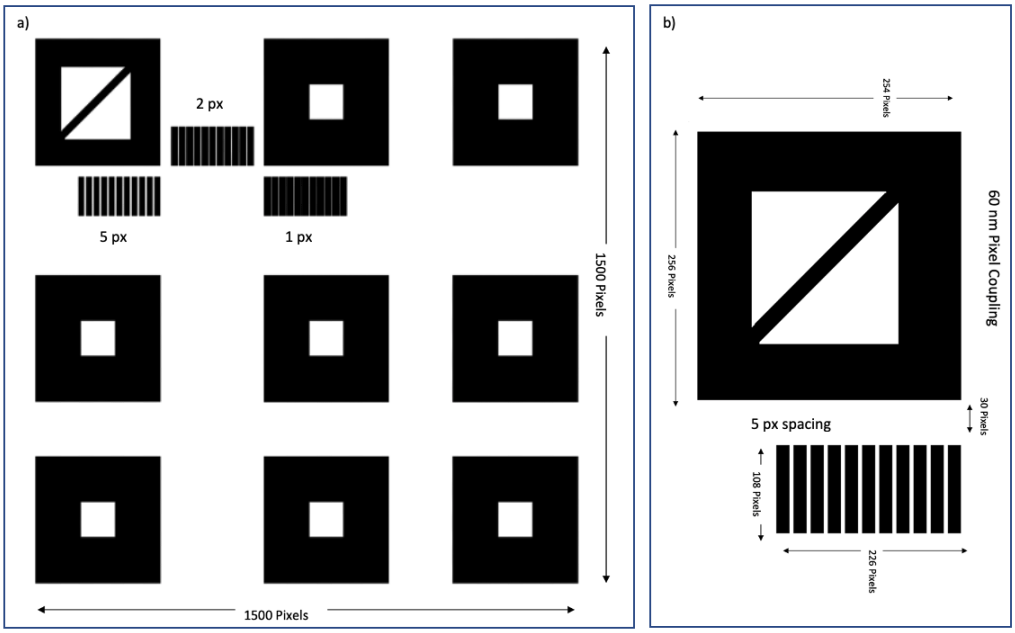

Figure 6.6 a) Full bitmap image with $1500px \times 1500px$ for recording and read-back b) zoomed in top left reagion with rectangular line sets each with 5, 2, 1 pixel spacing

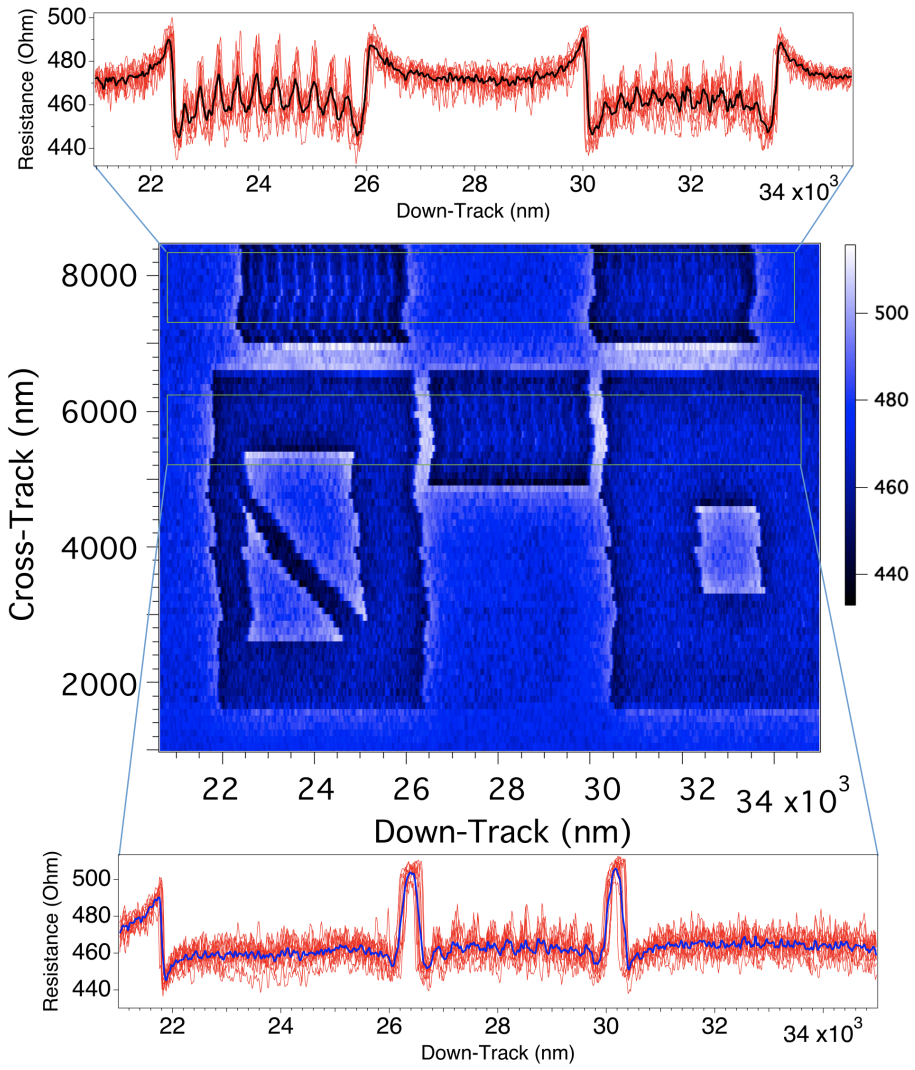

Figure 6.7 Read-back map of top left part of the bitmap image with averaged line scans

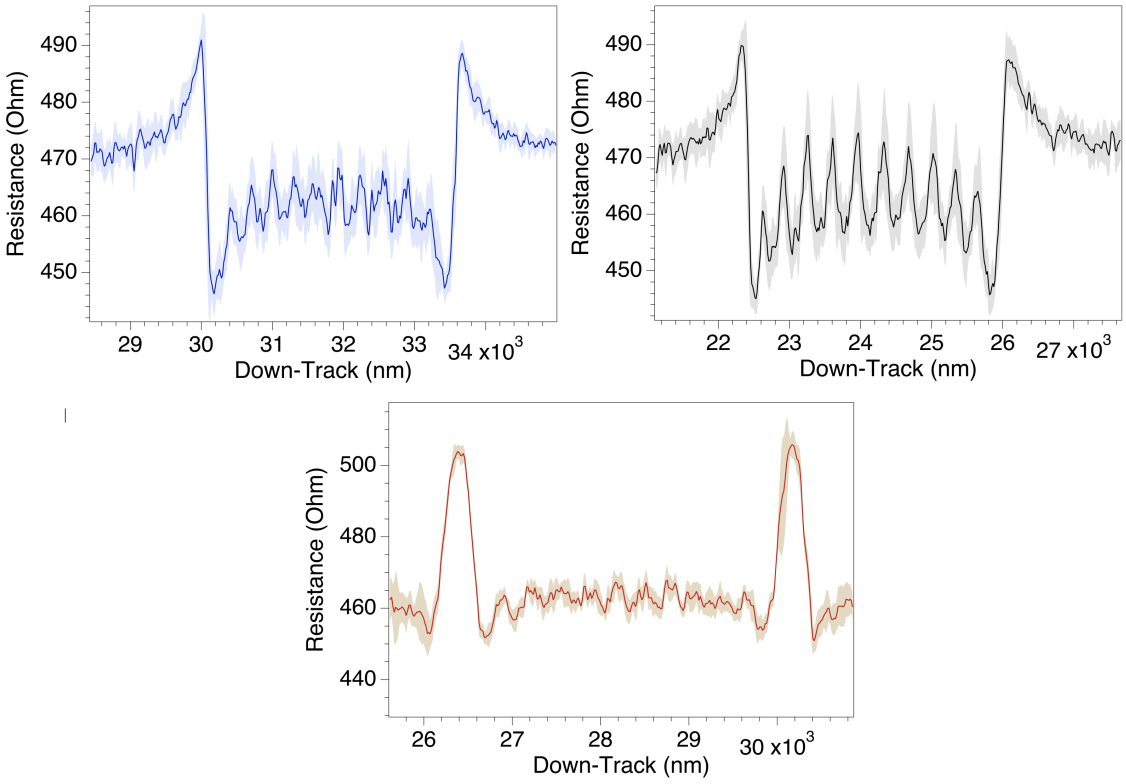

Figure 6.8 Read scans averaged for 5 pixels spacing (black curve), 2 pixels (green curve), one pixel (blue curve). The shaded area for each plot is representing standard deviations

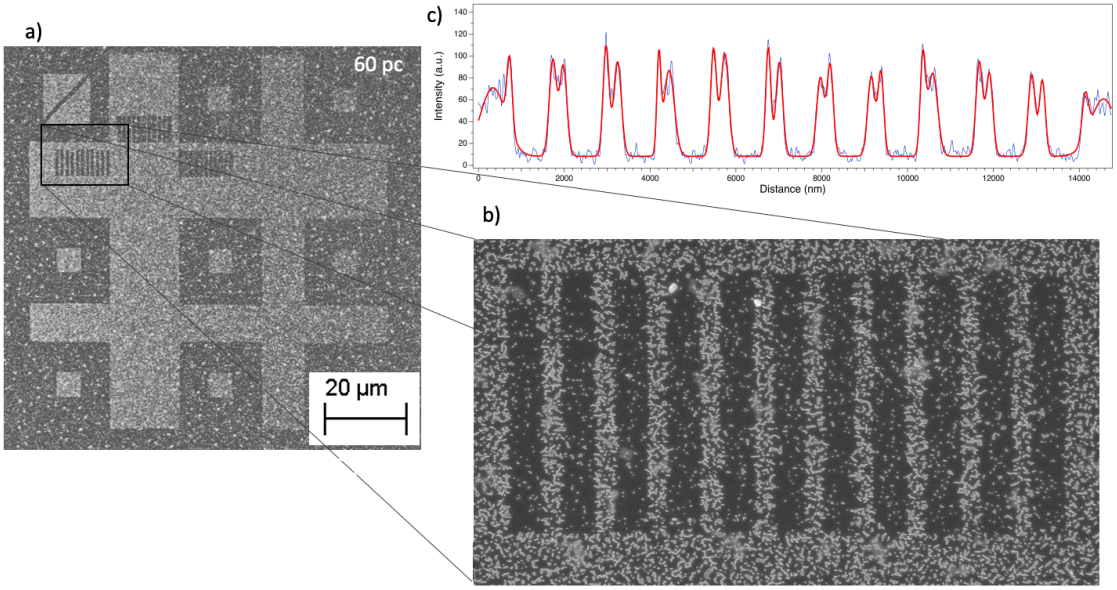

Figure 6.9 SEM image of 15 nm diameter particles self-assembled on the bitmap-recorded image. a) Full scale image, b) zoomed in region of lines with 5 pixels spacing, and c) corresponding line profiles

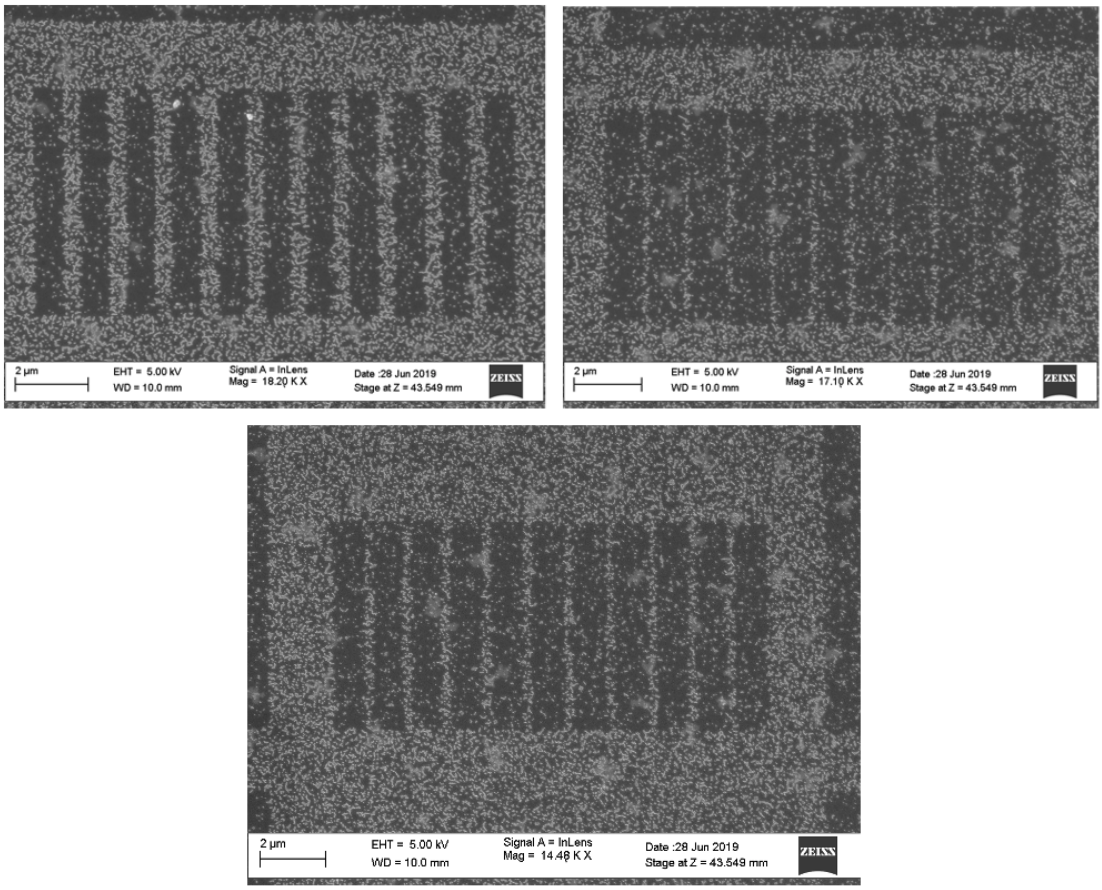

Figure 6.10 SEM images of three line regions for 5 pixels spacing (top left), one pixel spacing (top right), and 2 pixels spacing (bottom)

Chapter 7

Real Time Monitoring of Magnetic Nanoparticles Self-assembly

In previous chapters, the self-assembly of nanoparticles was studied with electron microscopy techniques. Since the assembly of the nanoparticles happens rapidly, imaging does not provide detailed information about the dynamics of the process. One way to see how and how fast nanoparticles self-assemble is to monitor diffraction and scattering of the particles. This chapter explores the real-time self-assembly of iron oxide nanoparticles in hexane onto the parallel recorded lines with 1000 nm spacing on perpendicular disk drive media. We also show that this technique can be used to see the effects of the addition of polar solvent to nanoparticle solution and study the hydrophobic interaction of magnetic nanoparticles with colloidal quantum dots.

7.1 Experimental Setup for real-time measurements

First, a Polytetrafluoroethylene (PTFE) fluid cell with high resistance against solvents is designed. The fluid cell contains an inlet that allows the flow of nanoparticles to a 1 cm cavity where the disk drive medium is placed and has an outlet that removes the fluid from the chamber. The chamber is sealed with a class top via a vacuum pump. Three syringe pump systems can be used to control nanoparticle flow. A laser beam with 632 nm wavelength is chopped at 2.5kHz, and two lock-in amplifiers read the scattering and diffraction outputs, respectively. The diffracted light (spot)

is then observed by a CMOS camera and a photodetector (to monitor the diffracted pattern). Another detector controls the scattered light (to eliminate the background scattered light), and the whole process is monitored by a CCD camera attached to a TV. The fluid cell and real-time measurement setup are demonstrated in figure 7.1.

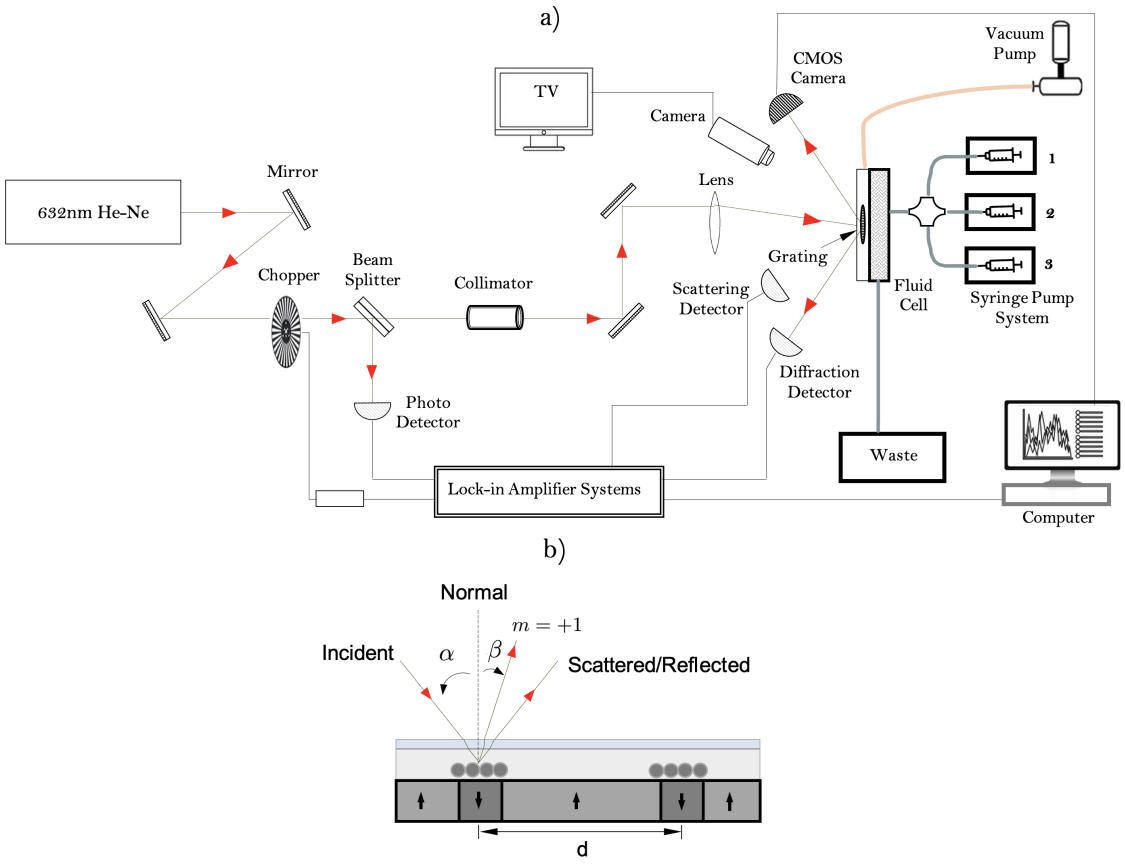

Figure 7.1 a) Real-Time Nanoparticle Diffraction Measurement Setup b) cartoon of diffracted and scattered light in the fluid cell

Once the magnetic nanoparticles are injected into the fluid cell, particles assemble within the lines onto the media and form a grating. The incident light hits the media with angle α less than 5° and then diffracts with angle β, which is related to wavelength and grating spacing a with the following equation:

$$m\lambda = a(\sin\alpha + \sin\beta) \tag{7.1}$$

here m is diffraction order, both CMOS camera and diffraction detector detects light from $m = 1$ or first order diffraction. The relationship between diffraction detection and scattered detection is linear in each detector; the correct magnitude to subtract is found by calibrating the relative difference in scattered signal between the diffraction detector and the scattering detector:

$$I_{d,DD} = I_d - mI_{s,SD} \tag{7.2}$$

.

where $I_{d,DD}$ is first order diffraction, I_d is measured diffraction intensity with diffraction detector and $I_{s,SD}$ scattered light measured by scattering detector ($I_d = I_{d,DD}+I_{s,DD}$), m is linearity between two actual measured values. In our measurement for 4 concentrations or nanoparticles (7 μL , 14 μL , 21 μL , 28 μL) the value of m is averages to 4.28.

7.2 Concentration Tests

To test the setup, different concentrations of aqueous nanoparticle solutions were made. Three concentrations (5 μL , 15 μL and 30 μL) of PrecisionMRX particles were added into three beakers containing 20 mL Di water. Each beaker is first vortexed for 30 seconds, then injected into the fluid cell and left on the media after the injection ends. When the fluid reaches the recorded region of the disk drive, forces due to the extreme field gradient pull nanoparticles towards the transition, and the diffraction signal starts to pick up almost instantly. Fluid injection/flow is continuous for 250 seconds and shows a smooth curve for diffraction (Figure 7.2). When the flow stops, the diffraction signal slows down and continues to increase and oscillate at a slower rate. The continuous flow shows the exponential increase in diffraction; however, adding another flowing force to the recorded media is not ideal when studying the self-assembly of nanoparticles due to the magnetic forces. Therefore, we proceed with

the rest of the experiments by stopping the injection when the fluid cell chamber is filled with nanoparticle solution. That way, we only consider the magnetic force due to the recorded patterns on the medium.

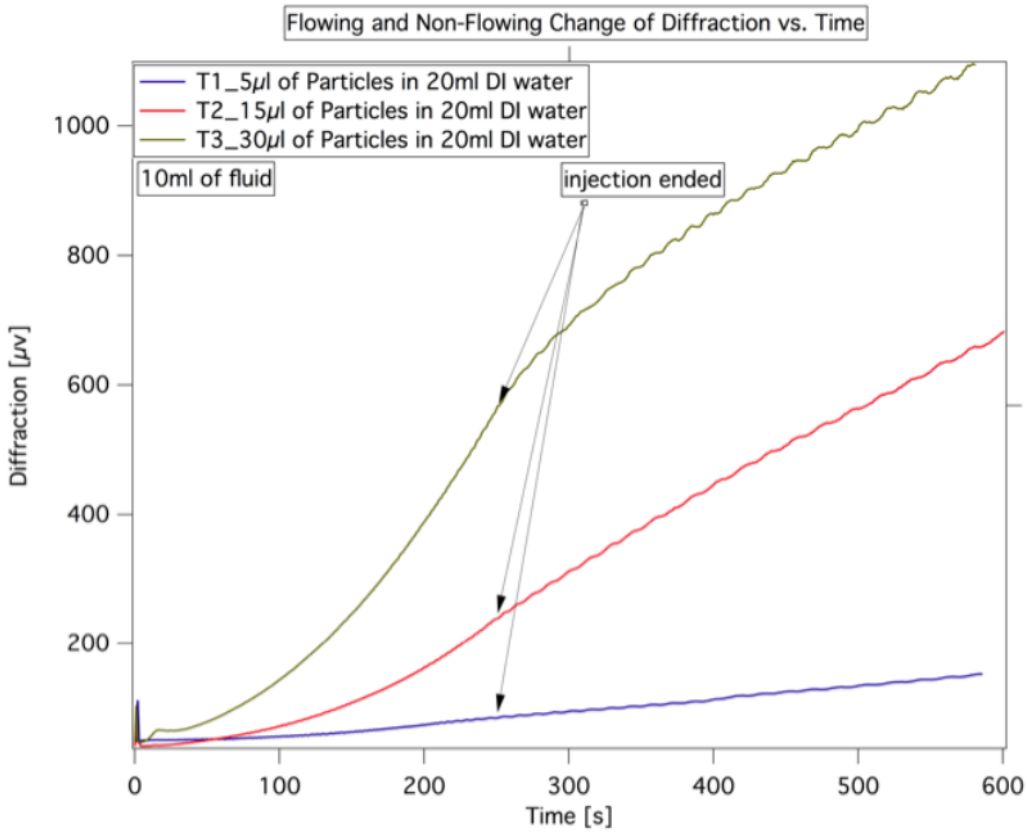

Figure 7.2 Diffraction signal for 3 concentrations in aqueous solution compared for flowing and non-flowing solution

7.3 Monitoring non-aqueous self-assembly in real-time

In this section we consider non-aqueous suspension of 25 nm iron oxide nanoparticles coated with oleic acid in hexane. Four concentration (7 μL , 14 μL , 21 μL , 28 μL) of non-aqueous PrecisionMRX particles were added into four beakers each containing 5 mL anhydrous hexane.

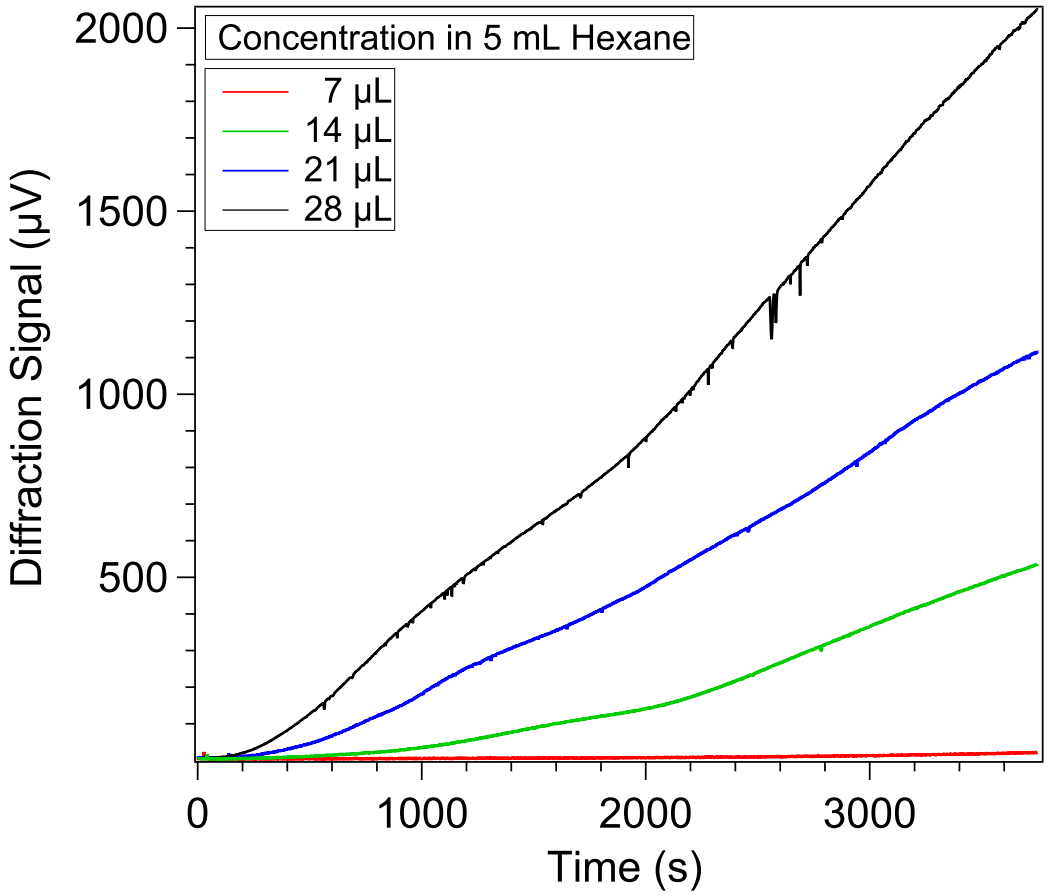

Figure 7.3 Diffraction signal for four concentrations in hexane

We monitor diffraction and scattering signals for about one hour for each concentration. Figure 7.3 shows diffraction profiles over time for four concentrations. Although the lowest concentration (7 μL red curve) has the lowest diffraction intensity, diffraction from the lines is still visible to the eyes after the experiment. The diffraction curve for this concentration is separately plotted in Figure 7.5. For concentrations (14 μL , 21 μL, 28 μL) the diffraction intensity doubles at 3600 seconds, from 500 μV for 14 μL, to 1000 μV for 21 μL, and to 2000 μV for 28 μL. The highest concentrations show more noise because nanoparticles scatter light more. Figure 7.4 shows the scattering signal as a function of time for the same concentrations. Note that the scattering signal stays flat over time and is much less than the diffraction

signal.

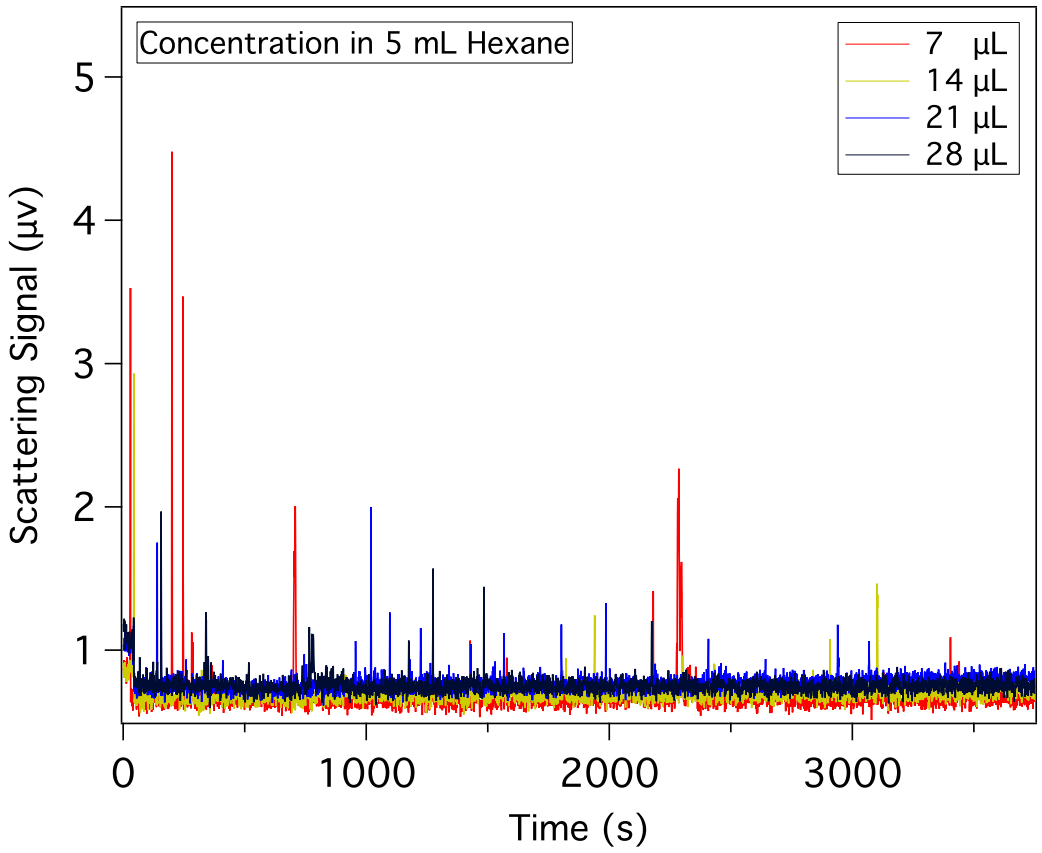

Figure 7.4 Scattering signal for four concentrations in hexane

From Figure 7.3, It is evident that 7 μL barely triggers self-assembly at short times; as concentration increases, the diffraction signal increases. Also, the behavior of the diffraction plots for each concentration shows an initial boost at 1000 seconds, becomes steady until 2000 seconds, and eventually starts to increase again beyond 2000 seconds. To see these changes in the curves, compare them by taking the first derivatives of the diffraction. For that, each signal was averaged and interpolated to reduce the background noise.

Figure 7.5 shows the diffraction plot for 7 μL, which has been averaged using IgorPro software with *Interpolate* function. The function converts the extensive uneven

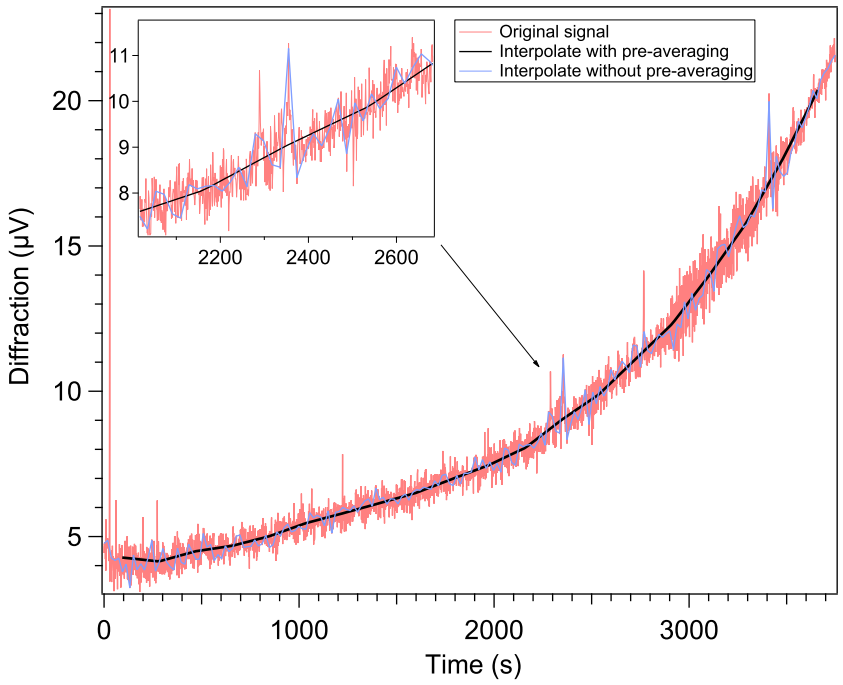

Figure 7.5 Scattering signal for 4 concentrations in non-aquesous (hexane) solution

data set into evenly spaced (x,y) pairs, first without averaging (blue curve) and then with averaging (black curve). Figure 7.6 shows the first derivative for each concentration. For the lowest concentration (top left plot in Figure 7.6), it seems that the self-assembly happens at larger times. For 14 μL concentration, the slope change is positive for the first 1400 seconds, is steady for 300 seconds, and suddenly increases at 2000 seconds and beyond. Similarly, for 3 and 4 times, concentration slope change rapidly increases but eventually drops at 1500 seconds and slowly increases and drops again at 3600 seconds.

First derivative for all concentrations are compared together in Figure 7.7. Note that all four plots follow the same behaviour.

From these results, we hypothesize that the first formation or the first increase in the diffraction graph, regardless of the time it takes, is pulling the particles out

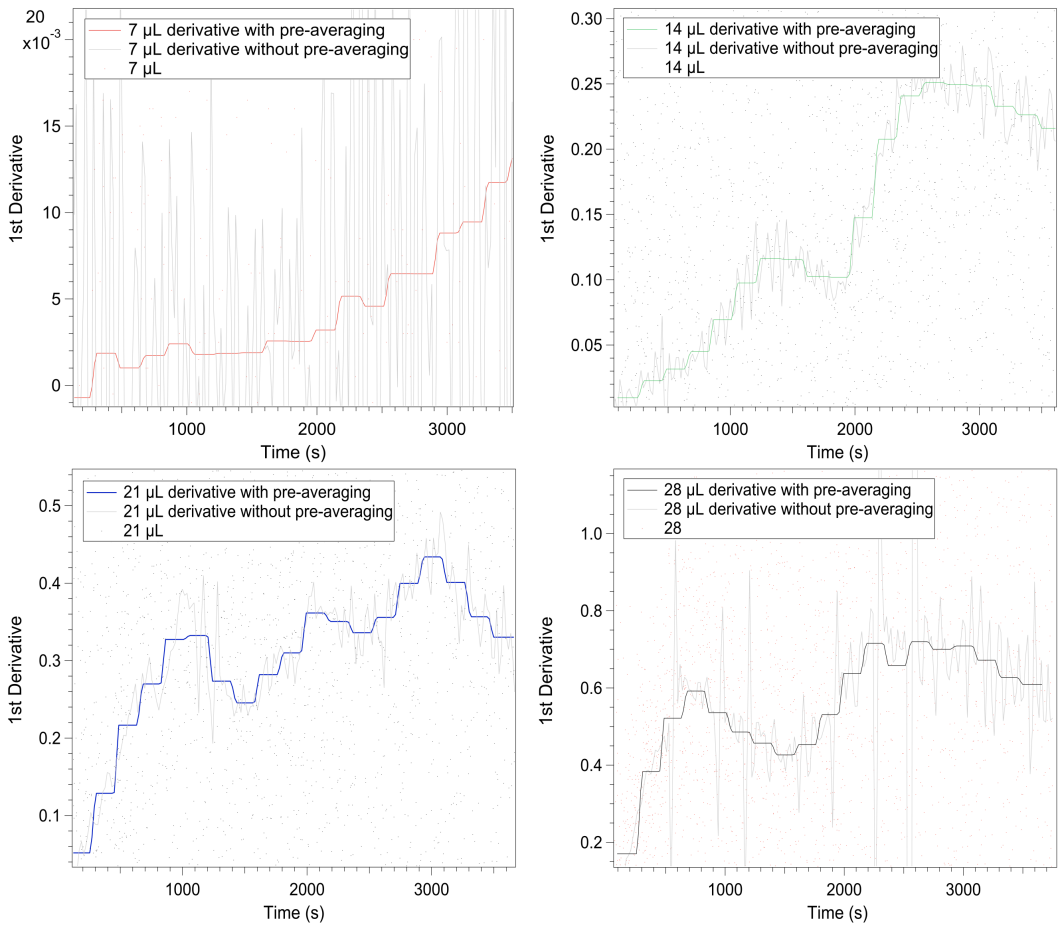

Figure 7.6 First derivative plots of diffraction signal for four concentrations after noise is removed, each derivative plot is compared to the original noisy signal

of the lower layer of the fluid, following with self-assembly. As they assemble, they get more diffraction, and consequently, diffusion happens, and other particles have to come down, fill in the space, and self-assemble. The diffusion process takes time compared to the assembly process. As the particles come from the upper layers of the fluid, they block and scatter the incident light and prevent it from reaching the diffraction grating. Therefore, the diffraction signal increases and then momentarily decreases as all the particles diffuse down and assemble onto the grading. Notice the decrease happens sooner when the concentration is high; the higher the concentration

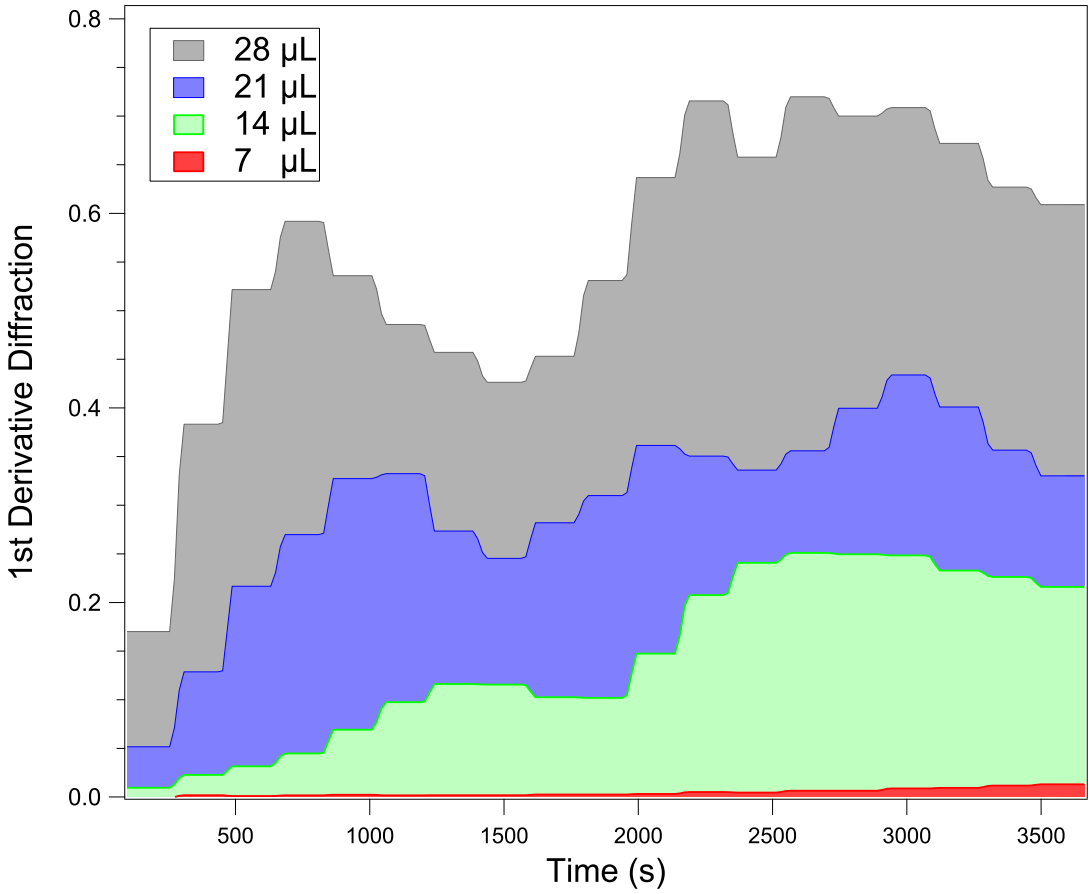

Figure 7.7 First derivatives for all concentrations in 5 mL hexane compared together

of nanoparticles, the faster self-assembly and the diffraction signal drop.

The diffusion equation, also called Fick's second law of diffusion, is a second-order differential equation for space and a first-order differential equation for time.

$$\frac{\partial c}{\partial t} = D\frac{\partial^2 c}{\partial x^2} \tag{7.3}$$

Therefore, there are two boundary conditions for spatial dependence and a single initial condition for the time-dependence. The first boundary condition is that the concentration must be finite everywhere, and the total number of particles in the solution is fixed n_0. For the time-dependent solution, the initial condition is that at

$t = 0$, all particles are concentrated at the yz plane. As such, the solution for the differential equation is:

$$c(x,t) = \frac{n_0}{A(\pi Dt)^{1/2}} e^{-\frac{x^2}{4Dt}} \tag{7.4}$$

Here A is the area, and D is the diffusion constant.

The diffusion equation shows that the rate of change of concentration is proportional to the second derivative; if the concentration changes sharply from point to point, then the concentration changes rapidly with time.

The solutions of the diffusion equation can be used to predict the concentration of particles at any location. We can also use them to calculate the net distance through which the particles diffuse in a given time or vice versa.

To calculate the net distance traveled on average by particles in a time t with the diffusion constant D, one needs to calculate the probability that a particle will be found at a certain distance from the origin and then calculate the average by weighting each distance by that probability. The number of particles in a in a thickness dx area A at x, with $c = cAN_A dx$ the probability that any of the particles is in the slab is therefore $cAN_A dx$.

$$<\text{x}> = \int_0^\infty \frac{xcAN_A}{N_0} dx = \int_0^\infty \frac{x}{N_0} \frac{n_0}{A(\pi Dt)^{1/2}} e^{-\frac{x^2}{4Dt}} dx = \frac{1}{(\pi Dt)^{1/2}} \int_0^\infty x e^{-\frac{x^2}{4Dt}} dx = 2(\frac{Dt}{\pi})^{1/2}$$

The average distance of diffusion varies as the square root of the lapsed time. Using the Stokes-Einstein relation for the diffusion coefficient D, the time it takes for a particle with radius r in a solvent with viscosity η is:

$$t = \left(\frac{3\pi^2 \eta r x^2}{2kT}\right) \tag{7.5}$$

For a particle with 12.5 nm radius, in hexane with viscosity 0.000297 $\frac{Ns}{m^2}$ at room temperature, the time it takes to travel 100 nm is 14 ms, indicating that self-assembly happens rapidly for the particles near the surface of the media. However, the fluid is nearly 500 μm; for the particles to diffuse from a layer located at that distance, the total time it takes to diffuse is 3552 seconds.

7.4 Real-time monitoring diffraction signal when ethanol is added to the solution

In the previous chapters, we showed that small changes to the polarity of nanoparticle solution could dramatically change the self-assembly. To determine how the diffraction signal changes when ethanol is added to the solution, we pick a fixed concentration 14 μL and add different ethanol volumes to the solution.

Figure 7.8 shows the diffraction signal for 14 μL with different volumes of added ethanol. The lowest concentration with zero ethanol is compared when 50 μL, 75 μL, and 100 μL are added to the solution. The diffraction signal is reduced overall compared to the case with no ethanol. However, the diffraction signal triggers much faster in the case when 50 μL added ethanol, such that at 1000 seconds, the diffraction signal is nearly 150 μV. It takes 500 more seconds for the cases with 75 μL and 100 μL added ethanol and 1000 seconds for cases with zero ethanol to reach such value. Such rapid increase in diffraction when colloid is destabilized with a specific volume of ethanol has been observed in the case of aqueous nanoparticles when the colloidal suspension was destabilized with added salt (PBS). [93] Note that the diffraction signal for 100 μL added ethanol, behaves similar to the case with no added ethanol. A possible reason is ethanol reduces the oleic acid layer of the particles and forces

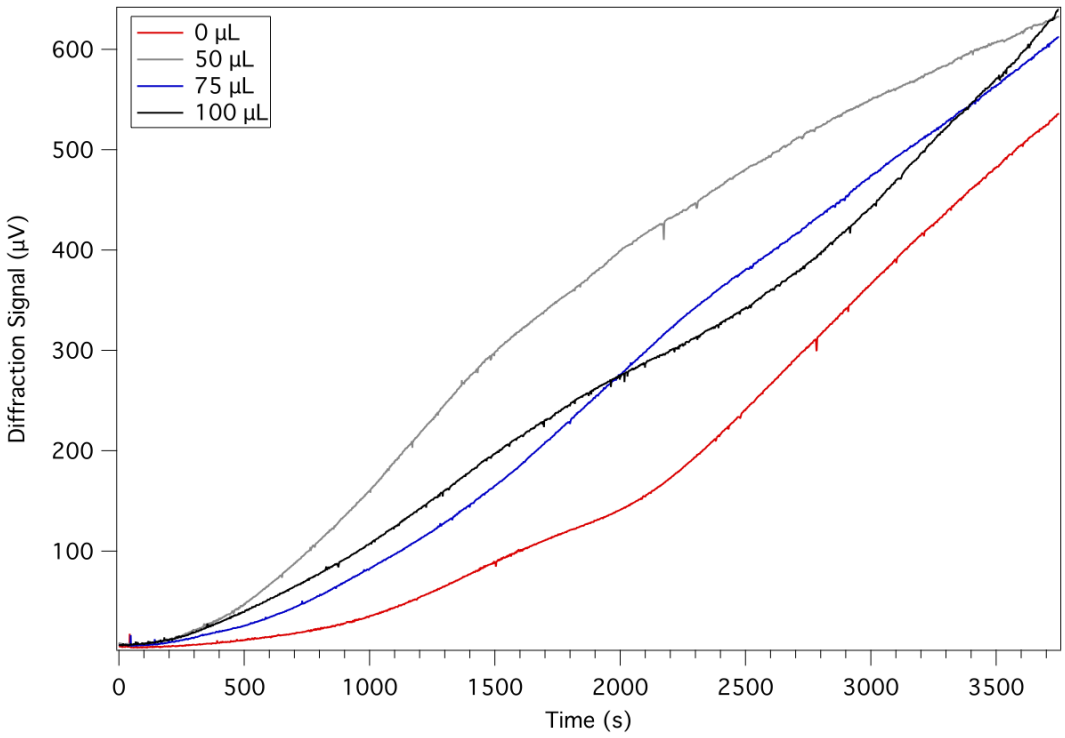

Figure 7.8 Real-time diffraction signal curves for the case where three concentrations of ethanol is added to the base nanoparticle solution

them to aggregate and form larger clusters of nanoparticles. These large clusters diffuse faster to the disk drive surface but like with the case with no ethanol, they initially form the first layers, and then the uppermost particles diffuse down to start the second layers. This behavior could be observed in the case where 50 μL ethanol is added as well if the experiment is set to run for longer times. Figure 7.9 shows the first derivative of the diffraction signal for 14 μL with different volumes of added ethanol.

7.5 Real-time monitoring of Iron Oxide and Cadmium Selenide quantum dots self-assembly

Recently, there has been an interest in developing materials where metal oxide and semiconductor nanoparticles are assembled via strong interparticle interactions. Such

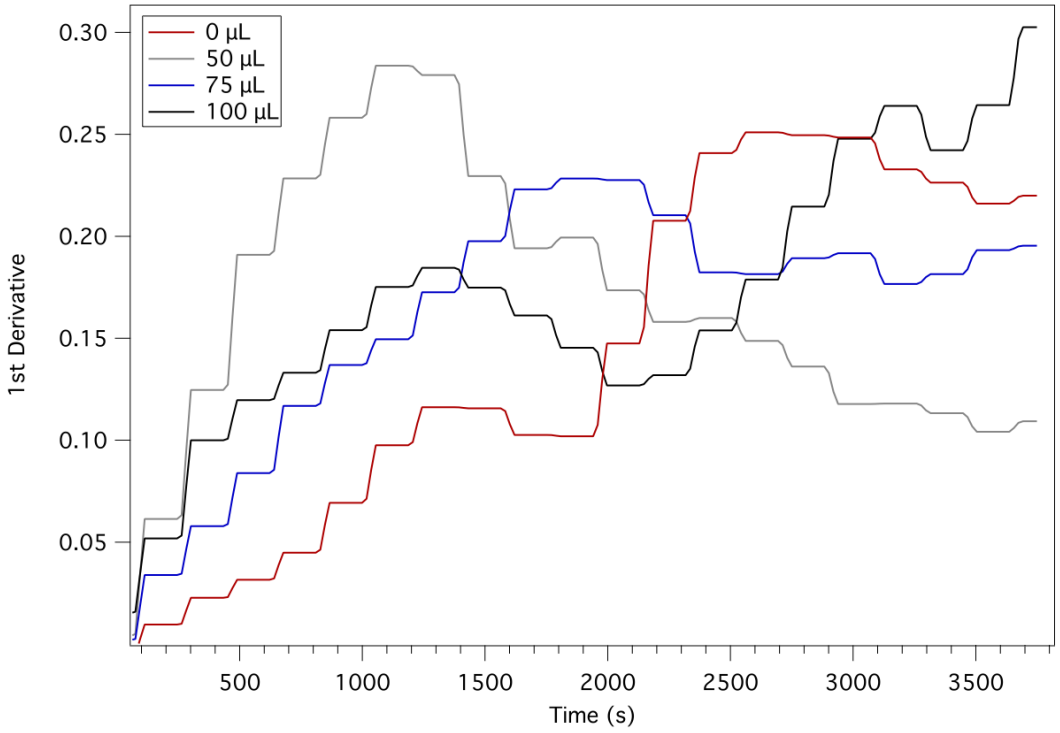

Figure 7.9 First derivatives of diffraction signal for the case where three ethanol concentrations are added to 14 μL in 5 mL hexane

materials can be achieved using various techniques, such as evaporation, lithographic patterns, Langmuir Blodgett, and molding techniques. Here, we demonstrate the hydrophobic assembly of fluorescent semiconducting cadmium selenide (CdSe) / Cadmium Sulfide (CdS) core/shell quantum dots (QDs) onto magnetically patterned substrates of iron oxide nanoparticles with oleic acid coating.

CdSe/CdS quantum dots are light-emitting nanoparticles with diameters between 1 to 10 nanometers. These quantum dots are usually functionalized with surface capping ligands that vary in structure, making them colloidally stable. They show high optical tunability properties through their size and surface functionalization, which have significant effective dielectric constant and adsorption coefficients. Quantum dots with such properties are usually used in photovoltaics, light-emitting diodes, and photodetectors. Our goal here is to assemble fluorescent quantum dots into

patterns using iron oxide nanoparticles as templates to measure nanoparticle-surface interactions and ultimately control the emission of fluorescence light.

First, we prepare a magnetic template with magnetic recording, consisting of 8, $500 \times 50\ \mu\,\mathrm{m}^2$ rectangular regions with different spacings. The surface of the template was coated with oleic acid-capped iron oxide nanoparticles in hexane for 20 minutes. The media is observed with dark-field optical microscope to confirm the assembly of iron oxide nanoparticles (Figure 7.10 a). Next, 1 mL of CdSe quantum dots in toluene were deposited on the magnetic template with iron oxide nanoparticles and was spin-coated for 1 minute at 1800 RPM. Figure 7.10 b shows the media with iron oxide and deposited quantum dots; the solid line is the result of the dried quantum dots solution after the spin coating (inset shows the fluorescent image of the same line. Figure 7.10 d shows the fluorescent image of the 1000 nm and 500 nm spacing, showing that oleate-coated quantum dot emitters assembled on iron oxide nanoparticles. At 1000 nm spacing, quantum dots seem to assemble very well and show distinct lines, whereas, for 500 nm spacing, distinct lines are not as visible. Emission intensity for both spacings is shown in Figure 7.10 c, which corresponds to the wavelength of 570 nm. For 500 nm spacing, the intensity is higher because of the large aggregates for particles on the surface of the media. Note that for the coupon before quantum dots deposition, the emission is flat.

With the first evidence of quantum dots assembly on iron oxide nanoparticles observed with fluorescent microscopy, we next study the self-assembly of iron oxide and quantum dots in real-time. For that, we use the fluid cell set up in Figure 7.1 to measure the change in diffraction efficiency after the quantum dots solution is injected into the fluid cell. We use three syringe pumps, as shown in Figure 7.1: First, for pure hexane, to clean the surface of the media and any residual particles from previous runs. Second, for oleic acid capped iron oxide nanoparticle solution, and third, for oleic acid capped quantum dots nanoparticles solution. We disperse

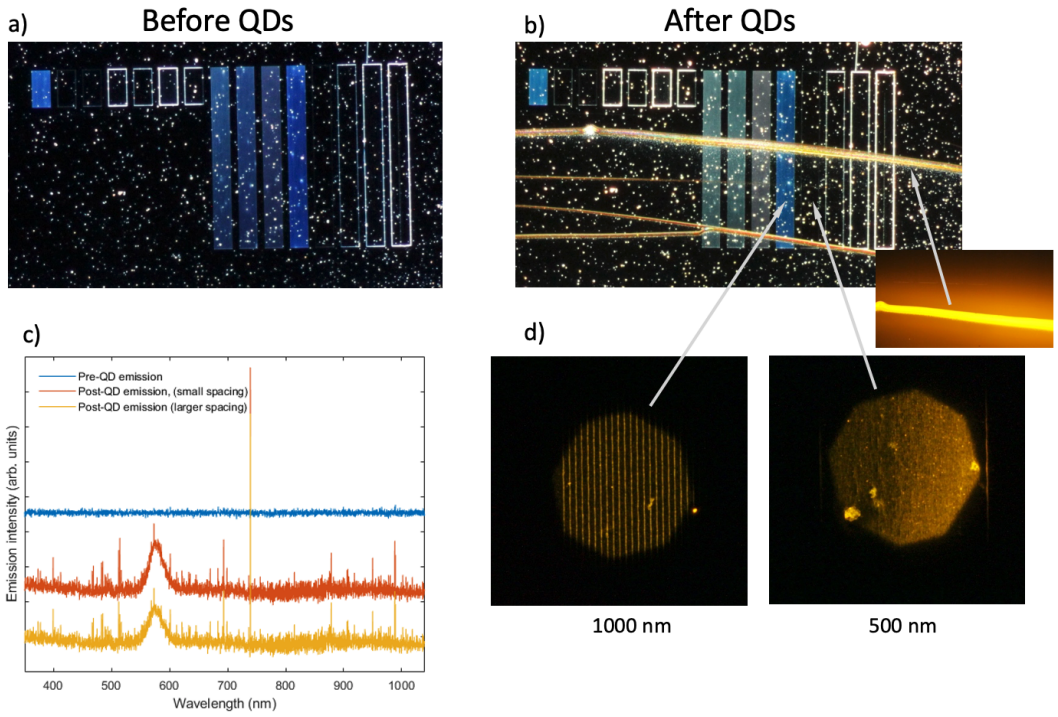

Figure 7.10 Optical image for a) iron oxide self-assembly b) when quantum dots deposited on iron oxide self-assembly, c) emission intensity plot for before, and after quantum dots deposition for 500 nm spacing region (red curve) and 1000 nm space region (yellow curve), d) Flourescent microscope image of quantum dots self-assembled on iron oxide with 500 and 1000 nm spacings

the quantum dots stock solution into hexane instead of toluene to observe real-time diffraction change and quantum dots assembly with iron-oxide nanoparticles.

Figure 7.11 shows a one-hour real-time observation of diffraction and scattering signals for iron oxide nanoparticles and cadmium selenide quantum dots. At first, 10 mL, clean hexane is injected into the fluid cell, and the sharp peak for both diffraction (blue curve) and scattering signal (red curve) at 100 seconds happens when the fluid reaches the laser spot on the media. Then 10 mL of iron oxide is injected, and at 300 seconds, the flow of iron oxide stops. At this time, all the tubing is clamped, the fluid cell is in equilibrium, and the iron oxide solution stays on top of the media until the diffraction signal reaches 12 μV. Next, the iron oxide solution is pushed to waste with

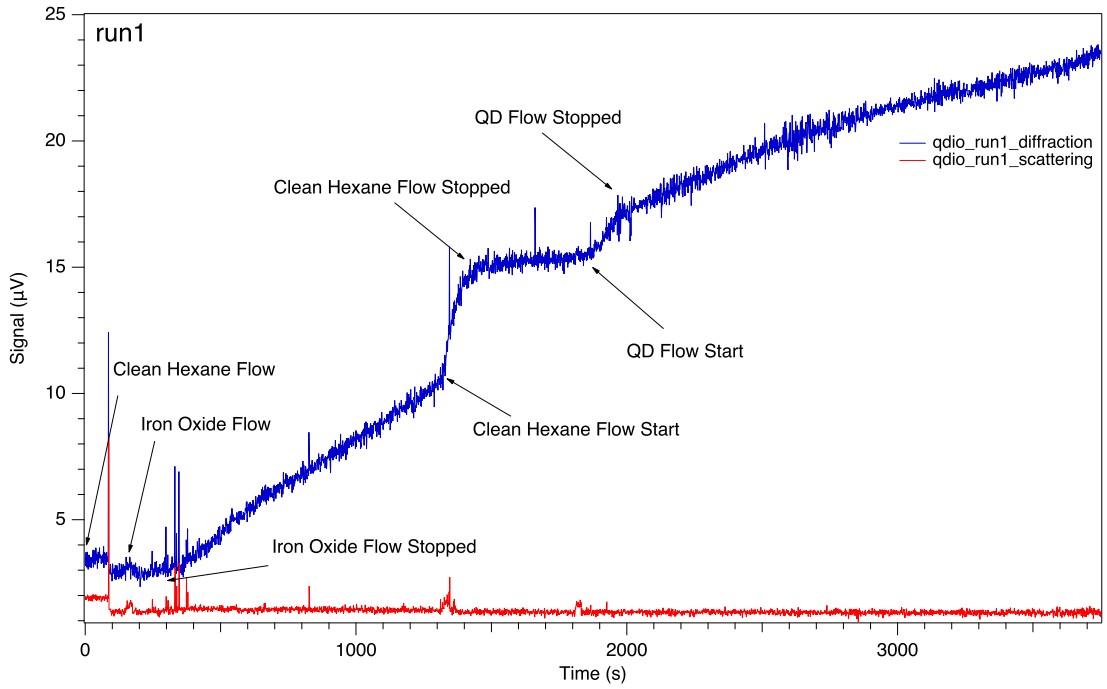

Figure 7.11 Real-time diffraction (blue curve) and scattering (red curve) signal of iron oxide nanoparticles and cadmium selenide quantum dots

clean hexane solution, and at 1350 seconds, the diffraction signal rapidly increased from 12 μV to 15 μV. This is significant because the scattering signal does not change or increase. This means that clean hexane flow removes the non-specific assemblies between the grating where the magnetic field gradient is minimal and thus enhancing the diffraction efficiency. At 1500 seconds, clean hexane flow stops and let sit on the media. As expected, the diffraction signal from 1500 - 2000 seconds stays steady. Finally, the clean hexane is removed, and a solution of quantum dots is introduced to the fluid cell. As quantum dots flow past the medium, the diffraction signal linearly increases (2000 s - 2100 s). When quantum dots solution flow stops on the medium, the diffraction signal increases but not linearly until it reaches 23 μV at 3600 seconds. These results show a strong hydrophobic interaction between oleate-caped cadmium selenide quantum dots and oleic acid-coated iron oxide nanoparticles.

To confirm even further, we remove the quantum dots solution from the fluid cell

in the same experiment and inject pure hexane into the fluid cell to wash the media's surface. If the quantum dots are assembled to the iron oxide nanoparticles, then the diffraction signal should not decrease.

This is shown in Figure 7.12. The quantum dots are set in the fluid cell for 1500 seconds beyond 3600 seconds, and the diffraction signal increases from 23 μV to 28 μV. When the solution is removed and the fluid cell left empty for 1500 seconds, the diffraction signal drops to 24 μV and is not steady. This is due to the increased scattering as the fluid dries. However, when clean hexane is injected once again, the scattering signal drops, and the diffraction signal is increased back to 29 μV and stays steady up to 3600 seconds.

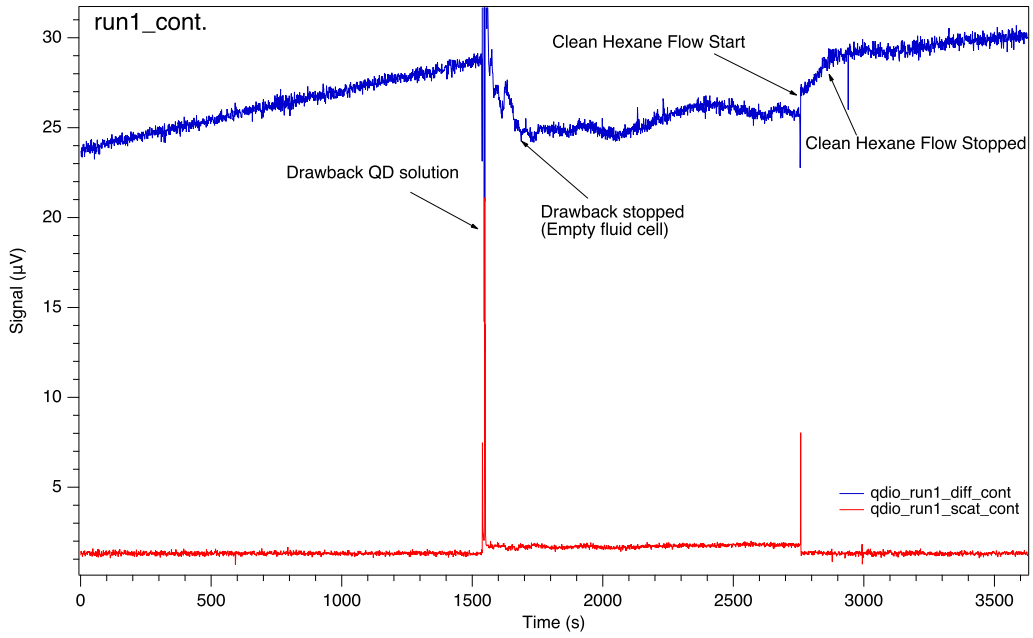

Figure 7.12 Continued Real-time diffraction (blue curve) and scattering (red curve) signal of iron oxide nanoparticles and cadmium seleninde quantum dots after cleaned with hexane

Chapter 8

Summary and conclusion

In this dissertation we have conducted experimental studies to better understand and control self-assembly of magnetic nanoparticles using extreme field gradients at the surface of the disk drive medium. Forces due to the field gradients at the transition where media magnetization is switching its orientation were theoretically described and plotted.

We explored field equations due to medium transitions and effects of soft underlayer on self-assembly. We showed that when *two* magnetic transitions are near each other, magnetic nanoparticles can self-assemble above them in two different ways. The final self-assembled structure is sensitive to minute adjustments in local magnetic field, field gradient, and/or nanoparticle ligand length/folding (via the addition of ethanol). These adjustments are able to completely transform the observed nanoparticle pattern: a single wide stripe spanning both transitions (hexane) can be converted to two separated stripes above the two transitions (hexane with ethanol). In particular, the formation of the self-assembled wide stripe is not expected if one thinks of magnetic transitions as sources of very large magnetic field gradients that pull particles to the surface. However, the magnetic field gradient is "smoothed" out between the two transitions due to their relative closeness (roughly 100 nm) and due to the existence of the thick, soft magnetic underlayer component of the hard disk medium.

The observed changes in the assemblies can be understood with the aid of particle-level Langevin simulations and a careful calculation and analysis of the stray field gra-

dient produced by the disk drive template. The same trends are seen in simulation as in experiment, provided the soft underlayer is included and the ligand length shrinks with addition of ethanol. A decrease in ligand length brings magnetic nanoparticles closer to the disk surface, altering the magnetic force sufficiently to make the nanoparticles assemble in different locations.

Change in parameters such as spacing between magnetic stripes, applied voltage to the head, lubrication, allows control over self-assembly to achieve mono- or bilayer assembly, nanoparticle chains with varying width and lengths, or single line assembly. At specific spacing, we have shown that nanoparticles achieve minimum edge roughness with highly ordered features that form two-dimensional layers with so-called "hexatic ordering". The degree of hexatic ordering was quantified using the G_6 bond-orientational order parameter, and is found to deteriorate when ethanol is added. The hexatic phase is also less ordered for wider spacing d between lines. For both cases, with and without added ethanol, we quantitatively calculated line width growth and number of non-specifically assembled particles.

We have also demonstrated two approaches to record magnetic patterns on a disk drive medium: Bitmap recording, that outputs positive and negative voltage based on pixel intensity of a bitmap image to magnetize the medium, and parallel line recording, where the DC current is applied to the write head to magnetize the medium grains as it is pushed and pulled across the disk drive surface.

The importance of the read head in both methods was explained. Read-back profiles from the recorded regions for each approach to confirm the quality of the recording were demonstrated. The write head width was calculated from FWHM of the read-back signal of parallel lines, and head sensitivity was tested for 3 line sets with different spacing from a bitmap image. The distortion in the read-back images could be due to the read scans itself. The heads are designed to process information in picoseconds, writing with longer times allows weaker fields to reverse medium grains

and create noisier features. Therefore, the time resolution can be tuned and adjusted to improve the overall equality or recording and reading.

To better understand the dynamics of self-assembly we studied the process in real-time by measuring change in diffraction and scattering intensity as nanoparticles self-assemble. We were also able see the increase to the initial diffraction intensity as a result of hydrophobic assembly of Cadmium Selenide quantum dots on Iron Oxide nanoparticles arrays. While we confirm the sensitivity of self-assembly to the concentration and polarity of the base nanoparticles solution, the change in the diffraction signal for different concentration of added ethanol to the solution is still not clearly understood, further experiments need to be done to explain this behavior.

The knowledge gained from these experiments can be used to design recording head and media deliberately for self-assembly instead of data storage, in order to produce features below 200 nm for specific applications including (but not limited to) MRI contrast agents, superconducting wires, and sensors for magnetic fields. There are many material parameters in the recording system that have yet to be adjusted and explored for nanoparticle assembly, in principal allowing a system with even smaller feature sizes, improved feature quality, and that limit sensitivity to external influences.These include the specific thickness, saturation magnetization, and coercivity of both the medium and the soft underlayer, as well as the size of the recording head and the field it produces. Furthermore, nanoparticle diameter, material, and magnetic behavior can be widely tuned as well.

Bibliography

[1] Mazaher Ahmadi et al. "Application of magnetic nanomaterials in magnetic field sensors". In: *Magnetic nanomaterials in analytical chemistry*. Elsevier, 2021, pp. 327–345.

[2] Anwar Ahniyaz, Yasuhiro Sakamoto, and Lennart Bergström. "Magnetic field-induced assembly of oriented superlattices from maghemite nanocubes". In: *Proceedings of the National Academy of Sciences* 104.45 (2007), pp. 17570–17574.

[3] Nicholas R Anderson et al. "Simulating the Self-Assembly and Hysteresis Loops of Ferromagnetic Nanoparticles with Sticking of Ligands". In: *Nanomaterials* 11.11 (2021), p. 2870.

[4] VM Arole and SV Munde. "Fabrication of nanomaterials by top-down and bottom-up approaches-an overview". In: *J. Mater. Sci* 1 (2014), pp. 89–93.

[5] Manuel Arruebo et al. "Magnetic nanoparticles for drug delivery". In: *Nano today* 2.3 (2007), pp. 22–32.

[6] Y. Bao, J. A. Sherwood, and Z. Sun. "Magnetic iron oxide nanoparticles as T1 contrast agents for magnetic resonance imaging". In: *Journal of Materials Chemistry C* 6 (2018), pp. 1280–1290. ISSN: 2050-7526. DOI: 10.1039/C7TC05854C. URL: http://xlink.rsc.org/?DOI=C7TC05854C.

[7] Gutarowska Beata and Michalski Andrzej. "World ' s largest Science , Technology & Medicine Open Access book publisher :" in: *Capsaicin Sensitive Neural Afferentation and the Gastrointestinal Tract from Bench to Bedside* ().

[8] S Bedanta et al. "Magnetic nanoparticles: a subject for both fundamental research and applications". In: *Journal of nanomaterials* 2013 (2013).

[9] Bharat Bhushan. "Friction". In: *Tribology and Mechanics of Magnetic Storage Devices*. Springer, 1996, pp. 231–365.

[10] Justin R. Bickford. *Analyze Strips ImageJ*. URL: https://imagejdocu.list.lu/doku.php?id=macro:analyze_stripes.

[11] Alexander Böker et al. “Self-assembly of nanoparticles at interfaces”. In: *Soft matter* 3.10 (2007), pp. 1231–1248.

[12] Jose R Borba et al. “Quantitative characterization of hexagonal packings in nanoporous alumina arrays: a case study”. In: *The Journal of Physical Chemistry C* 117.1 (2013), pp. 246–251.

[13] Joel D Brock et al. “Hexatic ordering in liquid crystal films”. In: *Contemporary physics* 30.5 (1989), pp. 321–335.

[14] Hans-jürgen Butt and Michael Kappl. *Surface and Interfacial Forces*. ISBN: 9783527406296.

[15] S.H. Charap. “Thermal instability at 10 Gbit/in/sup 2/ magnetic recording”. In: *IEEE Transactions on Magnetics* 30.6 (1994), pp. 4230–4232. ISSN: 00189464. DOI: 10.1109/20.334044. URL: http://ieeexplore.ieee.org/lpdocs/epic03/wrapper.htm?arnumber=334044.

[16] Jun Chen et al. “Self-Assembly and Directed Assembly of Polymer Grafted Nanocrystals via Solvent Annealing”. In: *Macromolecules* 50.24 (2017), pp. 9636–9646.

[17] Jagadish Chennupati and Amanda Barnard. *Nanoscience: Thinking big, Working Small*. 2019. URL: https://www.science.org.au/curious/nanoscience.

[18] J. M. D. Coey. *Magnetism and Magnetic Materials*. Cambridge University Press, 2010. DOI: 10.1017/CBO9780511845000.

[19] Terence Cosgrove. *Colloid science: principles, methods and applications*. John Wiley & Sons, 2010.

[20] Mohtasebzadeh A. R. Davidson J. Livesey K. Crawford T. M. “Tunability and order in two-dimensional arrays of magnetic nanoparticles”. In: *Advanced Materials Interfaces* (2022). DOI: 10.1002/admi.202201056.

[21] Thomas Crawford. “Pattern Transfer Nanomanufacturing”. In: *APS Southeastern Section Meeting Abstracts*. Vol. 78. APS Meeting Abstracts. Oct. 2011, NC.002, NC.002.

[22] Kathleen Davis et al. “Quantitative measurement of ligand exchange on iron oxides via radiolabeled oleic acid”. In: *Langmuir* 30.36 (2014), pp. 10918–10925. ISSN: 15205827. DOI: 10.1021/la502204g.

[23] Dietrich A Dehlinger et al. “Electric-Field-Directed Assembly of Biomolecular-Derivatized Nanoparticles into Higher-Order Structures”. In: *Small* 3.7 (2007), pp. 1237–1244.

[24] Ahmet F Demirörs et al. “Colloidal assembly directed by virtual magnetic moulds”. In: *Nature* 503.7474 (2013), pp. 99–103.

[25] Patrick Dillmann, Georg Maret, and Peter Keim. “Two-dimensional colloidal systems in time-dependent magnetic fields”. In: *The European Physical Journal Special Topics* 222.11 (2013), pp. 2941–2959.

[26] Berta Domènech et al. “Hierarchical supercrystalline nanocomposites through the self-assembly of organically-modified ceramic nanoparticles”. In: *Scientific reports* 9.1 (2019), pp. 1–11.

[27] Roel PA Dullens et al. “Shape-induced frustration of hexagonal order in polyhedral colloids”. In: *Physical review letters* 96.2 (2006), p. 028304.

[28] Randall M Erb et al. “Composites reinforced in three dimensions by using low magnetic fields”. In: *Science* 335.6065 (2012), pp. 199–204.

[29] EP Furlani. “Analysis of particle transport in a magnetophoretic microsystem”. In: *J. Appl. Phys.* 99.2 (2006), p. 024912.

[30] Hongyu Gao et al. “Entropy Can Bundle Nanowires in Good Solvents”. In: *Nano letters* 19.10 (2019), pp. 6993–6999.

[31] Urs Gasser. “Crystallization in three-and two-dimensional colloidal suspensions”. In: *Journal of Physics: Condensed Matter* 21.20 (2009), p. 203101.

[32] P G De Gennes. “Scaling theory of polymer adsorption”. In: *Journal De Physique* 37.12 (1976), pp. 1445–1452.

[33] G. F. Goya et al. “Static and dynamic magnetic properties of spherical magnetite nanoparticles”. In: *Journal of Applied Physics* 94.5 (2003), pp. 3520–3528. ISSN: 00218979. DOI: 10.1063/1.1599959.

[34] Marek Grzelczak et al. “Directed self-assembly of nanoparticles”. In: *ACS nano* 4.7 (2010), pp. 3591–3605.

[35] Pablo Guardia, Amilcar Labarta, and Xavier Batlle. “Tuning the Size, the Shape, and the Magnetic Properties of Iron Oxide Nanoparticles”. In: *The Journal of Physical Chemistry C* 115.2 (2011), pp. 390–396. ISSN: 1932-7447. DOI: 10.1021/jp1084982. URL: http://pubs.acs.org/doi/abs/10.1021/jp1084982.

[36] B.I. Halperin and David R Nelson. “Theory of two-dimensional melting”. In: *Physical Review Letters* 41.2 (1978), p. 121.

[37] Richard HJ Hannink and Anita J Hill. *Nanostructure control of materials*. Woodhead Publishing, 2006.

[38] Linda Ann Harris. “Polymer stabilized magnetite nanoparticles and poly (propylene oxide) modified styrene-dimethacrylate networks”. PhD thesis. Virginia Polytechnic Institute and State University, 2002.

[39] Le He et al. “Assembly and photonic properties of superparamagnetic colloids in complex magnetic fields”. In: *Langmuir* 27.22 (2011), pp. 13444–13450.

[40] Le He et al. “Magnetic assembly route to colloidal responsive photonic nanostructures”. In: *Accounts of chemical research* 45.9 (2012), pp. 1431–1440.

[41] J Henderson et al. “Pattern transfer nanomanufacturing using magnetic recording for programmed nanoparticle assembly”. In: *Nanotechnology* 23.18 (2012), p. 185304.

[42] JR Henderson and TM Crawford. “Repeatability of magnetic-field driven self-assembly of magnetic nanoparticles”. In: *Journal of Applied Physics* 109.7 (2011), p. 07D329.

[43] Jacob N Israelachvili. *Intermolecular and surface forces*. Academic press, 2015.

[44] Bashar Issa et al. “Magnetic nanoparticles: Surface effects and properties related to biomedicine applications”. In: *International Journal of Molecular Sciences* 14.11 (2013), pp. 21266–21305. ISSN: 16616596. DOI: 10.3390/ijms141121266.

[45] Shun-ichi Iwasaki. “Perpendicular magnetic recording—Its development and realization—”. In: *Proc. Jpn. Acad., Ser. B* 85.2 (2009), pp. 37–54.

[46] Hyun Uk Jeon et al. “Electric field directed self-assembly of block copolymers for rapid formation of large-area complex nanopatterns”. In: *Molecular Systems Design & Engineering* 2.5 (2017), pp. 560–566.

[47] C Kajdas and Bharat Bhushan. “Mechanism of interaction and degradation of perfluoropoly-ethers with DLC coating in thin film magnetic rigid disks—A critical review”. In: *J. Info. Storage Proc. Syst.* Vol. 1. 1999, pp. 303–320.

[48] Hitoshi Kanai, Kenji Noma, and Jongill Hong. “Advanced spin-valve GMR head”. In: *Fujitsu Scientific and Technical Journal* 37.2 (2001), pp. 174–182. ISSN: 00162523.

[49] Peter Keim, Georg Maret, and Hans-Hennig von Grünberg. "Frank's constant in the hexatic phase". In: *Physical Review E* 75.3 (2007), p. 031402. DOI: https://doi.org/10.1103/PhysRevE.75.031402.

[50] S. Khizroev and D. Litvinov. "Perpendicular magnetic recording: Writing process". In: *Journal of Applied Physics* 95.9 (2004), pp. 4521–4537. ISSN: 00218979. DOI: 10.1063/1.1695092.

[51] Jin Young Kim et al. "Two-dimensional nanoparticle supracrystals: a model system for two-dimensional melting". In: *Nano letters* 16.2 (2016), pp. 1352–1358.

[52] Arati G Kolhatkar et al. "Tuning the magnetic properties of nanoparticles". In: *International journal of molecular sciences* 14.8 (2013), pp. 15977–16009.

[53] John M Kosterlitz and DJ Thouless. "Long range order and metastability in two dimensional solids and superfluids.(Application of dislocation theory)". In: *Journal of Physics C: Solid State Physics* 5.11 (1972), p. L124.

[54] John Michael Kosterlitz and David James Thouless. "Ordering, metastability and phase transitions in two-dimensional systems". In: *Journal of Physics C: Solid State Physics* 6.7 (1973), p. 1181.

[55] Sanjay Kumar, Pulak Bhushan, and Shantanu Bhattacharya. "Fabrication of nanostructures with bottom-up approach and their utility in diagnostics, therapeutics, and others". In: *Environmental, chemical and medical sensors*. Springer, 2018, pp. 167–198.

[56] Sukit Leekumjorn, Sravani Gullapalli, and Michael S Wong. "Understanding the solvent polarity effects on surfactant-capped nanoparticles". In: *The Journal of Physical Chemistry B* 116.43 (2012), pp. 13063–13070.

[57] Ryan Z Lei, Andrew J Gellman, and Paul Jones. "Thermal stability of Fomblin Z and Fomblin Zdol thin films on amorphous hydrogenated carbon". In: *Tribology Letters* 11.1 (2001), pp. 1–5.

[58] Charles E Leiserson et al. "There's plenty of room at the Top: What will drive computer performance after Moore's law?" In: *Science* 368.6495 (2020), eaam9744.

[59] Bo Li, Di Zhou, and Yilong Han. "Assembly and phase transitions of colloidal crystals". In: *Nature Reviews Materials* 1.2 (2016), pp. 1–13.

[60] Xiyan Li, Xiaowang Liu, and Xiaogang Liu. “Self-assembly of colloidal inorganic nanocrystals: nanoscale forces, emergent properties and applications”. In: *Chemical Society Reviews* (2021).

[61] Eun-Kyung Lim et al. “pH-triggered drug-releasing magnetic nanoparticles for cancer therapy guided by molecular imaging by MRI”. In: *Advanced Materials* 23.21 (2011), pp. 2436–2442.

[62] Jun Lin et al. “Gold-coated iron (Fe@ Au) nanoparticles: synthesis, characterization, and magnetic field-induced self-assembly”. In: *Journal of Solid State Chemistry* 159.1 (2001), pp. 26–31.

[63] Yan Liu et al. “Differences between top-down and bottom-up approaches in mineralizing thick, partially demineralized collagen scaffolds”. In: *Acta biomaterialia* 7.4 (2011), pp. 1742–1751.

[64] Hartmut Löwen. “Melting, freezing and colloidal suspensions”. In: *Physics Reports* 237.5 (1994), pp. 249–324.

[65] An Hui Lu, E. L. Salabas, and Ferdi Schüth. “Magnetic nanoparticles: Synthesis, protection, functionalization, and application”. In: *Angewandte Chemie - International Edition* 46.8 (2007), pp. 1222–1244. ISSN: 14337851. DOI: 10.1002/anie.200602866.

[66] Abdul Rahman Mohtasebzadeh, Longfei Ye, and Thomas M Crawford. “Magnetic nanoparticle arrays self-assembled on perpendicular magnetic recording media”. In: *International journal of molecular sciences* 16.8 (2015), pp. 19769–19779.

[67] Kenya Murase et al. “Usefulness of magnetic particle imaging for predicting the therapeutic effect of magnetic hyperthermia”. In: *Open J. Med. Imaging* 5.02 (2015), p. 85.

[68] David R Nelson. *Defects and geometry in condensed matter physics*. Cambridge University Press, 2002.

[69] Yung Kang Peng, Shik Chi Edman Tsang, and Pi Tai Chou. “Chemical design of nanoprobes for T1-weighted magnetic resonance imaging”. In: *Materials Today* 19.6 (2016), pp. 336–348. ISSN: 18734103. DOI: 10.1016/j.mattod.2015.11.006. URL: http://dx.doi.org/10.1016/j.mattod.2015.11.006.

[70] C Petit, V Russier, and MP Pileni. “Effect of the structure of cobalt nanocrystal organization on the collective magnetic properties”. In: *The Journal of Physical Chemistry B* 107.38 (2003), pp. 10333–10336.

[71] SN Piramanayagam and Tow C Chong. *Developments in data storage: materials perspective*. John Wiley & Sons, 2011.

[72] Jörg Polte. "Fundamental growth principles of colloidal metal nanoparticles–a new perspective". In: *CrystEngComm* 17.36 (2015), pp. 6809–6830.

[73] Calle Preger et al. "Bottom-up field-directed self-assembly of magnetic nanoparticles into ordered nano-and macrostructures". In: *Nanotechnology* 32.19 (2021), p. 195603.

[74] Zhao Qin and Markus J Buehler. "Hierarchical nanostructures for functional materials". In: *Nanotechnology* 29.28 (2018), p. 280201.

[75] A. G. Roca et al. "Magnetite nanoparticles with no surface spin canting". In: *Journal of Applied Physics* 105.11 (2009). ISSN: 00218979. DOI: 10.1063/1.3133228.

[76] Y Sahoo et al. "Field-directed self-assembly of magnetic nanoparticles". In: *The Journal of Physical Chemistry B* 108.11 (2004), pp. 3380–3383.

[77] *Scanning Electron Microscopy Technology, Scanning Electron Microscopy Technology Overview*. 2014. URL: http://www.nanoscience.com/products/sem/technology-overview/.

[78] G David Scott. "Radial distribution of the random close packing of equal spheres". In: *Nature* 194.4832 (1962), pp. 956–957.

[79] Zongqian Shi et al. "Investigation on the self-assembly of magnetic core-shell nanoparticles under soft-magnet element by using discrete element method". In: *Journal of Magnetism and Magnetic Materials* 475 (2019), pp. 152–159.

[80] Srikanth Singamaneni et al. "Magnetic nanoparticles: recent advances in synthesis, self-assembly and applications". In: *Journal of Materials Chemistry* 21.42 (2011), p. 16819. ISSN: 0959-9428. DOI: 10.1039/c1jm11845e. URL: http://xlink.rsc.org/?DOI=c1jm11845e.

[81] Gurvinder Singh et al. "Self-assembly of magnetite nanocubes into helical superstructures". In: *Science* 345.6201 (2014), pp. 1149–1153.

[82] Valter Ström, Richard T. Olsson, and K. V. Rao. "Real-time monitoring of the evolution of magnetism during precipitation of superparamagnetic nanoparticles for bioscience applications". In: *Journal of Materials Chemistry* 20.20 (2010), p. 4168. ISSN: 0959-9428. DOI: 10.1039/c0jm00043d. URL: http://xlink.rsc.org/?DOI=c0jm00043d.

[83] Shouheng Sun et al. “Monodisperse FePt nanoparticles and ferromagnetic FePt nanocrystal superlattices”. In: *science* 287.5460 (2000), pp. 1989–1992.

[84] Rajagopalan Thiruvengadathan et al. “Nanomaterial processing using self assembly bottom-up chemical and biological approaches”. In: *Reports on Progress in Physics* 76.6 (2013), p. 066501.

[85] Pietro Tierno. “Magnetic assembly and annealing of colloidal lattices and superlattices”. In: *Langmuir* 30.26 (2014), pp. 7670–7675.

[86] Joseph B Tracy and Thomas M Crawford. “Magnetic field-directed self-assembly of magnetic nanoparticles”. In: *MRS bulletin* 38.11 (2013), pp. 915–920.

[87] Philippe Walter et al. “Early use of PbS nanotechnology for an ancient hair dyeing formula”. In: *Nano letters* 6.10 (2006), pp. 2215–2219.

[88] Mingsheng Wang, Le He, and Yadong Yin. “Magnetic field guided colloidal assembly”. In: *Materials Today* 16.4 (2013), pp. 110–116.

[89] Shan X Wang and Alex M Taratorin. *Magnetic Information Storage Technology*. Academic Press, 1999.

[90] Weizhong Wei and Zhen Wang. “Investigation of magnetic nanoparticle motion under a gradient magnetic field by an electromagnet”. In: *Journal of Nanomaterials* 2018 (2018).

[91] Wei Wu et al. “Recent progress on magnetic iron oxide nanoparticles : synthesis , surface functional strategies and biomedical applications”. In: (2015). DOI: 10.1088/1468-6996/16/2/023501.

[92] X Xue, J Wang, and E P Furlani. “Self-assembly of crystalline structures of magnetic core–shell nanoparticles for fabrication of nanostructured materials”. In: *ACS applied materials & interfaces* 7.40 (2015), pp. 22515–22524.

[93] L Ye et al. “Triggered self-assembly of magnetic nanoparticles”. In: *Scientific reports* 6.1 (2016), pp. 1–9.

[94] Longfei Ye et al. “Magnetic-Field-Directed Self-Assembly of Programmable Mesoscale Shapes”. In: *Advanced Functional Materials* 26.22 (2016), pp. 3983–3989.

[95] Yuan Yuan et al. “Effect of surface modification on magnetization of iron oxide nanoparticle colloids”. In: *Langmuir* 28.36 (2012), pp. 13051–13059. ISSN: 07437463. DOI: 10.1021/la3022479.

[96] Jian-Gang Jimmy Zhu. “New heights for hard disk drives”. In: *Materials Today* 6.7-8 (2003), pp. 22–31.

Appendix A

Details on the magnetism of magnetic nanoparticles and interactions during self-assembly

A.1 Magnetic Nanoparticles

From a magnetism point of view, materials are divided into two main types: Diamagnetic Materials and Paramagnetic Materials. [18] Materials such as iron, cobalt, or magnetite, display a spontaneous magnetization that arises from magnetic dipoles due to itinerant electrons and unclosed atomic electron orbitals. Dipoles are coupled in parallel by the exchange interaction between electrons:

Heisenberg formulated a Hamiltonian to represent the interaction of two neighboring atoms, based on Pauli's principle whose total electronic spins, in units of Planck's constant.

$$E_{ex} = -2J_{ij}\vec{S}_i \cdot \vec{S}_j \tag{A.1}$$

This originates from the Pauli exclusion principle in quantum physics and Coulomb energy for two electron i and j. The J_{ij} is the exchange integral. In ferromagnetic material $J_{ij} > 0$ where the spins tend to orient parallel to minimize the exchange interaction energy. In anti ferromagnetism $J_{ij} < 0$, the spins tend to orient antiparallel. When $J_{ij} = 0$ thermal energy aligns magnetic dipoles randomly, resulting paramagnetism with no spontaneous magnetization.

The most striking manifestation of magnetism in solids is the spontaneous mag-

netization of ferromagnetic materials such as iron or magnetite, and this is usually associated with hysteresis. Hysteresis information contribute to the control and optimization of key parameters such as saturation magnetization M_S (Maximum allowed magnetization in a given temperature), coercivity H_c (Magnetic field strength required to completely demagnetize a material), blocking temperature T_B , remanent magnetization M_r (The magnetization left after field is removed), etc. Figure B.1 shows the magnetic hysteresis for different materials.

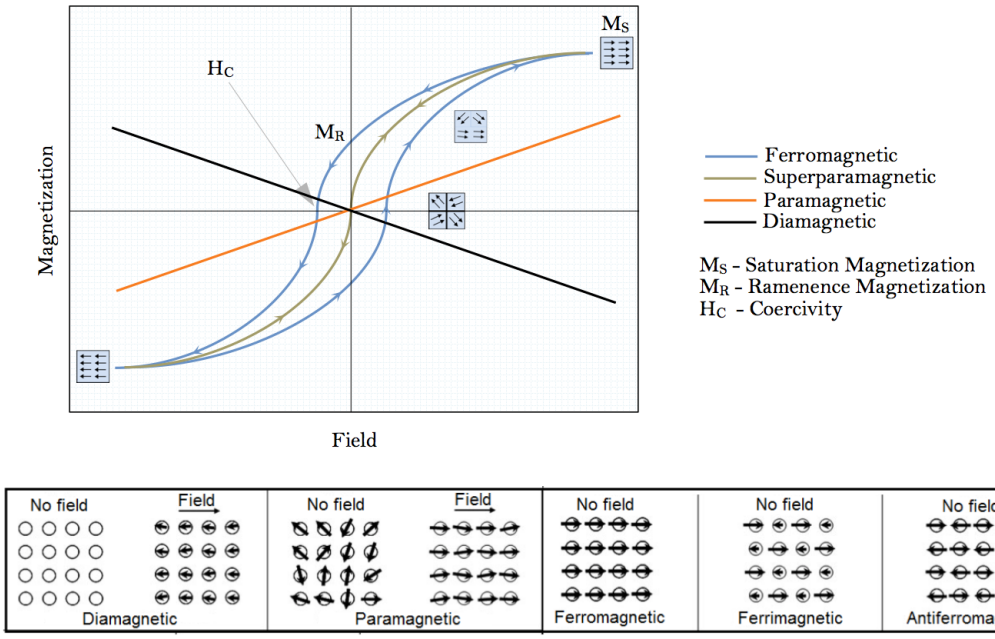

Figure A.1 Hysteresis Loops and representation of moment orientation for different magnetic materials. (Reproduced with permission from [46] and [5])

The spontaneous magnetization due to alignment of the atomic magnetic moments depends on temperature, and it falls precipitously to zero at the Curie temperature T_C. At temperature higher than T_C the ferromagnetic order collapses, and material becomes paramagnetic. The magnetic response to an applied field of materials which do not order magnetically may be either paramagnetic or diamagnetic. In isotropic paramagnets, the induced magnetization $\vec{M}$ is in the same direction as $\vec{H}$, whereas

in diamagnets it is in the opposite direction.

Ferromagnetic, ferrimagnetic, and antiferomagnetic materials have a non-zero coercivity at bulk. They consist of domains (regions) in which magnetic moments are oriented to a specific direction. One of the most important parameters is usually the size of magnetic nanoparticle. This usually leads to another class of magnetic materials with *Superparamagnetic* properties. When material reaches saturation magnetization, domains are rotated such that all moments are aligned even after external field is removed. As the particle's diameter gets smaller the coercivity goes up until particle reaches a critical diameter where coercivity falls to zero. In such diameter particle has a single domain and is called "Superparamagnetic" and magnetization of the particle can randomly flip direction under the influence of temperature. Superparamagnetism follows the behavior of the Langevin function and is related to Blocking Temperature T_B (the minimum energy at which the magnetic moments become blocked).

$$T_B = \frac{KV}{ak_B} \tag{A.2}$$

In which K is the effective anisotropy constant, V is particle's volume, k_B is Boltzmann constant and $a = ln\frac{\tau_m}{\tau_0}$ depends to typical time between magnetization flips *Néel relaxation time* τ:

$$\tau_m = \tau_0 e^{\frac{KV}{k_B T}} \tag{A.3}$$

Where τ_m is measurement time and τ_0 is *attempt time* with a typical value between $10^{-9}s$ and $10^{-10}s$. The net magnetic moment of a nanoparticle is determined by considering several factors such as crystal structure, magnetic interaction among the surface spins, the exchange coupling at the core-shell interface, the magnetic anisotropy of the core and the surface anisotropy [44]. Magnetic anisotropy energy is the energy that keeps the magnetic moment in a particular orientation. At a characteristic size for each type of MNP, the anisotropy energy becomes equal to the thermal

energy, which allows the random flipping of the magnetic moment [52]. These parameters are usually determined by cooling nanoparticles to very low temperature with and without applied fields (Zero Field Cooled (ZFC) and Field Cooled (FC) curves) [7] [75].

Crystal structure of MNPs is shown in figure A.2.

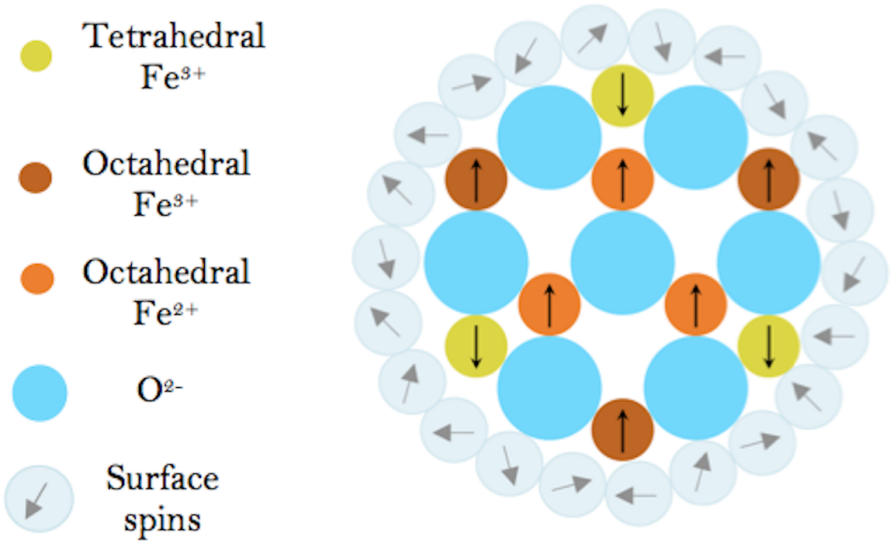

Figure A.2 Iron oxide atom sites

Magnetite essentially has a spinal crystal structure $(Fe^{3+}(Fe^{2+}Fe^{3+})O_4)$, which is essentially a cubic structure with the O^- ions forming a FCC lattice [91]. The cations (usually metals) occupy 1/8 of the tetrahedral sites and 1/2 of the octahedral sites and there are 32 O-ions in the unit cell. This simply means there are two types of cubic building units inside a big FCC lattice, filling all 8 octants $(Fe^{3+})^{tetr}{}_8[Fe^{3+}Fe^{2+}]^{oct}{}_8O_{32}$. From the magnetic moment configuration point of view, magnetite is categorized as ferrimagnetic materials. Its magnetic properties is reflected by the splitting of the 5d orbitals as visualized in Figure B.2 b. The 5d orbitals are split into two subsets due to the influence of oxide ligands, implying that all Fe^{3+} and Fe^{2+} ions have valence electrons and four unpaired electrons respectively. Octahedral coordinations are coupled ferromagnetically, opposite spin in

Fe^{2+} is exchanged to Fe^{3+} However, electrons in Fe^{3+} tetrahedral and octahedral are coupled anti-feromagnetically by O^{2-} atoms resulting cancelation of spins in Fe^{3+}. Therefore unpaired spins in octahedral coordination contributes to magnetization.

A.2 Interactions during self-assembly

A.2.1 Brownian Motion

Nanoparticles in a solution will perform movements in random directions. The motion is due to unequal bombardment of the particles caused and the molecules of the surrounding media. The thermal energy dictates the magnitude of these stochastic forces molecules change their mutual position and can rearrange to the state with minimal free energy and need to be small enough to exhibit Brownian motion

$$lim_{x\to\infty} < \Delta r^2(t) >= 6D_0 t = \frac{k_B T t}{\pi \eta R} \tag{A.4}$$

Where D_0 is the Stokes-Einstein diffusivity, k is Boltzmann's constant, T is temperature, t is time, R is the particle radius, and η is the solvent viscosity. Brownian force in one dimension modeled with Gaussian white noise process, with ζ a random number with Gaussian distribution is

$$\vec{F}_{b,i} = \zeta \sqrt{\frac{2D_0 k_B T}{\Delta t}} \tag{A.5}$$

A.2.2 Gravitational and Bouyant Force

Thegravitational $\vec{F}_g$ and buoyant $\vec{F}_b$ forces are respectively calculated as

$$F_g = \frac{4\rho\pi {R_p}^3 g}{3} \tag{A.6}$$

$$F_b = \frac{4\rho_f\pi {R_p}^3 g}{3} \tag{A.7}$$

where, R_p is particle diameter, ρ is density of particle and ρ_f density of fluid.

A.2.3 Drag Force

$$\vec{F_d} = -6\pi\eta R_p \vec{v} \tag{A.8}$$

where $\vec{v}$ is the particle velocity and η is the viscosity of the fluid.

A.2.4 Magnetic Force

The magnetic force can be predicted using an "effective" dipole moment method in which the particle is modeled as an "equivalent" point dipole with an effective moment $m_{eff} = V_p M_p$

$$\vec{F_m} = \mu_f V_p (\vec{M_p} \cdot \vec{\nabla}) \vec{H_a} \tag{A.9}$$

Here μ_f is permeability of fluid and H_a is applied field. The magnetic force in three dimension can be written as:

$$\vec{F_m}(x,y,z) = F_{mx}(x,y,z)\hat{x} + F_{my}(x,y,z)\hat{y} + F_{mz}(x,y,z)\hat{z} \tag{A.10}$$

where

$$F_{mx}(x,y,z)\hat{x} = \mu_0 V_p f(H_a)\Big[H_{ax}(x,y,z)\frac{\partial H_{ax}(x,y,z)}{\partial x} + H_{ay}(x,y,z)\frac{\partial H_{ay}(x,y,z)}{\partial y} + H_{az}(x,y,z)\frac{\partial H_{ax}(x,y,z)}{\partial z}\Big] \tag{A.11}$$

similarly for $F_{my}(x,y,z)\hat{y}$ and $F_{mz}(x,y,z)\hat{z}$ [92].

A.2.5 DLVO Theory

The DLVO theory that comes from two Russian (Derjaguin and Landau) and two Dutch (Verwey and Overbeek) is a main theory for colloidal stability. The assumption

is that the total force between colloidal particles is addition of the Van der Waals (attractive) and repulsive forces,

$$w_{DLVO}(r) = w_A(r) + w_R(r) \tag{A.12}$$

Where w_A is VDW attractive force and w_R is repulsive force either Electrostatic Double Layer (EDL) force or steric force, as a function of distance r.

The van der Waal's interaction energy between spherical particles with radius R_p with distance D is given by:

$$w_A(D) = -\frac{\alpha}{6}\Big[\frac{2{R_p}^2}{D^2 - r{R_p}^2} + \frac{2{R_p}^2}{D^2} + \ln(\frac{D^2 - 4{R_p}^2}{D^2})\Big] \tag{A.13}$$

Where α is the Hamaker's constant that depends on the shape, medium of interaction and the material that particles are made.

Electrostatic Double Layer:

The forces due to the EDL are caused by the overlap of the electric potential distribution and the overlap of the ion concentration [72, 43] The interaction energy per unit area in EDL repulsive force is given by

$${w_a}^{EDL}(D) = \frac{64\pi k_B T R_p \rho_{\inf} \gamma^2}{\kappa^2} e^{-\kappa D} \tag{A.14}$$

where k_B is Boltzman's constant, T is temperature, $\rho_{\inf}$ is the ionic concentration in the bulk solution, and $\gamma = tanh(\frac{ze\psi_0}{4k_B T})$ with z and e ionic number and electron charge respectively [14] [19]. For a surface charged particle the surrounding fluid is given by $\psi(x) = \psi_0 e^{-\kappa}$ where $1/\kappa$ is the characteristic Debye length which depends on temperature. At room temperature it is $\frac{0.304}{\sqrt{I}(M)}$ with M is ionic strength in molar.

Steric Interaction:

The steric or polymer mediated interaction is rather more complicated involving a great deal of statistical mechanics. There are many theories have been proposed [14]

[19]. The most famous approach was proposed by De Gennes (nobel prize in physics 1991) in which he theoretically explained the mechanism of steric interaction [32].

In his model polymers chains are considered as blobs; inside the blob the chain is self-avoiding but the blobs themselves can overlap and essentially ideal in a good solvent.

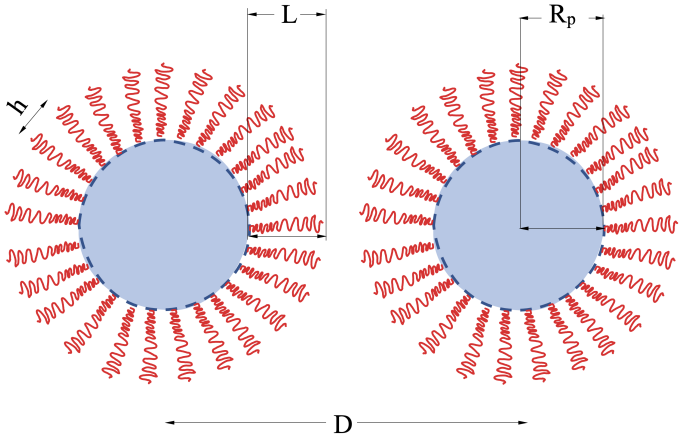

Figure A.3 A schematic representation of polymer brush model

Steric forces are due to the surfaces of colloidal particles that are prevented from aggregating by adsorption of large molecules at the particle surface, such as polymers or surfactants.

$$w_a{}^{steric}(D) = \frac{100 R_p L^3}{(D-2R_p)\pi h^3} k_B T \exp\left[-\frac{-\pi(D-2R_p)}{L}\right] \tag{A.15}$$

Where L is the average length of the ligands, h is the mean distance between two ligand head groups on the surface of the particles. [3]

Figure B.4 shows calculated van der Waals and steric forces for two nanoparticles with 12.5 nm radius, 2 nm ligand length, and 2 nm ligand spacing.

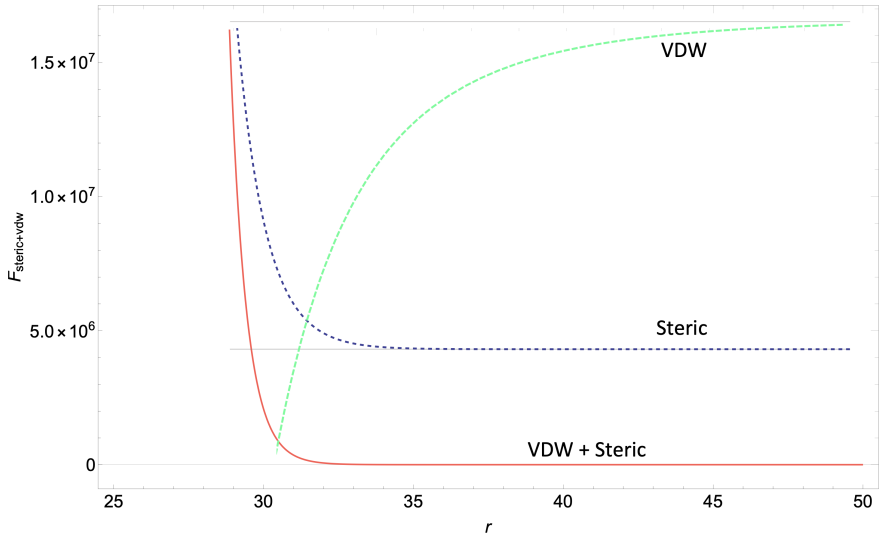

Figure A.4 Plots of van der Waals (green dashed) and steric force (blue dashed) and their sum for two spherical particles with 1 nm separation and Hamaker constant $\alpha = 29 \times 10^{-21} J$

A.2.6 Dipole-Dipole Interaction

The long-range order dipolar inter-particle interactions is another important parameter in the magnetic response of the NPs, because they are usually not enough spatially separated to follow the behavior of an ideal superparamagnet [7] [22]

$$Dipole - dipoleinteraction \propto \frac{m_1 m_2}{r^3}(3\cos^2\Theta - 1) \tag{A.16}$$

the strength of the dipole-dipole interaction is not only proportional to magnitudes of the individual dipoles, but also proportional to the distance, the relative orientation and the spectral overlap of resonances that satisfy the conservation of angular momentum and energy.

A.3 Theoretical calculation of the field gradients in PMR

In a perpendicular magnetic recording media for a single transition in two dimensions, the general solution to the Laplace equation $\nabla^2\Phi(x,y,z)=0$ is given by:

$$\Phi(x,z)=\sum_{n=1}^{\infty}A_n\sin(\frac{n\pi}{a}x)(1-e^{-(\frac{n\pi}{a})\delta})e^{-(\frac{n\pi}{a})z} \tag{A.17}$$

and corresponding fields in x, and z are:

$$\begin{aligned}H_x(x,z)&=-\frac{8M_r}{\pi^2}\sum_{n=1}^{\infty}\Big[\frac{1}{n}\cos(\frac{n\pi}{a}x)(1-e^{-(\frac{n\pi}{a})\delta})e^{-(\frac{n\pi}{a})z}\Big],\\ H_z(x,z)&=\frac{8M_r}{\pi^2}\sum_{n=1}^{\infty}\Big[\frac{1}{n}\sin(\frac{n\pi}{a}x)(1-e^{-(\frac{n\pi}{a}\delta})e^{-(\frac{n\pi}{a})z}\Big]\end{aligned} \tag{A.18}$$

with M_r remnant magnetization, a width of the magnetized region in x direction, and δ is the media thickness [50]. This is a simple case where there is a single transition (Figure A.5 a). For the modified geometry used in this research, where there are two transitions located close together instead of one, and both soft and hard magnetic layers of magnetic recording media are considered, the field expressions are changed. Such geometry is shown in Figure A.5 b. The in-plane component of the stray field above the hard disk ($z>0$) is given by:

$$\begin{aligned}H_x(x,z)=\sum_{n=1}^{\infty}\Big[&-\frac{1}{2n\pi}e^{-(\frac{-2n\pi(t_h+t_c+z)}{d})}e^{(\frac{-2n\pi t_h}{d}-1)})M_{s,h}\Big(sin(2n\pi)\\ &+2(sin(\frac{b_h n\pi}{d}+sin(\frac{n\pi(b_h-2d)}{d})sin(\frac{2n\pi x}{d})\Big)\\ &-\frac{1}{2n\pi}e^{-(\frac{-2n\pi(t_h+t_s+t_sp+t_c+z)}{d})}e^{(\frac{-2n\pi t_s}{d}-1)})M_{s,s}\Big(sin(2n\pi)\\ &+2(sin(\frac{b_s n\pi}{d}+sin(\frac{n\pi(b_s-2d)}{d})sin(\frac{2n\pi x}{d})\Big)\Big]\end{aligned} \tag{A.19}$$

and the out of plane component of the stray field above the hard disk ($z>0$) is given by:

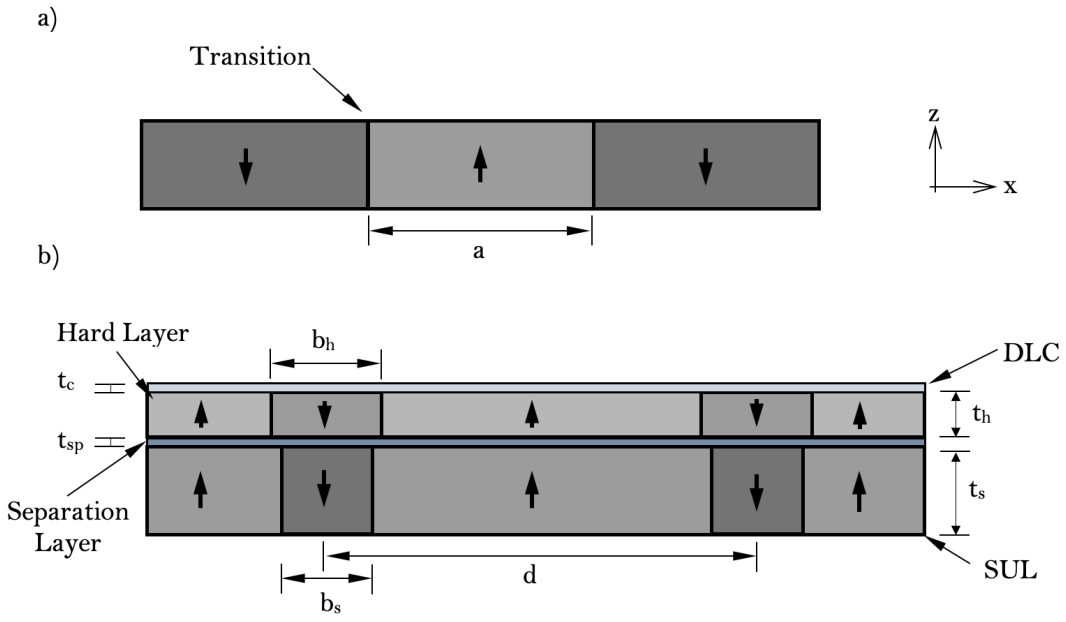

Figure A.5 Perpendicular recording media geometry a) only recording layer with periodic single transition b) recording layer and soft-under layer with periodic stripes containing double transition

$$H_z(x,z) = \sum_{n=1}^{\infty} \Big[-\frac{1}{2n\pi} e^{-(\frac{-2n\pi(t_h+t_c+z)}{d})} e^{(\frac{-2n\pi t_h}{d}-1)) M_{s,h} \Big(sin(2n\pi) + 2(sin(\frac{b_h n\pi}{d} + sin(\frac{n\pi(b_h-2d)}{d}) cos(\frac{2n\pi x}{d}) \Big) - \frac{1}{2n\pi} e^{-(\frac{-2n\pi(t_h+t_s+t_sp+t_c+z)}{d})} e^{(\frac{-2n\pi t_s}{d}-1)) M_{s,s} \Big(sin(2n\pi) + 2(sin(\frac{b_s n\pi}{d} + sin(\frac{n\pi(b_s-2d)}{d}) cos(\frac{2n\pi x}{d}) \Big) \Big] \quad \text{(A.20)}$$

where d is the separation between reversed magnetic regions, b_h is the distance between two transitions in hard layer, b_s is the distance between two transitions in soft layer, t_c, t_h, t_{sp}, t_s, are the thickness of the capping, hard, spacer, and soft layer of the hard disk drive respectively $M_{s,s}$ and $M_{s,h}$ are the saturation magnetization of the soft under-layer and hard layer respectively.

The soft under layer (SUL) combines with the recording head during the write process, producing a magnetic 'image' of the write head below the medium to boost

the size of the write field. Yet once recorded, the SUL also produces an image of the medium magnetization as well, which modifies the field above the medium. Therefore this layer plays an important role for magnetic field directed self-assembly of nanoparticles and must be taken into account for theoretical and simulation purposes to model the true effect of the medium stray field on self-sssembly.

Next, we plot the fields, gradients and forces generated by perpendicular recording media with inclusion of soft under layer, and compare them to the case for the case with a single transition that can be found in [94]. The magnetic force that assembles the magnetic nanoparticles depends on the magnetic field, its gradient at the medium surface, and how both vary with respect to the recorded transitions.

$$\vec{F_m} = \mu_0 V_p (\vec{M_p} \cdot \vec{\nabla}) \vec{H_a} \tag{A.21}$$

Here μ_0 is the permeability of free space, V_p is the volume of the nanoparticle, Mp is its magnetization, and H_a is the external field. We neglect the interaction of the supporting fluid with the field gradient because the diamagnetic hexane used here has a molar susceptibility three orders of magnitude smaller than the iron oxide nanoparticles, but note that its diamagnetism would actually enhance nanoparitcle assembly due to negative magnetophoresis.

In two dimensional geometry, forces on particles due to media magnetization has two components:

$$\vec{F}_m(x,y) = F_{mx}(x,y)\hat{x} + F_{my}(x,y)\hat{y} \tag{A.22}$$

where

$$F_{mx}(x,y)\hat{x} = \mu_0 V_p f(H_a)\Big[H_{ax}(x,y)\frac{\partial H_{ax}(x,y)}{\partial x} + H_{ay}(x,y)\frac{\partial H_{ay}(x,y)}{\partial y}\Big] \tag{A.23}$$

$f(H)$ is a function that allows for variation and saturation of the the NPs magnetic susceptibility as a function of magnetic field. [29]

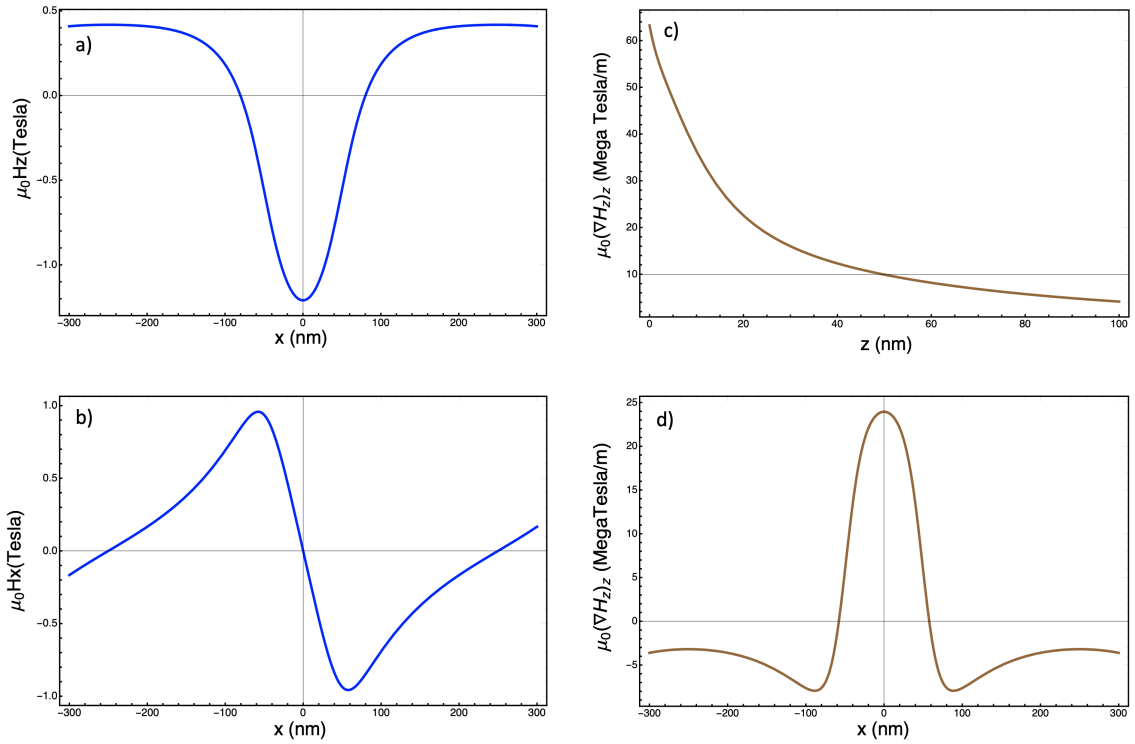

Figure A.6 a) z component, b) x component, of the Magnetic field as a function of x, c) z component of z-directed field gradient as a function of z, and d) x component of the z-directed field gradient as a function of x

For a 27 nm diameter iron oxide nanoparticle coated with oleic acid in hexane, corresponding field profiles and forces due to a media with parameters that are shown in Table A.1 are as following. Figure A.4 a and b shows z and x components of magnetic fields in horizontal (x) direction, the z component of the field is negative on both side of the stripe with two transitions, the x component of the field is negative on one side and positive on another side.

Magnetic nanoparticles in such fields are oppositly magnetized along x direction but have the same magnetization along the z direction near a single transition.

Figure A.6 c and d, show the z-component of the gradient of the z-directed mag-

Table A.1 Parameters table for $d = 500$ nm

$\rho\ [\frac{kg}{m3}]$	$t_h\ [nm]$	$t_s\ [nm]$	$t_c\ [nm]$	$b_h\ [nm]$	$b_s\ [nm]$	$M_s\ [\frac{A}{m}]$	$M_h\ [\frac{A}{m}]$
5.255	15	200	3	100	90	1.8×10^6	2.8×10^6

netic field as a function of z (height above the disk drive medium), and as a function of x (panel d at a height of $z = 30$ nm away from the medium surface) respectively. Note that at 30 nm close to surface the z component of the field gradient is nearly 30 $\frac{MT}{m}$ and falls off rapidly with height.

Figure A.7 shows force profiles on a nanoparticle with 27 nm diameter. The x directed magnetic force (Figure 2.5 a) peaks to 90 pN, drops to 40 pN at 100 nm, and persists beyond each double transition. The peaks on two sides from the center of double-transition, at $(x = -50)$ and $(x = +50)$, push the nanoparticles horizontally close to transitions. The force acting on a magnetic nanoparticle is sensitive to the diameter of the nanoparticle. Figure A.7 b shows a comparison of the horizontal force on particles with 3 different radii. As we will see in the next chapter, this force can transform self-assembly of nanoparticles when we change the hydrodynamic radius of nanoparticles. The z directed force (Figure A.7 c) which is negative, pushes the particles downwards close to transitions. The net force on the particles, shown in Figure A.7 d, peaks beyond 110 Pn and maximum around stripe with two transitions but with a dip right at the center of the double transition.

A.4 Electron Microscopy

In this research we extensively used Scanning Electron Microscope (SEM) as a tool to observe self-assembly of mangetic nanoparticles. It is worth mentioning the basic concept of electron microscopy. SEM scans a focused electron beam over a surface of a target to create an image. For the measurement of nanoparticle properties and see how nanoparticle patterns grow with time, it is important to have high resolution

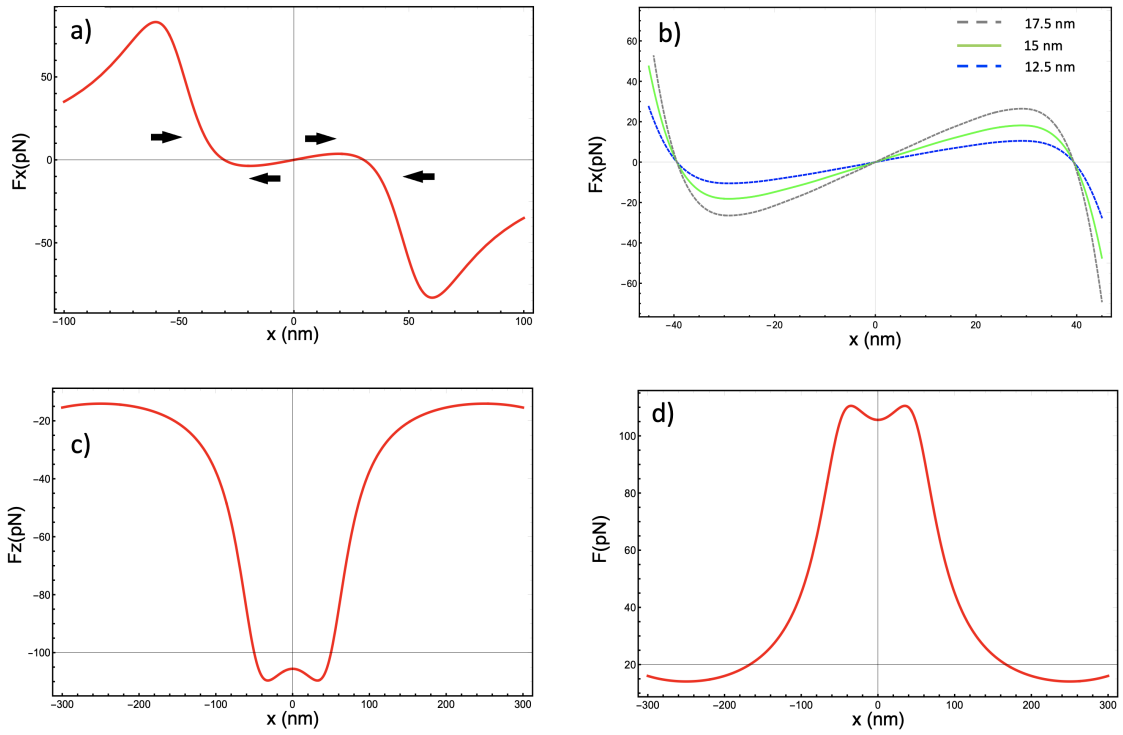

Figure A.7 For a 27 nm particle a) x- component of the magnetic force, b) comparison of horizontal component of the magnetic force for particles with 3 different radii, c) z- component of the magnetic force, d) net force.

images. In SEM, electrons are produced by filament, usually tungsten [77]. Electrons then accelerated towards the sample. During this process electrons are focused by different lenses and apertures. The position of the beam is controlled by coils that allow the beam to be scanned over the sample surface. The incident electron beam will interact with the sample surface sample and produce back-scattered secondary electrons which are collected by detector [77]. Figure A.8 shows the SEM structure.

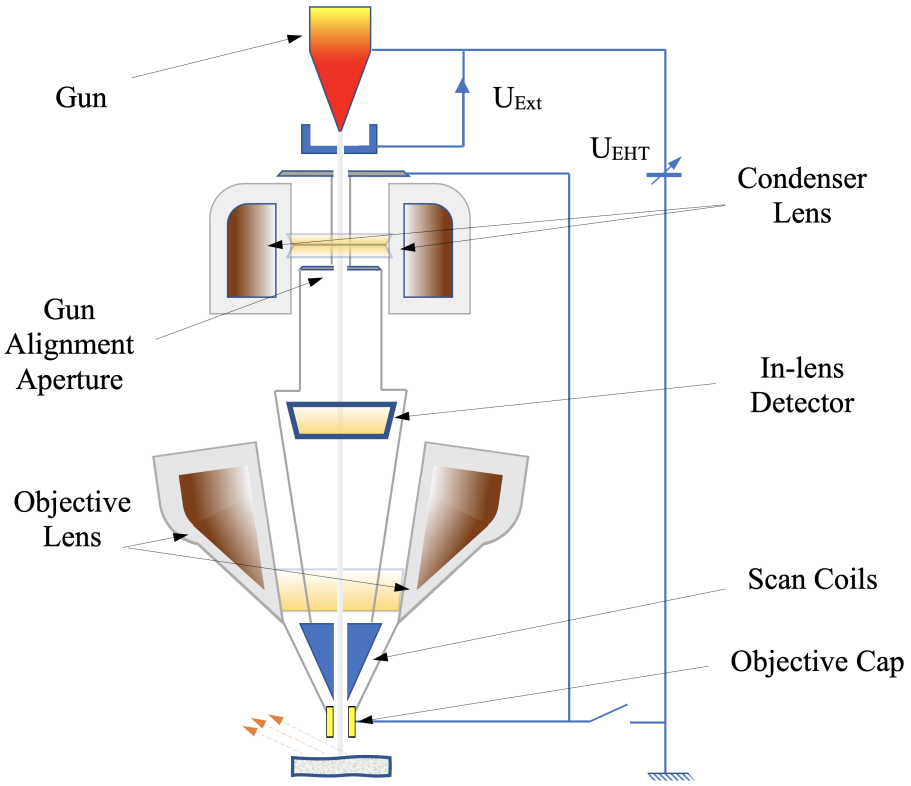

Figure A.8 Components of a Scanning Electron Microscope (SEM)

Appendix B

Experimental section details

B.1 Preparing Nano-Particles Solution for self-assembly experiments

Magnetic nanoparticles in our experiments are purchased from PrecisionMRX. The Magnetite (Fe_3O_4) nanoparticles coated with oleic acid (50.8mg) are mixed with 2.54 mL hexane (Sigma Aldrich Anhydrous 95 percent) to obtain stock solution. Aqueous Magnetite (Fe_3O_4) are coated with a monolayer of oleic acid and a monolayer of an amphiphilic polymer with carboxylic acid functionality and have 20 $\frac{mg}{mL}$ concentration. The diameter for both type of nanoparticles are determined by TEM. Amount of 12.2 μL of stock solution for type particles were mixed with 5 mL of hexane or DI water and 200 μL of each sample was poured on two TEM grids. Image analysis are performed using ImageJ, suggesting that the diameter averages to 27.03 nm with $\pm$ 4.1 nm standard deviation for nanoparticles in hexane and 28.1 nm with $\pm$ 4.4 nm standard deviation for nanoparticles in DI water. Figure A.1 shows TEM image and size distribution for both kind of particles.

B.2 Nanoparticles pattern transferring methods

While it has been shown that aqueous nanoparticles can be transferred to a polymer film for further studies [66],[21], for non-aqueous nanoparticles there are two alternative methods. One way is to coat the surface of the disk drive with Poly-methyl methacrylate (PMMA) and use Polydimethylsiloxane (PDMS) to lift nanoparticles or

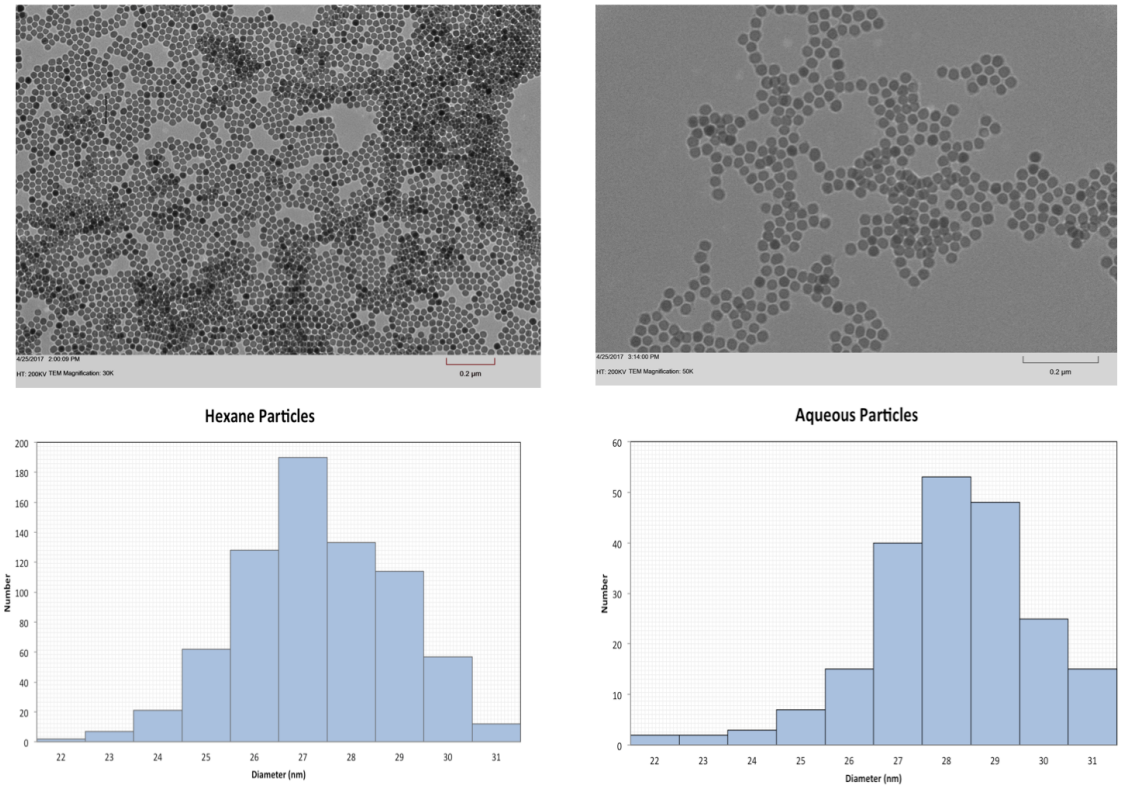

Figure B.1 TEM images and Size Distribution for particle dispersion in Hexane (left) and DI Water (right)

transfer to desired substrate. Another approach is to use Silicon Nitride (SiN) TEM window grid. This window grids have a 10 nm robust SiN membrane that can be placed on recorded templates and allows nanoparticles to self-assemble and be transfered for further application. Figure B.2 shows results of nanoparticles self-assembly using SiN membrane.

B.3 Required tools for HDD disassembly

The required tools to disassemble a disk drive are shown in Figure B.3. It is important to operate in electrostatic free environment. For that using a grounded metallic tray, Electro-Static Discharge (ESD) wrist band, and ESD ionizer blower can be very useful. For all magnetically recorded templates in this research, the head assembly

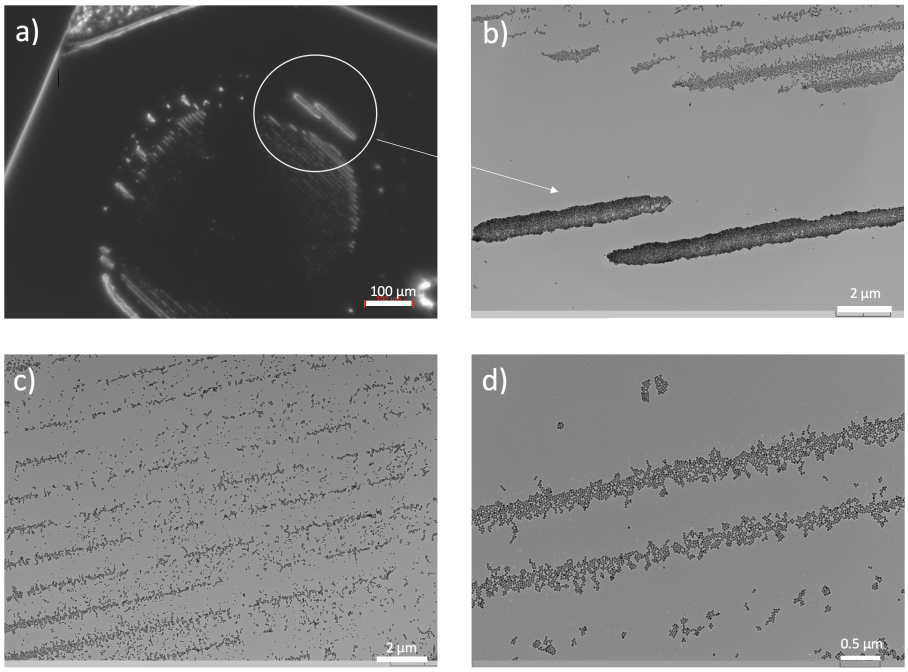

Figure B.2 a) Optical image of a window wafer after nanoparticles self-assembly at 100x magnification and b) corresponding TEM image. c) to d) TEM images of self-assembly at 1000 nm spacing

and magnetic medium is extracted from HGST Travelstar7000 (Figure B.4). This hard disk drive comes with two disk platters and four head assemblies.

B.4 Hard Drive Disassembly Steps

Step 1: Using T6 torx bit remove 6 screws at the corners of HDD and one screw in the lower part under the label (Figure B.5).

Step 2: Using T6 torx and tweezers carefully remove the spindle.

Step 3: Using tweezers, carefully remove the filter.

Step 4: Using plastic tweezers, carfelly remove media and place them in a safe container. The media can be cut into desired pieces and used for magnetic patterning.

Step 5: Carefully place the head comb in head assembly hole on a swing arm.

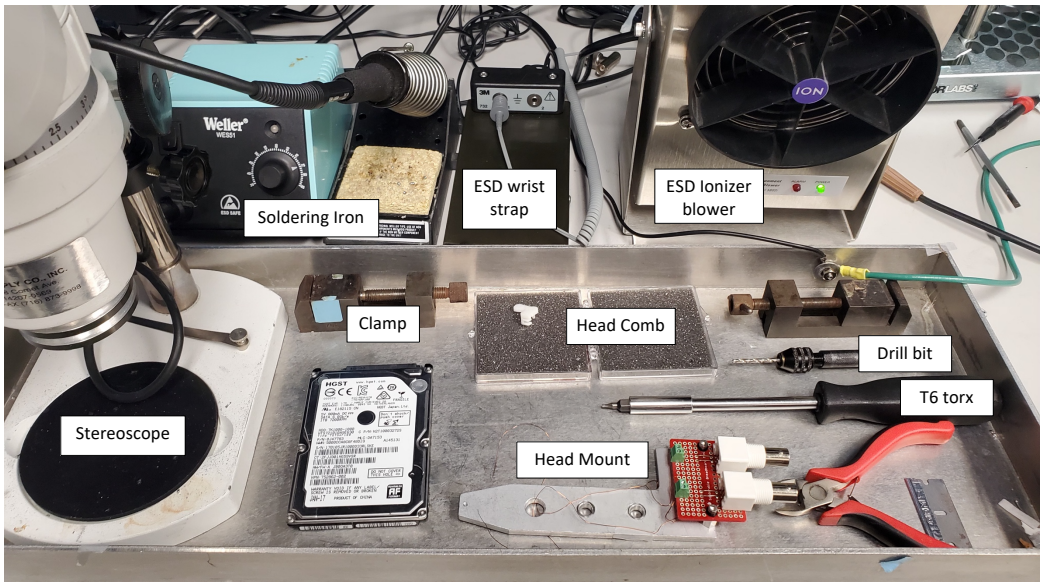

Figure B.3 Tools and environment for disk drive disassembly

Step 6: Move the swing arme to one side and using T6 torx remove the parking ramp.

Step 7: Remove magnet that holds the swing arm, there are three screws, use T6 torx. Carefully lift the magnet with pliers.

Step 8: Remove the swing arm screw located in the back of Hard Disk Drive marked in yellow (Figure B.6).

Step 9: Remove the circuit board and carefully lift the swing arm.

Step 10: Mount the swing arm to a clamp.

Step 11: Observe the electric pads of heads under the stereoscope and desolder them to remove from circuit board. To avoid read head damage due to Electrostatic Discharge (ESD), make sure to short the electric pads with soldering material, i.e. cover electric pads with soldering material.

Step 12: Once circuit board is disconnected, carefully bend the lower head with pliers until the aluminum swing arm is broken.

Step 13: Mount the broken arm to a clamp and slowly drill through the hole

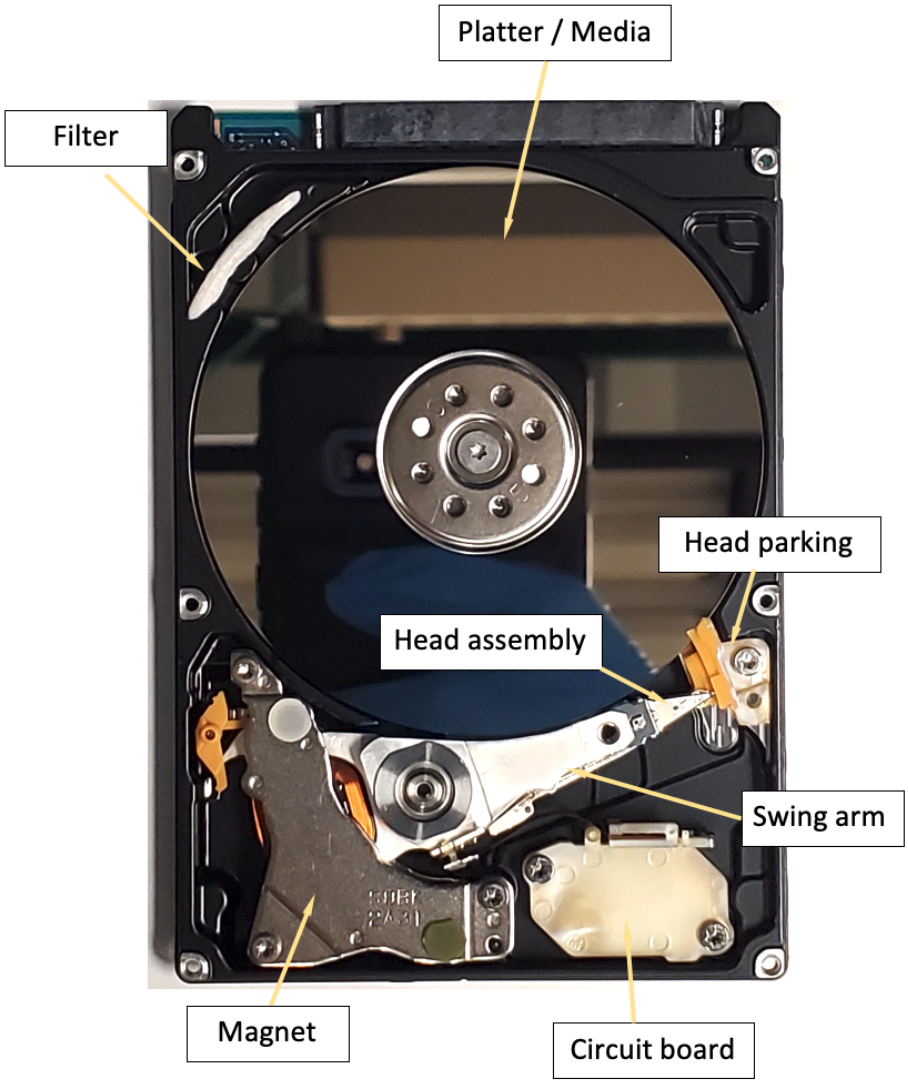

Figure B.4 Hard Disk Drive parts

that keeps the head attached until head is completely detached. Repeat the process for other heads. Note that, two middle heads are attached to a single aluminum arm, one has to carefully drill through one head to release the other one.

Step 14: Place the heads in a ESD protected container. Make sure heads are facing up.

Step 15: Mount the head to the external arm with a screw. Solder read and write head wires. For the write head, solder sixth and seventh pads. These pads

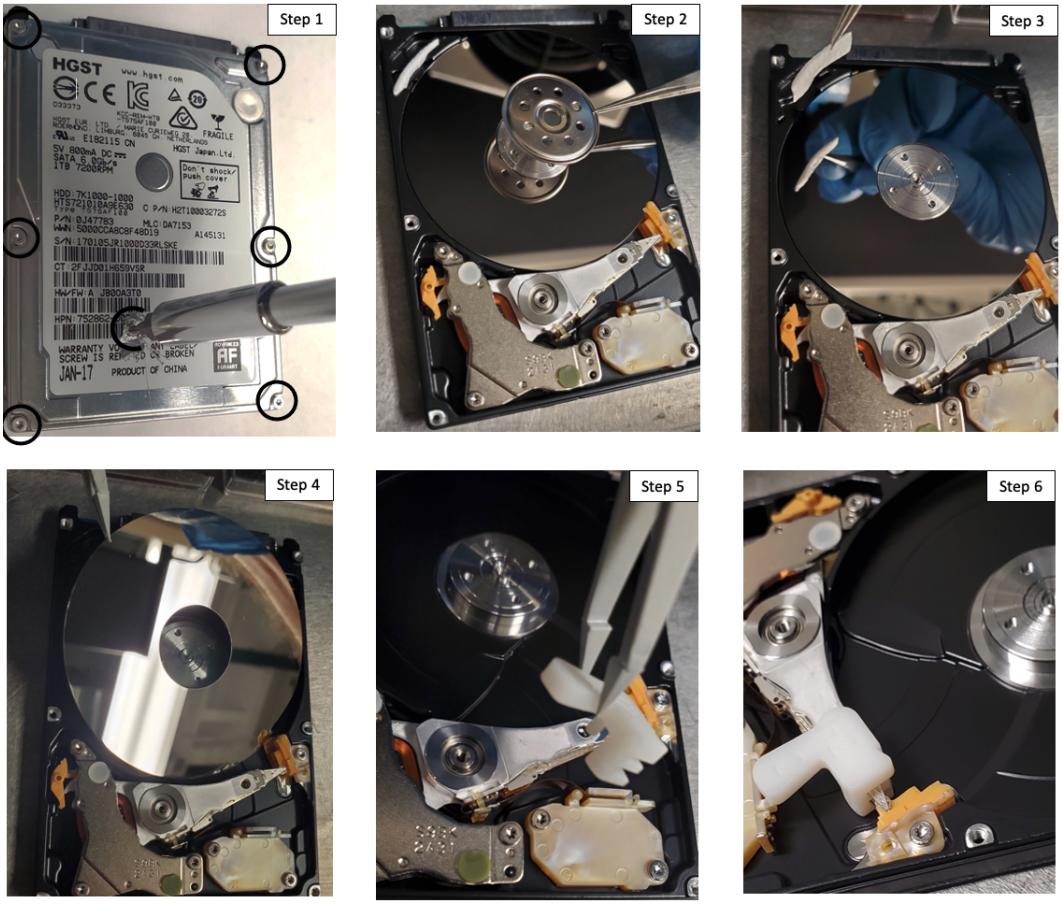

Figure B.5 Steps 1 to 6

should read 6 - 7 Ω. For the read head solder third and fourth pads. The read head is typically around 450- 550 Ω. Read head should never be measured with multi-meter directly. (Figure B.7)

B.5 Improving recording speeds

As shown in Figure B.8, read/write heads are embedded in a slider which is held by a suspension assembly. The assembly of a suspension and a slider forms a head gimbal assembly (HGA) that are held with load beam. The suspension enables the slider to fly just above the surface of the spinning disk with a flying height of five nanometers. [96] When HGA is used to record magnetic patterns for self-assembly,

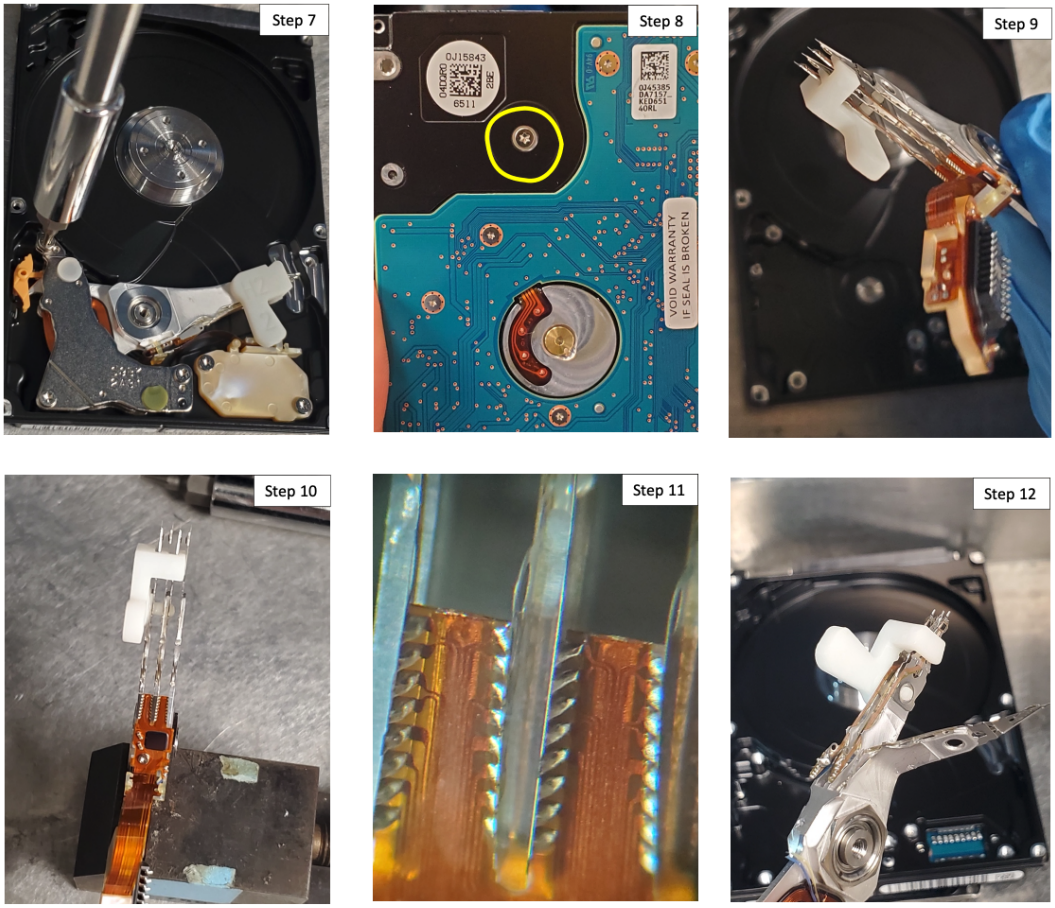

Figure B.6 Steps 7 to 12

achieving high speeds recording becomes challenging, mainly because of tribological failure. To prevent this, one way is to stiffen the suspensions with mounting was. The recommended wax is Mounting Wax 80 which has high hardness and is typically used for polished metallic surfaces.

Once head is connected to the holder follow these steps:

Step 1: Cut small peices of Mounting Wax 80 and place on HGA near the suspensions.

Step 2: Apply low heat with soldering tip until wax covers holes from top.

Step 3: Apply higher heat until wax melts and penetrates under the suspensions. Check the rosin flow and make sure it reaches suspensions and holds them with load

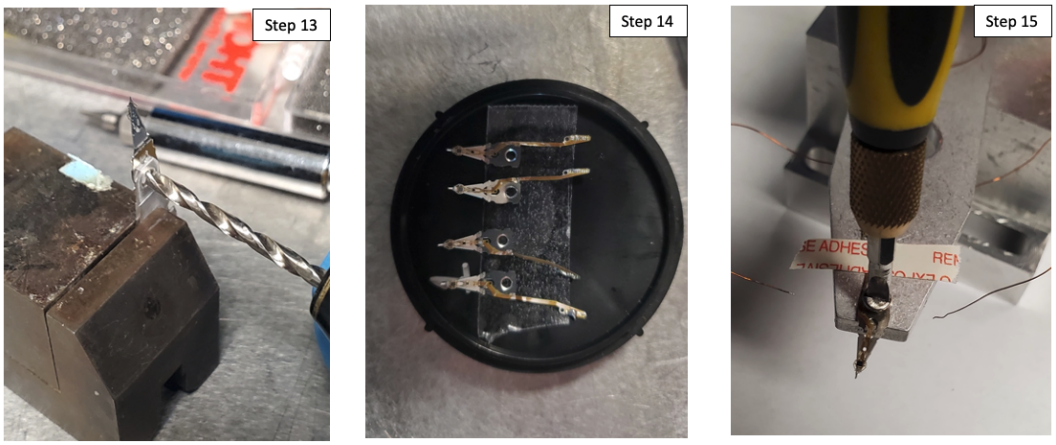

Figure B.7 Steps 13 to 15

beam from bottom. Never allow rosin to flow behind the line indicated in (Figure B.9). Never apply heat to the rosin and HGA from bottom.

If mounting wax is not available, one can use rosin core soldering wire to stiffen the suspensions. Hold the wire on top of HGA near the suspension holes, and touch the wire with hot soldering tip until rosin flows under the suspension (at 60 - 80 degrees of Celsius).

B.6 Details on recording parallel magnetized lines

The medium is cut into desired pieces, erased using a 2 T external magnetic field applied by a Quantum Design Physical Property Measurement System (PPMS), and cleaned with deionized water and methanol. An Aerotech3000 XY stage with 10 nm resolution was employed to record patterns on the disk drive medium. Prior to recording, the sample is coated with a thin layer of lubricant. For lubrication, we apply $1mL$ of 0.01% Zdol-Vertrel XF mixture on the surface of the sample and spin coat for 1 minute at 8000 RPM. The mixture contains $10\mu L$ Z-dol in $9900\mu L$ Vertrel XF solvent. Zdol is a class of Fombilines that are random copolymers with very high thermal stability and low viscosity, and Vertrel XF is a proprietary hydrofluorocarbon

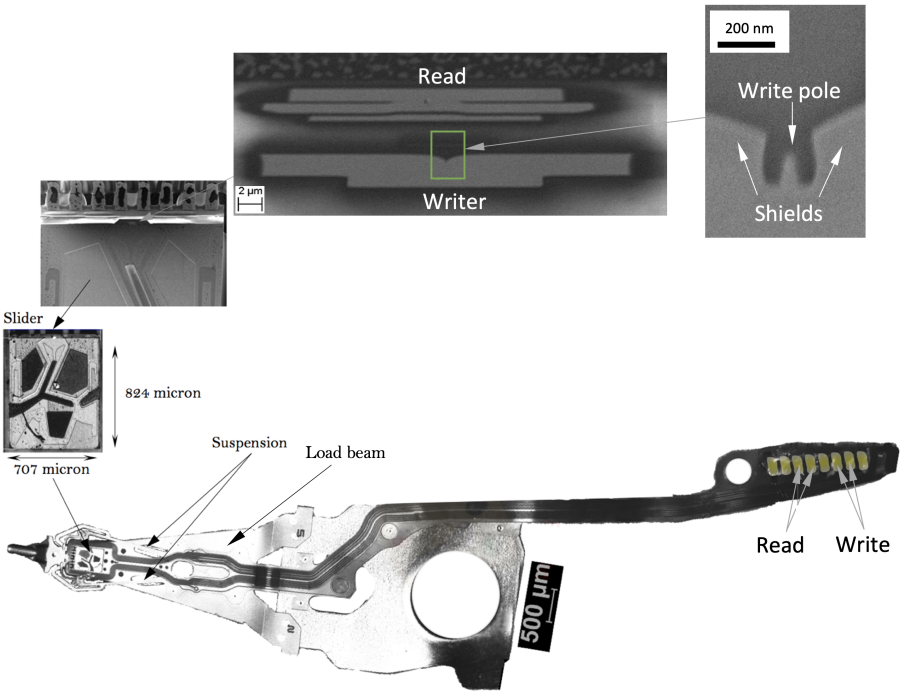

Figure B.8 Microscope image of a head assembly and zoomed in image of slider. The read and write head elements that are embedded in the slider are imaged with SEM

(HFC) fluid ideally suited for vapor degreasing equipment for cleaning, rinsing, and drying. They are the most common lubricant used in hard disk drives [57]. Patterns with area $A = 1000 \times 100$ μm^2 consist of parallel magnetized lines with spacing d. Additional patterns of area A are made with d ranging from 50 nm to 2000 nm. Single written lines have widths corresponding to the write head width ($\sim$ 100 nm) and were recorded by dragging the head across the media (along the Y-direction) at a speed of 750 μm s^{-1} while applying 0.7 V to the write head. The process is repeated for different X (incremented by d) until the region of area A is filled with parallel magnetized lines.

Table B.1 shows parameters imported to the LabView software for recording. As seen in this table, 21 rectangular regions with 1 mm length and 0.1 mm width are recorded with 750 μms^{-1} speed and 0.7 Volts of applied voltage. The first rectangle

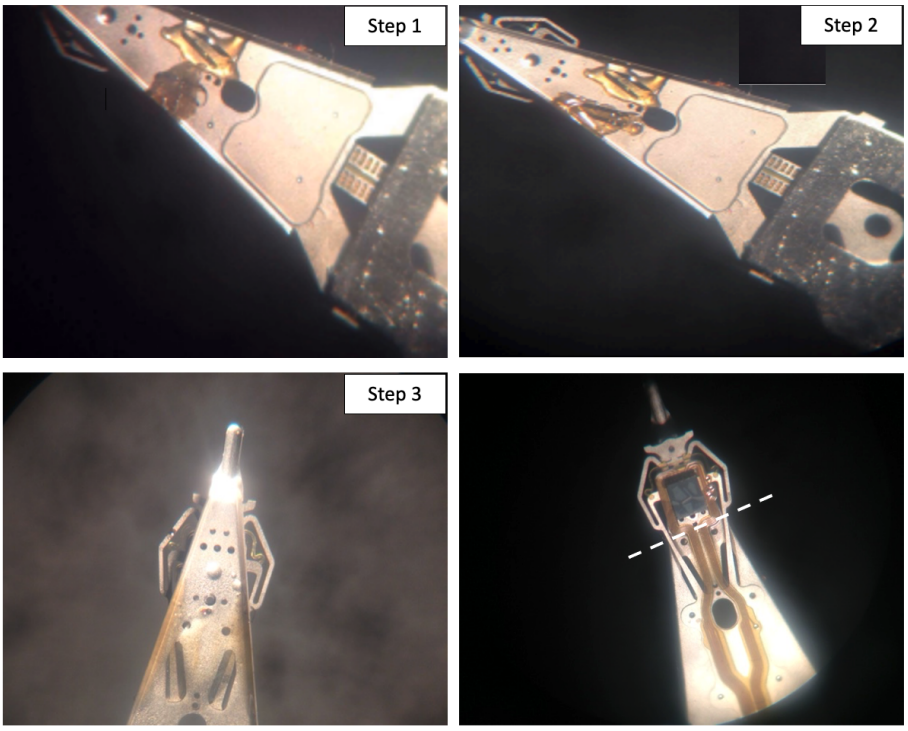

Figure B.9 Stiffening steps 1 to 3. Lower right image indicating the line where mounting wax should not reach.

Table B.1 Patterns on sample with varying line spacing, fixed voltage and fixed recording speed.

No.	Length of Pattern [μm]	Width of Pattern [μm]	Number of Lines	Line Spacing [nm]	Applied Voltage [V]	Speed in Y [$\frac{\mu m}{s}$]	Speed in X [$\frac{\mu m}{s}$]
1	1000	100	1	50	0.7	750	10
2	1000	100	1	100	0.7	750	10
3	1000	100	1	200	0.7	750	10
...	...	...	...	...	...	...	...
21	1000	100	1	2000	0.7	750	10

has a spacing of 50 nm, and the spacing for the remaining 20 rectangles is increased from 100 nm to 2000 nm. To remove the lubricant after the disk medium is recorded, we clean the surface of the medium by sonicating the medium with Galden Perfluorosolv PFS-2 solvent.

Next, the entire sample is submerged in the nanoparticles solutions and stirred for 20 minutes using the spin/rotating machine. The nanoparticle solution concentration is $14.5\mu L$ stock solution in $10mL$ Anhydrous Hexane. After the coating is completed, the sample is lifted straight upwards at a constant rate, and the remaining solution on the medium is evaporated.

B.7 Read-back ESD circuit

Figure B.10 shows a circuit to use for protecting head from the Electro-Static Discharge (ESD). Never measure the resistance of the head directly with a digital multimeter. Instead, use a lock in amplifier. The 500KΩ resistor is used to prevent sudden current flow. For 10 mV it inputs 0.02 mA to the read head. That is enough for a typical head that has 500Ω resistance.

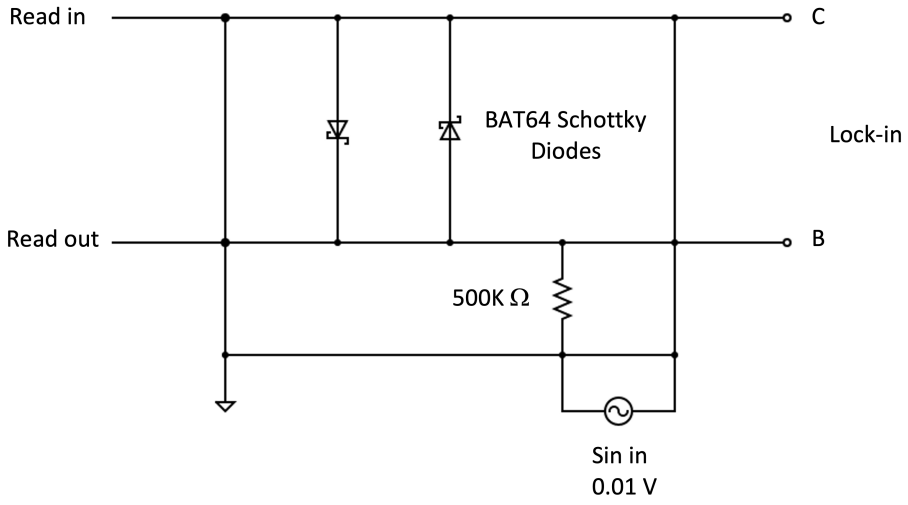

Figure B.10 Read head protection circuit

B.8 Additional examples of nanoparticles self-assembly on templates recorded from bitmap images

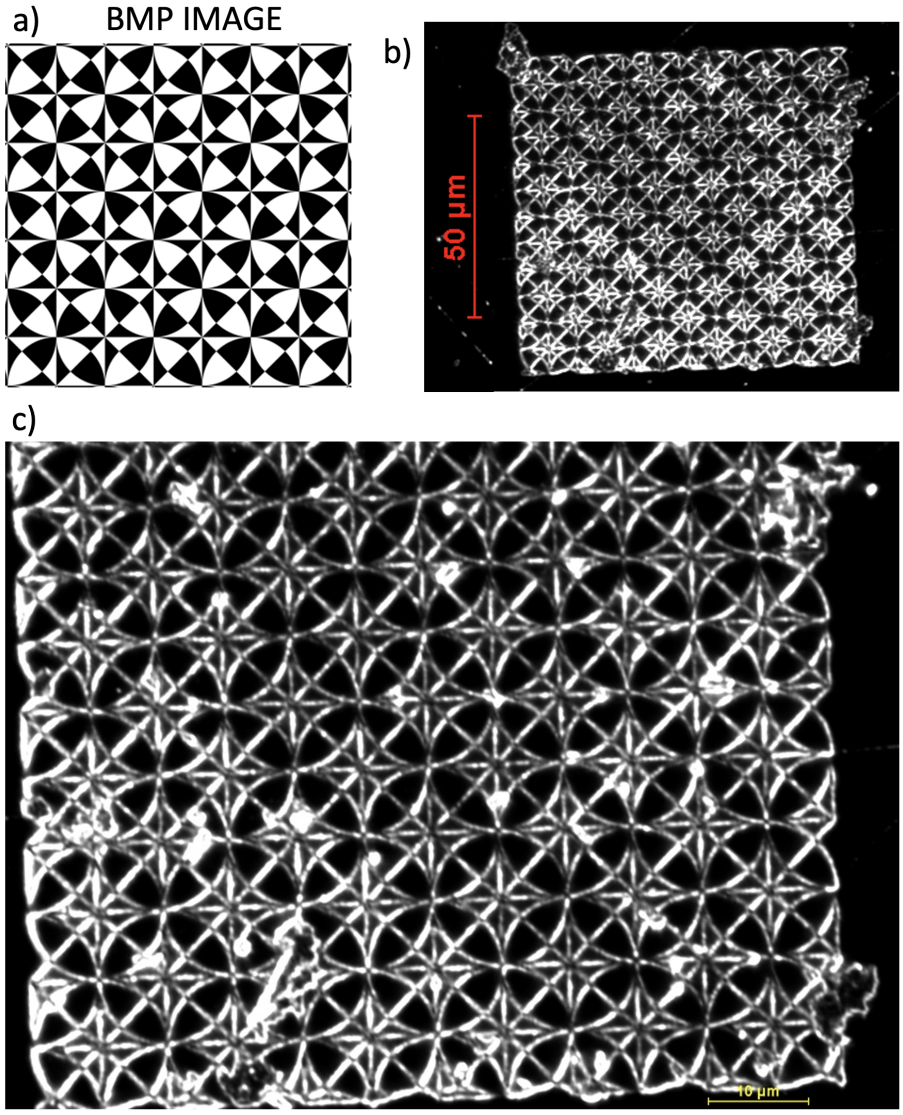

Figure B.11 a) Original Bitmap Image. b) 10x and c) 100x, dark field optical microscope image of assembled nanoparticles on recorded pattern

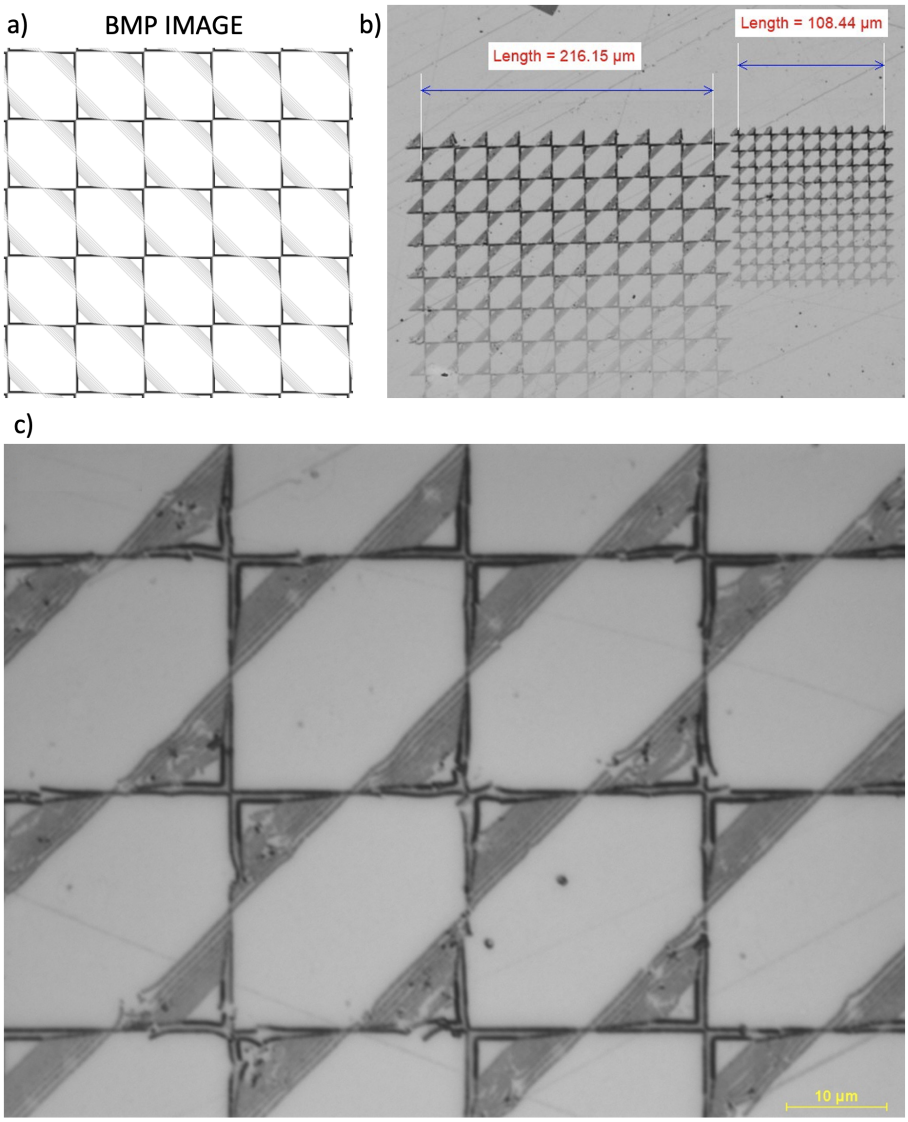

Figure B.12 a) Original Bitmap Image. Bright field optical microscope image of assembled nanoparticles on small and large recorded pattern with: b) 10x magnification and c) 100x magnification.

Appendix C

Image analysis and G_6 calculation

C.1 Calculating spacing, width and edge roughness

To quantify parameters related to self-assembly such as feature width and edge roughness, we use ImageJ Analyze Stripes Package with modification for the case with nanoparticles. Upon smoothing a single line and properly applying threshold, the macro first finds all edges, selects the outer most edges and places them in two groups (Figure C.1). Then it finds the mean, standard deviation, minimum and maximum values of each groups. For a 1 μm long stripe, Line width can be calculated by subtracting the average of each group for. [10]

We also use ImageJ to measure the spacing for each stripe using the center-to-center distance between peaks in horizontal line profiles extracted from the image.

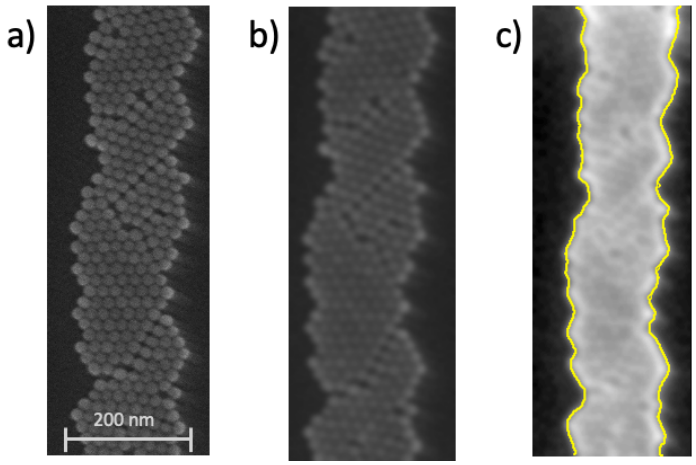

Figure C.1 Width calculation steps: (a) an original SEM image (b) applied blur, (c) adjusted threshold for edge detection separated into two line groups

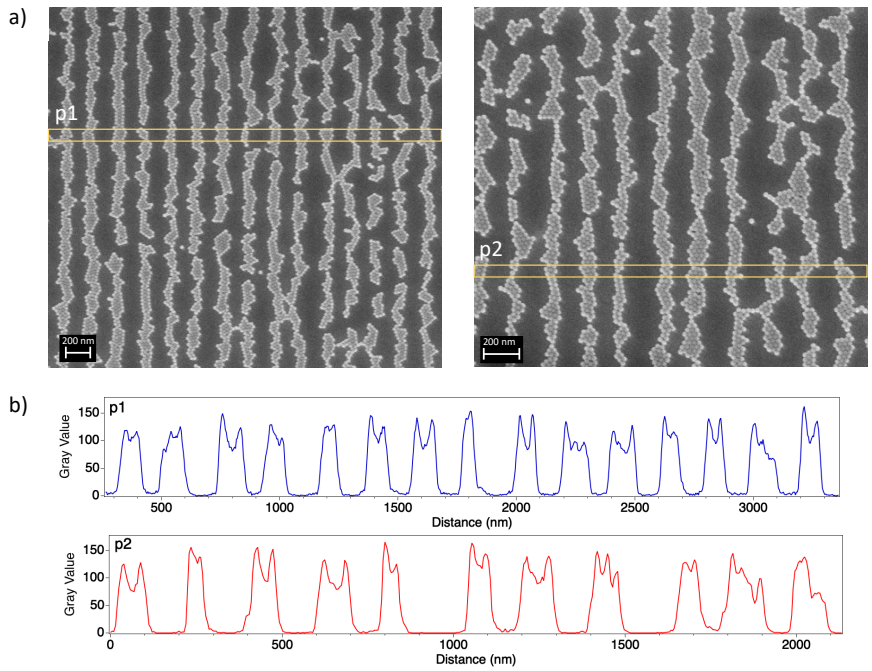

Figure C.2 a) Two SEM images of nanoparticles self-assembly at 200 nm spacing and two rectangular scans p1 and p2. b) Horizontal profiles corresponding to the rectangles p1 and p2.

To get the profiles, a rectangle with the height of 2 to 3 nanoparticles is vertically scanned across multiple images (Figure C.2).

C.2 Calculating bond oreintational parameter

To calculate the center-points of nanoparticles, import an the desired SEM image to Fiji and measure the scale bar conversion factor from pixels. Crop the desired section of the image, adjust window and level, and run the following macro. To run it you should first enable "ImageScience" from the Fiji update sites, update, and restart Fiji. This will enable the Laplacian command. If the center-points were not picked up by macro, use the point selection tool and select them manually. Then measure the points by pressing "**Cmd + m**" in mac or "**Ctrl + m**" in windows, and convert data to "*.txt*" files.

```
setBatchMode(true);
run("Duplicate...", "title=temp");
run("32-bit");
run("Median...", "radius=2");
run("FeatureJ Laplacian", "compute smoothing=3");
selectWindow("temp");
run("Gaussian Blur...", "sigma=5");
setAutoThreshold("Intermodes dark");
run("Create Selection");
run("Select None");
selectWindow("temp Laplacian");
run("Restore Selection");
run("Find Maxima...",
"prominence=0.20 light output=[Point Selection]");
run("Select None");
close();
```

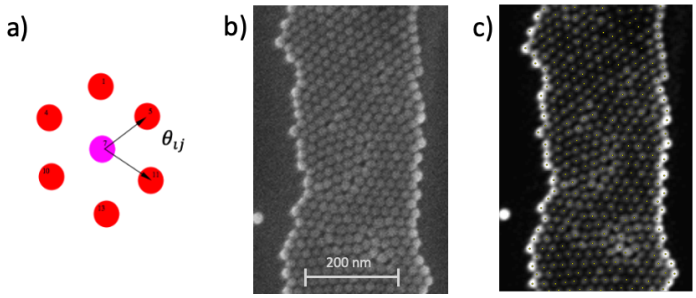

Figure C.3 (a) Illustration of θ_{ij} for a particle i and it's six nearest neighbors, indexed by j. (b) One stripe of an original SEM image. (c) Center points detected after edge detection and applying blur.

```
run("Restore Selection");
setBatchMode(false);
```

All particle pairs are thus calculated, allowing sufficient statistics to determine the mean value of the correlation $G_6(D) = \langle \psi^*{}_6(0)\psi_6(D) \rangle$. Note that particle pairs all have different center-to-center separations so the data must be binned with bins of D being roughly 27 nm wide.

The following Mathematica code was developed with the help of Dr. Karen Livesey from New Castle University. It calculates bond orientation correlation $G_6(D)$ from a text file containing two columns for (X, Y) coordinates in pixels. The pixel value is converted to nanometers based on the scaling factor measured from the SEM image scale bar.

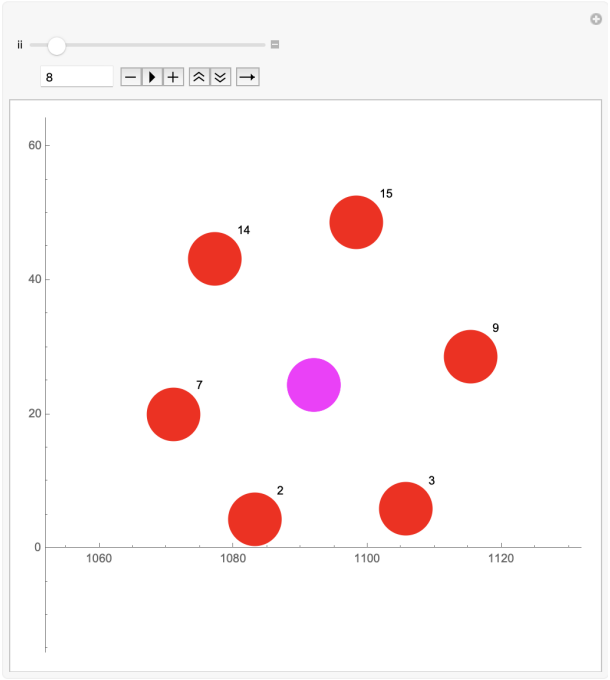

Figure C.4 Example of output of nearest neighbors particles (red) for particle 8 (blue)

The code finds the nearest neighbors to all the points. The nearest neighbors with angle θ_{ij} (Figure C.3) can be seen using the "**InteractivePoints**" command (Figure C.4). To run the program for a single desired file run the command "**processFile["*file name*.txt"]**.

```
Clear["Global`*"]
SetDirectory[NotebookDirectory[]]
files = FileNames[NotebookDirectory[] <> "*.txt"];
Do[Print["Processing file ", files[[n]]];
 processFile[files[[n]]], {n, 1, Length[files]}]
(*Imports a file to process*)
processFile[fileName_] :=
 Module[{data},
```

```
data = Import[fileName, "Data"];
data = data *2.335766423; (* data conversion *)
neighbors500b[i_] := (
  listS[i] = {};
  Do[distX = Abs[data[[i]][[1]] - data[[j]]][[1]];
   distY = Abs[data[[i]][[2]] - data[[j]][[2]]];
   If[Sqrt[distX^2 + distY^2] < 27,
    AppendTo[listS[i], j],
    Continue
    ],
   {j, 1, i - 1}
   ];
  Do[distX = Abs[data[[i]][[1]] - data[[j]]][[1]];
   distY = Abs[data[[i]][[2]] - data[[j]][[2]]];
   If[Sqrt[distX^2 + distY^2] < 27,
    AppendTo[listS[i], j],
    Continue
    ],
   {j, i + 1, Length[data]}
   ]
  );
  (*Make a table of nearest particles to i*)
Table[neighbors500b[i], {i, 1, Length[data]}];
(*List mid points*)
MidPoints[i_] :=
 ListPlot[{Labeled[data[[i]], i]}, AspectRatio ->
 Automatic,
```

```
  PlotStyle -> Directive[PointSize[0.1],
  Magenta], PlotRange -> All];
(*List surrounding points*)
SurroundingPoints[i_] :=
 ListPlot[
  Table[Labeled[data[[listS[i]][[j]]]], listS[i][[j]]],
  {j, 1, Length[listS[i]]}], AspectRatio -> Automatic,
  PlotStyle -> Directive[PointSize[0.1], Red],
  PlotRange -> {{data[[i]][[1]] - 40,
     data[[i]][[1]] + 40}, {data[[i]][[2]] - 40,
     data[[i]][[2]] + 40}}];
(*Plots the data points that are within the range*)
allpts = ListPlot[data, AspectRatio -> Automatic,
  PlotStyle -> PointSize[0.08], PlotRange ->
  {Automatic}];
(*Here for each particle i , calculate
hexagonal angles*)
numneighbors[i_] := Length[listS[i]]; (*
number of neighbors to site i *)
distXX[i_, j_] := -data[[i]][[1]] +
data[[listS[i][[j]]]][[1]]; (*distance in x
between neighbors*)
distYY[i_, j_] := -data[[i]][[2]] +
  data[[listS[i][[j]]]][[2]]; (*distance in y*)
\[Theta][i_, j_] :=
  ArcTan[distXX[i, j],
  distYY[i, j]]; (*angle with x axis*)
```

```
\[Psi][i_] :=
 1/numneighbors[i] Sum[
   Exp[I 6 \[Theta][i, j]], {j, 1, numneighbors[i]}];
   (* Complex angle average at site i *)
pair[i_, k_] := Chop[Conjugate[\[Psi][i]] \[Psi][k]];
(* the pair correlation, between a site i
and a site k *)
separation[i_, k_] :=
 Sqrt[(data[[i]][[1]] - data[[k]][[1]])^2 +
 (data[[i]][[2]] - data[[k]][[2]])^2];
(* how far apart in pixels are sites i and k, chop:
replaces approximate real numbers in expr.

that are close to zero by \the exact integer 0. *)
(* find the maximum distance *)
max = 1;
Do[
 If[separation[i, k] > max,
  max = separation[i, k],
  Continue],
 {i, 1, Length[data]}, {k, 1, Length[data]}
 ];
(* Binning particles *)
bins[binsize_] := (
  Do[
    bin
      [binsize, kk] = {},
```

```
    {kk, 1, Quotient[max, binsize] + 1}
    ];
   Do[
    num = Quotient[separation[i, k], binsize] + 1;
    AppendTo[bin[binsize, num], pair[i, k]],
    {i, 1, Length[data]}, {k, i, Length[data]}
    ]
   );
(* Set the bin size *)
bins[27];
R = 27; (*R is bin number*)
LengthOfElements = Length[data];
(*Calculate the mean of pairs*)
MeanOfPairs = Mean[Table[pair[ii, ii],
{ii, 1, Length[data]}]];
(*save and export datafiles*)
AbsPlotVals =
 Table[{(ii R) - R*0.5, Abs[Mean[bin[R, ii]]]},
 {ii, 1, max/R}];
Export[FileBaseName@fileName <> ".csv", AbsPlotVals];
RealPlotVals = Table[{ii R, Re[Mean[bin[R, ii]]]},
{ii, 1, max/R}];
Export["Real_" <> FileBaseName@fileName <> ".csv",
RealPlotVals];
AllRealPlotVals =
 Table[{ii R, Re[Mean[bin[R, ii]]]}, {ii, 1, max/R}];
Export["ARG6bin" <> FileBaseName@fileName <> ".csv",
```

```
 AllRealPlotVals];
(*plot and export resulting graphs*)
AbsolutePlot =
 ListPlot[
  Table[{(ii R) - R*0.5 , Abs[Mean[bin[R, ii]]]},
  {ii, 1, max/R}],
  Frame -> True,
  FrameLabel -> {"r (nm)",
    "Abs[ \!\(\*SubscriptBox[\(g\), \(6\)]\)(r) ]"},
  LabelStyle -> Directive[Black, Large],
  FrameStyle -> Directive[Thick, Black],
  PlotStyle -> Blue,
  PlotLegends -> {"G6" <> FileBaseName@fileName
  <> "_bin25"}~
    Placed~{0.5, 1}, PlotRange -> {{0, max},
    {0, 0.80}}];
AllPlot =
 ListPlot[
  Table[{(ii R) - R*0.5 , Abs[Mean[bin[R, ii]]]},
  {ii, 1, max/R}],
  Frame -> True,
  FrameLabel -> {"r (nm)",
    "Abs[ \!\(\*SubscriptBox[\(g\), \(6\)]\)(r) ]"},
  LabelStyle -> Directive[Black, Large],
  FrameStyle -> Directive[Thick, Black],
  PlotStyle -> Blue, PlotLegends ->
  {"allG6" <> FileBaseName@fileName <>
```

```
  "_bin25"}~
    Placed~{0.5, 1}, PlotRange -> {{0, max/R},
    {0, 0.80}}];
RealPlot =
 ListPlot[Table[{ii R, Re[Mean[bin[R, ii]]]},
 {ii, 1, max}],
  Frame -> True,
  FrameLabel -> {"r (nm)",
    "Re[ \!\(\*SubscriptBox[\(g\), \(6\)]\)(r) ]"},
  LabelStyle -> Directive[Black, Large],
  FrameStyle -> Directive[Thick, Black],
  PlotStyle -> Blue];
G6plotZero =
 ListPlot[Table[{ii, pair[ii, ii]},
 {ii, 1, Length[data]}],
  Frame -> True,
  FrameLabel -> {"particle number",
    "\!\(\*SubscriptBox[\(g\), \(6\)]\)(0)"},
  LabelStyle -> Directive[Black, Large],
  FrameStyle -> Directive[Thick, Black],
  PlotStyle -> Blue];
Export["G6_bin" <> FileBaseName@fileName <> ".png",
AbsolutePlot];
Export["RP_bin" <> FileBaseName@fileName <> ".png",
RealPlot];
Export["G6PlotAll_bin" <> FileBaseName@fileName
<> ".png", G6plotZero];
```

```
  NeighbsPlot =
   Table[Show[Graphics[SurroundingPoints[ii],
   {ii, 100, 105}],
     Graphics[MidPoints[ii], {100, 105}]],
     {ii, 100, 105}];
  InteractivPoints =
   Manipulate[
    Show[Graphics[SurroundingPoints[ii],
    {ii, 1, 100}],
     Graphics[MidPoints[ii], {ii, 1, 100}]],
     {ii, 1, 100, 1}];
  ]
  (*EXECUTE THE CODE BELOW FOR A SINGLE FILE*)
files = FileNames[NotebookDirectory[] <> "*.txt"];
Do[Print["Processing file ", files[[n]]];
 processFile[files[[n]]], {n, 1, Length[files]}]
```

Appendix D

Permissions

License Details

This Agreement between Mr. Abdul Mohtasebzadeh ("You") and John Wiley and Sons ("John Wiley and Sons") consists of your license details and the terms and conditions provided by John Wiley and Sons and Copyright Clearance Center.

Print Copy

License Number	5352261103597
License date	Jul 18, 2022
Licensed Content Publisher	John Wiley and Sons
Licensed Content Publication	Advanced Materials
Licensed Content Title	Superparamagnetic Colloids: Controlled Synthesis and Niche Applications
Licensed Content Author	Y. Xia, H. Yang, Y. Wang, et al
Licensed Content Date	Dec 12, 2006
Licensed Content Volume	19
Licensed Content Issue	1
Licensed Content Pages	28
Type of Use	Dissertation/Thesis
Requestor type	University/Academic
Format	Print and electronic
Portion	Figure/table
Number of figures/tables	1
Will you be translating?	Yes, including English rights
Number of languages	2
Title	Magnetic Field Directed Self-Assembly of Colloidal Nanoparticles via Extreme Field Gradients of Magnetic Recording Media
Institution name	University of South Carolina
Expected presentation date	Aug 2022
Portions	Figure 1
Specific Languages	English, Persian
Requestor Location	Mr. Abdul Mohtasebzadeh 712 main street Department of Physics and Astronomy COLUMBIA, SC 29208 United States Attn: Mr. Abdul Mohtasebzadeh
Publisher Tax ID	EU826007151
Total	**0.00 USD**

BACK

License Details

This Agreement between Mr. Abdul Mohtasebzadeh ("You") and Elsevier ("Elsevier") consists of your license details and the terms and conditions provided by Elsevier and Copyright Clearance Center.

Print Copy

License Number	5352251151516
License date	Jul 18, 2022
Licensed Content Publisher	Elsevier
Licensed Content Publication	Nano Today
Licensed Content Title	Magnetic nanoparticles for drug delivery
Licensed Content Author	Manuel Arruebo,Rodrigo Fernández-Pacheco,M. Ricardo Ibarra,Jesús Santamaría
Licensed Content Date	Jun 1, 2007
Licensed Content Volume	2
Licensed Content Issue	3
Licensed Content Pages	11
Type of Use	reuse in a thesis/dissertation
Portion	figures/tables/illustrations
Number of figures/tables/illustrations	1
Format	both print and electronic
Are you the author of this Elsevier article?	No
Will you be translating?	Yes, including English rights
Number of translations	2
Title	Magnetic Field Directed Self-Assembly of Colloidal Nanoparticles via Extreme Field Gradients of Magnetic Recording Media
Institution name	University of South Carolina
Expected presentation date	Aug 2022
Portions	Figure 4
Specific Languages	English, Persian
Requestor Location	Mr. Abdul Mohtasebzadeh 712 main street Department of Physics and Astronomy COLUMBIA, SC 29208 United States Attn: Mr. Abdul Mohtasebzadeh
Publisher Tax ID	98-0397604
Total	**0.00 USD**

BACK

License Details

This Agreement between Mr. Abdul Mohtasebzadeh ("You") and AIP Publishing ("AIP Publishing") consists of your license details and the terms and conditions provided by AIP Publishing and Copyright Clearance Center.

Print Copy

License Number	5351500097299
License date	Jul 17, 2022
Licensed Content Publisher	AIP Publishing
Licensed Content Publication	Journal of Applied Physics
Licensed Content Title	Perpendicular magnetic recording: Writing process
Licensed Content Author	S. Khizroev, D. Litvinov
Licensed Content Date	May 1, 2004
Licensed Content Volume	95
Licensed Content Issue	9
Type of Use	Thesis/Dissertation
Requestor type	Student
Format	Print and electronic
Portion	Figure/Table
Number of figures/tables	2
Will you be translating?	Yes
Number of languages	2
Title	Magnetic Field Directed Self-Assembly of Colloidal Nanoparticles via Extreme Field Gradients of Magnetic Recording Media
Institution name	University of South Carolina
Expected presentation date	Aug 2022
Portions	Fig 1
Specific Languages	English
Requestor Location	Mr. Abdul Mohtasebzadeh 712 main street Department of Physics and Astronomy COLUMBIA, SC 29208 United States Attn: Mr. Abdul Mohtasebzadeh
Total	**0.00 USD**

BACK

American Physical Society
Reuse and Permissions License

16-Aug-2022

This license agreement between the American Physical Society ("APS") and Abdul Mohtasebzadeh ("You") consists of your license details and the terms and conditions provided by the American Physical Society and SciPris.

Licensed Content Information

License Number:	**RNP/22/AUG/056803**
License date:	16-Aug-2022
DOI:	10.1103/PhysRevE.75.031402
Title:	Frank's constant in the hexatic phase
Author:	P. Keim, G. Maret, and H. H. von Grünberg
Publication:	Physical Review E
Publisher:	American Physical Society
Cost:	USD $ 0.00

Request Details

Does your reuse require significant modifications: No

Specify intended distribution locations:	United States
Reuse Category:	Reuse in a thesis/dissertation
Requestor Type:	Student
Items for Reuse:	Figures/Tables
Number of Figure/Tables:	2
Figure/Tables Details:	Structure factor Sq of our colloidal system
Format for Reuse:	Electronic

Information about New Publication:

University/Publisher:	University of South Carolina
Title of dissertation/thesis:	Magnetic Field Directed Self-Assembly of Colloidal Nanoparticles via Extreme Field Gradients of Magnetic Recording Media
Author(s):	Abdul R Mohtasebzadeh
Expected completion date:	Aug. 2022

License Requestor Information

Name:	Abdul Mohtasebzadeh
Affiliation:	Individual
Email Id:	mohtaseb@email.sc.edu
Country:	United States